EVALUATION OF ESTABLISHED LOW IMPACT DEVELOPMENT TECHNIQUES: ASSESSING AGED BIORETENTION CELLS AND CLOGGING PERVIOUS CONCRETE

By

ALEX JAMES MCLEMORE

Bachelor of Science in Biosystems Engineering
University of Tennessee
Knoxville, Tennessee
2010

Master of Science in Biosystems Engineering
University of Tennessee
Knoxville, Tennessee
2012

Submitted to the Faculty of the
Graduate College of the
Oklahoma State University
in partial fulfillment of
the requirements for
the Degree of
DOCTOR OF PHILOSOPHY
December, 2017

EVALUATION OF ESTABLISHED LOW IMPACT DEVELOPMENT TECHNIQUES: ASSESSING AGED BIORETENTION CELLS AND CLOGGING PERVIOUS CONCRETE

Dissertation Approved:

Dr. Jason R. Vogel

Dissertation Adviser

Dr. Glenn O. Brown

Dr. Saleh Taghvaeian

Prof. Michael V. Holmes

ACKNOWLEDGEMENTS

I thank my advisor Dr. Jason Vogel for supporting me and providing the guidance that allowed me to complete this research. Additionally, I thank Dr. Glenn Brown for his time and advice and serving on my committee. Dr. Saleh Taghvaeian and Prof. Michael Holmes, I thank them both for being on my committee and providing productive feedback.

There are numerous graduate and undergraduate students in the Biosystems and Agricultural Engineering department at OSU that helped me in one way or another. I owe a significant (p-value<0.001) thank you to John McMaine. Our conversations were immensely helpful. I also thank Brad Rogers, Lise Montefiore, Saroj Kandel, Grant Graves, Kevin Moore, Nelly Ruiz, Riley Jones, Magen Kegley, Hanna Huling, Keima Kamara, Tyler Ogle, and Sagar Neupane. For those unmentioned, thank you.

I thank the Biosystems and Agricultural Engineering staff. Specifically, I thank Jason Walker and Wayne Kiner from the shop and Pat Bridger for their assistance throughout my research journey at OSU.

Lastly and most importantly, I thank my family. Andrea, your endless support and encouragement did not go unnoticed. Thank you. I thank Gray for always being at home to welcome me and bring endless joy to my day. Finally, I thank my parents, Jim and Susan. My ability to complete this research and earn a Ph.D. is without a doubt a product of your commitment to my education and love.

Name: Alex James McLemore

Date of Degree: JULY, 2017

Title of Study: EVALUATION OF ESTABLISHED LOW IMPACT DEVELOPMENT TECHNIQUES: ASSESSING AGED BIORETENTION CELLS AND CLOGGING PERVIOUS CONCRETE

Major Field: BIOSYSTEMS AND AGRICULTURAL ENGINEERING

Abstract: Low impact development practices are commonly installed to mitigate the negative impacts urbanization can have on stormwater runoff and the environment. Research on the long-term performance of aged low impact development practices is lacking. This dissertation includes three studies related to the long-term performance of aged low impact development practices. The first study focuses on hydraulics and leaching potential of two 8-year old bioretention cells with fly ash media filter media. With the use of flooding tests, it was determined that both bioretention cells were meeting design standards and providing pollution retention. However, both bioretention cells leached bacteria when flooded with treated municipal water. The second study involves the evaluation of pervious concrete infiltration rate changes over time, cleaning methods for restoring clogged pervious concrete, and the correlation of results to pervious concrete mix design. Five different pervious concrete tests plots were evaluated, all were used regularly in a parking lot. Infiltration rate underwent three phases as the pervious concrete aged. There was an initial decrease, then a phase of relatively constant infiltration rates, and finally a secondary decrease after which the pervious concrete was considered clogged. Spraying water while simultaneously vacuuming, significantly (95% confidence level) improved infiltration rates. Mixes with higher sand content experienced improved cleaning. The third study involved the application of porous media x-ray computer tomography (CT) techniques to quantify porosity, clogging, and internal characteristics of aged pervious concrete. Pervious concrete evaluated in the third study was cored from the tests plots in the second study. Void content, clogging, and cementitious material were quantified by adapting a frequency fitting distribution material classification method to x-ray CT images of pervious concrete. This is the first known approach that has classified multiple components within pervious concrete. Clogging material content was greater in the top 10 mm, compared to the rest of the pervious concrete cores. Overall, the LID practices evaluated continued to provide stormwater benefits as they aged.

TABLE OF CONTENTS

Chapter Page

Chapter Page

LIST OF TABLES

Table Page

Table Page

LIST OF FIGURES

Figure Page

Figure Page

Figure Page

Figure Page

CHAPTER I

INTRODUCTION

BACKGROUND

Low impact development (LID) has become a predominate stormwater management technique over the past three decades because it goes beyond traditional stormwater goals by utilizing natural processes to improve hydrology and reduce pollutant transport. It is well documented that urbanization can negatively impact stormwater and cause environmental degradation (Paul and Meyer 2001; Walsh et al. 2005; USEPA 1997). Stormwater management is driven by regulations at the city, state, and federal level (USEPA 2017). Traditional stormwater management practices primarily focus on volume and peak discharge management with centralized infrastructure (Roy et al. 2008). In the early 1990's, LID was formaly established in Prince George's County, Maryland and has been implemented widely throughout the area (USEPA 2000). Even though LID techniques have been in practice for over two decades, many questions remain related to effectivness and maintenance as LID stormwater control measures (SCM) age (Ahiablame et al. 2012; Dietz 2007; NAP 2009; Vogel et al. 2015; WEF 2015).

Degradation of waterways from poor stormwater runoff quality prompted the creation of the National Pollutant Discharge Elimination Systems (NPDES) to improve stormwater runoff quality (USEPA 1997; Roy-Poirier et al. 2010). The NPDES led to the formal creation of stormwater best management practices (BMPs) (Roy-Poirier et al. 2010). LID practices have

historically been classified as stormwater BMPs, though the now adopted terminology is stormwater control measures (SCM) (Fletcher et al. 2015). SCM conveys a clearer classification of the practices (Fletcher et al. 2015). Common LID SCMs include bioretention cells (BRCs), permeable pavements (including pervious concrete (PC)), green roofs, vegetated swales, rainwater harvesting, and infiltration trenches.

LID research is an active field, with 9,670 results being returned when searching "low impact development stormwater" on Google Scholar, limiting the search to 2016 to August 4th, 2017. Even with highly active research, there is a general need for research to advance the understanding of LID related to targeted designs and aged of SCMs (Hunt et al. 2012; Vogel and Moore 2016). Additionally, opportunities exist to utilize methodologies from of other fields of science to advance the scientific understanding and application of LID SCMs.

RESEARCH OBJECTIVES AND QUESTIONS

The objectives of this research focus on aged LID SCMs. In this study, the LID SCMs are considered aged because they have been in the field for multiple years. The first objective is to determine and compare the hydraulic performance of two 8-year-old BRCs to post-construction performance using controlled-flood testing. Secondly, pollutant leaching potential of the two aged BRCs will be investigated by measuring, analyzing, and interpreting water quality samples. The remaining objectives are related to 2.5-year-old PC. The first set of objectives related to PC include: evaluate how infiltration rate of PC changes with time, evaluate various cleaning methods and quantify their effectiveness to restore infiltration rate, create statistically significant relationships between clogging and mix design. The second set of PC related objectives involves the application of x-ray computer tomography. The objectives for the PC experiments are: (1) cut cores from each of the PC plots in Tulsa, OK and complete x-ray computer tomography on a section near the surface and a section near the bottom; (2) apply multiple component

segmentation methods to CT images to quantify void space and clogging; (3) assess clogging and internal features of reconstructed images from multiple component segmentation; and (4) statistically relate results from image analysis to mix design and clogging trends.

The research questions addressed in this dissertation are:

1. Does the hydrologic performance of BRCs amended with fly ash degrade with age or vary with wet and dry conditions?
2. Do aged BRCs amended with fly ash leach pollutants when flushed with treated municipal water?
3. Does PC that receives stormwater runoff clog nonuniformly when it is not maintained?
4. What, if any, cleaning methods are effective at restoring the infiltration rate of clogged PC?
5. Can x-ray computerized tomography and Hsieh et al (1998) segmentation methodology be used to classify porosity and clogging material in PC?
6. Are there statically significant correlations between clogging, cleaning, internal characteristics, and mix design of PC?

DISSERTATION FORMAT

The research questions are related in that they address aged LID SCMs, however, the specifics are not interrelated. The research in this dissertation is presented as a collection of three related research papers formatted for publication in peer-reviewed journals. Preceding the three manuscripts are an introduction and literature review. Following the manuscripts are a conclusion, list of references, and appendices. The manuscript titles in order as they appear this dissertation are 1) hydraulic analysis and pollutant leaching potential of two established BRCs amended with fly ash, 2) PC long-term clogging trends and evaluation of cleaning methods, and

3) characterizing PC with x-ray computed tomography, component frequency segmentation, and geostatistics.

REFERENCES

Ahiablame, L. M., Engel, B. A., and Chaubey, I. (2012). "Effectiveness of Low Impact Development Practices: Literature Review and Suggestions for Future Research." *Water, Air, & Soil Pollution*, Springer Netherlands, 223(7), 4253–4273.

Dietz, M. E. (2007). "Low Impact Development Practices: A Review of Current Research and Recommendations for Future Directions." *Water, Air, and Soil Pollution*, Springer Netherlands, 186(1–4), 351–363.

Fletcher, T. D., Shuster, W., Hunt, W. F., Ashley, R., Butler, D., Arthur, S., Trowsdale, S., Barraud, S., Semadeni-Davies, A., Bertrand-Krajewski, J.-L., Mikkelsen, P. S., Rivard, G., Uhl, M., Dagenais, D., and Viklander, M. (2015). "SUDS, LID, BMPs, WSUD and more – The evolution and application of terminology surrounding urban drainage." *Urban Water Journal*, 12(7), 525–542.

Hsieh, H. T., Brown, G. O., Stone, M. L., and Lucero, D. A. (1998). "Measurement of porous media component content and heterogeneity using gamma ray tomography." *Water Resources Research*, 34(3), 365–372.

Hunt, W. F., Davis, A. P., and Traver, R. G. (2012). "Meeting Hydrologic and Water Quality Goals through Targeted Bioretention Design." *Journal of Environmental Engineering*, 138(6), 698–707.

National Academies Press (NAP). (2009). *Urban Stormwater Management in the United States*. Washington, D.C.

Paul, M. J., and Meyer, J. L. (2001). “Streams in the Urban Landscape.” *Annual Review of Ecology and Systematics*, 32(1), 333–365.

Roy, A. H., Wenger, S. J., Fletcher, T. D., Walsh, C. J., Ladson, A. R., Shuster, W. D., Thurston, H. W., and Brown, R. R. (2008). “Impediments and Solutions to Sustainable, Watershed-Scale Urban Stormwater Management: Lessons from Australia and the United States.” *Environmental Management*, Springer-Verlag, 42(2), 344–359.

Roy-Poirier, A., Champagne, P., and Filion, Y. (2010). “Review of bioretention system research and design: Past, present, and future.” *Journal of Environmental Engineering*, 136(9), 878–889.

U.S. Environmental Protection Agency (USEPA). (1997). *Urbanization and Streams: Studies of Hydrologic Impacts*. Washington, D.C.

U.S. Environmental Protection Agency (USEPA). (2000). “Low Impact Development (LID): A Literature Review.” (October), 41.

U.S. Environmental Protection Agency (USEPA). (2017). “National Summary of State Information, Water Quality Assessment and TMDL Information.” Washington, D.C. <https://ofmpub.epa.gov/waters10/attains_nation_cy.control> (Sep. 7, 2017).

Vogel, J. R., Moore, T. L., Coffman, R. R., Rodie, S. N., Hutchinson, S. L., McDonough, K. R., McLemore, A. J., and McMaine, J. T. (2015). “Critical Review of Technical Questions Facing Low Impact Development and Green Infrastructure: A Perspective from the Great Plains.” *Water Environment Research*, 87(9), 849–862.

Vogel, J. R., and Moore, T. L. (2016). “Urban Stormwater Characterization, Control, and Treatment.” *Water Environment Research*, 88(10), 1918–1950.

Walsh, C. J., Roy, A. H., Feminella, J. W., Cottingham, P. D., Groffman, P. M., and Morgan, R. P. (2005). “The urban stream syndrome: current knowledge and the search for a cure.” *Journal of the North American Benthological Society*, 24(3), 706–723.

Water Environment Federation (WEF). (2015). *Rainfall to results: the future of stormwater*. Alexandria, VA.

CHAPTER II

LITERATURE REVIEW

INTRODUCTION

Stormwater is vital to humankind as it provides water to the ecosystems we enjoy and rely on for food and product and shapes the landscape which we live in. The U.S. Environmental Protection Agency (EPA) defines stormwater as,

> "Stormwater runoff is generated from rain and snowmelt events that flow over land or impervious surfaces, such as paved streets, parking lots, and building rooftops, and does not soak into the ground. The runoff picks up pollutants like trash, chemicals, oils, and dirt/sediment that can harm our rivers, streams, lakes, and coastal waters." – USEPA 2017

Urbanization is the primary cause of impervious surfaces and pollution that negatively alter the natural course and composition of stormwater. Polluted or excessive stormwater runoff creates unnatural conditions that change the physical, chemical, and ecological components of a stream (USEPA 1997; Paul and Meyer 2001; Walsh et al. 2005). Urbanization is common in for much of the world; therefore, it is imperative that we develop synergy between economic development and the management of natural processes within our urban zones.

Streams in the urban environment can be physically, chemically, and biologically altered by stormwater runoff (Paul and Meyer 2001; Walsh et al. 2005). The first, and probably the most significant, change is to the hydrology that feeds the stream. As watershed imperviousness increases, the amount of water that would have been infiltration or evapotranspiration becomes runoff. Forested watershed hydrology is approximately 40% evapotranspiration, 25% shallow infiltration, 25% deep infiltration, and 10% runoff on an annual basis (Paul and Meyer 2001). An equivalent watershed that is urbanized to 75-100% imperviousness will have approximately 30% evapotranspiration, 10% shall infiltration, 5% deep infiltration, and 55% runoff (Paul and Meyer 2001). This imbalance in the hydrology increases flash flooding, decreases stream baseflow, and reduces groundwater aquifer recharge (Viessman and Lewis 2003; Walsh et al. 2005).

The geomorphology of a stream transforms because of urbanization. Erosion from construction activities fills streams with sediment. The aggraded stream systems lose habitat and discharge carrying capacity. As construction ceases sediment loading to the stream slows but runoff increases because of increased imperviousness. This causes the newly aggraded channel to degrade which results in channel deepening and widening. These changes destabilize the banks and reduce natural habitat (Paul and Meyer 2001).

Within the urban landscape, there are increased loads of nutrients and other ions that are washed into streams during storm events (Paul and Meyer 2001; Pitt et al. 1995; Sansalone and Buchberger 1997; Walsh et al. 2005). This includes phosphorus and nitrogen from fertilizers, wastewater, and illicit discharges and chloride from road salting. Phosphorus is often the limiting nutrient therefore an increase in phosphorus can cause increased algae growth which leads to eutrophication (Correll 1998). Cars and industrial activities increase the loading of metals (Sansalone and Buchberger 1997). There are other numerous compounds that are sourced from the urban area, some of which have unknown effects on the stream ecosystem. This includes, but

is not limited to, pesticides, polychlorinated biphenyls (PCBs), polycyclic aromatic hydrocarbons (PAHs), petroleum-based aliphatic hydrocarbons, and pharmaceuticals. The chemical impacts combined with the physical changes create unfavorable conditions for the microbes, algae, macrophytes, invertebrates, and fish. Ultimately causing degradation of the stream and river ecosystem (Paul and Meyer 2001; Walsh et al. 2005).

According to the most recent assessment of waters in the United States, 54.9% of assessed rivers were impaired (USEPA 2017). The impacts of urbanization are a leading cause of stream impairment. According to Paul and Meyer (2001), urbanization was the second leading source of impairments, exceeded only by agriculture. This not necessarily surprising because agriculture accounts for a much higher percentage of land use, and the U.S. Streams that are impaired for specific pollutants have load budgets created for them. These pollution budgets are known as a Total Maximum Daily Load (TMDL), and are, as stated, the maximum amount that a water body can receive daily and still meet water-quality standards. There is a positive trend in the number of water bodies with TMDLs (Figure 2.1). This trend is influenced by the rate of urbanization.

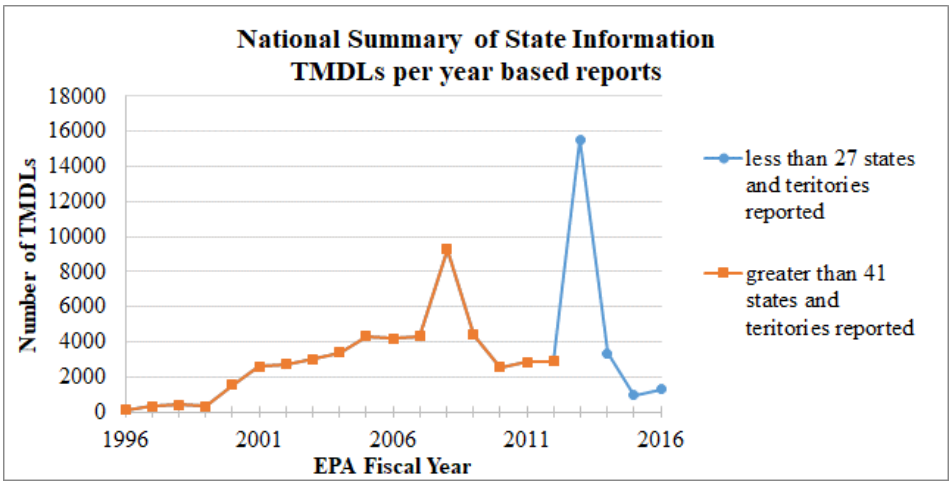

Figure 2.1. Number of Total Maximum Daily Loads (TMDL) reports by states and territories to the U.S. Environmental Protection Agency (USEPA 2017).

With greater than fifty percent of the world's population now residing in urban areas, properly managing stormwater is critical for long-term sustainability and economic growth (National Academy Press 2009; UN DESA 2014). In the United States, approximately seventy percent of the population lives in urban areas (US Census Bureau 2010). This equates to 223 million people. The U.S. urban population lives on only 88,000 square miles of land, which is less than five percent of the U.S. land area (US Census Bureau 2010). It is not surprising, given the high number of people in urban areas, that urban watersheds and streams suffer from overwhelming areas of imperviousness when considering the amount of infrastructure needed for business, homes, and transportation. Urban areas are relatively compact and thus provide the opportunity for significant improvement in a small footprint. This requires the development of innovative and targeted treatment techniques that continue to function as designed year after year.

LOW IMPACT DEVELOPMENT

Low impact development (LID) is a stormwater management approach that includes practices and control measures that are intended to mimic the natural hydrology of altered landscapes. While LID is mainly applied in urban areas, the techniques and practices can be implemented in many landscapes. LID practices include reduced impervious area, urban forest preservation, soil restoration, and disconnecting impervious surfaces. Common LID stormwater control measures (SCMs) include bioretention cells (BRCs), permeable pavements, rainwater harvesting, green roofs, and bioswales. These practices and techniques are widely implemented in the U.S. and throughout the world. In Australia, LID is called Water-Sensitive Urban Drainage and in the United Kingdom, it is called Sustainable Urban Drainage Systems (Fletcher et al. 2015). In China LID often is applied to create 'sponge cities', which indicates the wide speared application of LID practices in city (Ding et al. 2017).

Application of LID practices in Oklahoma are not new, but currently, there are only 49 LID implementations listed on the National Low Impact Development Atlas (Dickson et al. 2011, database accessed 2017-03-28). Of the 49 projects, 26 are BRCs or bioswales (53%) and only 6 (12%) are permeable pavements. This list does not constitute every LID practice in Oklahoma but does provide a general sense of Oklahoma's LID footprint and image to the nation. The national average in the database is 61% bioretention or bioswales and 24% permeable pavements. Oklahoma's implementation of bioretention and bioswales is more similar to the national average, while the permeable pavement implementation is lacking.

Knowing the long-term performance of an LID control measure is important when installed to meet specific water management targets. LID is a proven method, but long-term performance data is variable and limited. The lack of research and application is further limited in the Great Plains and specifically in Oklahoma (Vogel et al. 2015). Because specific water quality targets are becoming more prevalent, understanding how LID control measures change as they age will be critical for long-term success and improving designs to meet future needs.

BIORETENTION CELLS

BRCs are an infiltration based LID technique that have been in practice for over two decades. A BRC is shallow landscape feature that has an inlet, ponding area, soil media, overflow, and often a drainpipe below the soil media. They are sized to store and treat runoff produced by small to medium sized precipitation events on lot-sized catchment areas (Vogel et al. 2015). The volume of runoff to be treated is often the first 25.4 mm (1.0 in) of runoff from the contributing area (Vogel et al. 2015). Stormwater storage capacity of a BRC includes the ponded surface and voids in the soil media. BRC filter media varies, but the main component is a low-fines sandy soil. The sandy soil provides storage and filtration and is the medium which biological and chemical sorption can occur. Infiltration capacity at the surface and percolation through soil media are key

attributes for the long-term application and reliability of BRCs as a SCM. As BRCs age and a biological community develops, the long-term performance may change, which could result in infiltration rates and storage volumes above or below design specifications.

Design specifications

BRCs are shallow depressions in the landscape where stormwater collects and is treated. The primary components of a BRC include the inlet, ponding area, filter media, and overflow (Liu et al. 2014). There different types of BRCs. Major types of BRCs include; infiltration, filtration with bottom underdrain, biofiltration with internal water storage zone, and filtration with sump (OCES 2017). Infiltration systems do not have an underdrain and only function properly when the native underlying soil can drain stored water within 24 hours to 48 hours. Filtration BRCs rely on an underdrain positioned near the bottom of the BRC for sufficient drainage during and after storm events. An internal water storage zone is created with an upturned elbow underdrain, while a sump is created by elevating the entire underdrain above the bottom of the BRC.

Specific design details vary, but the depth of the ponding area typically ranges from 15 cm to 30 cm typically. The ponding area is often planted with wet and dry tolerant plants that are surrounded by shredded hardwood mulch, though, other ground covers include turf grasses and rock mulch (Claytor and Schueler 1996). Filter media blends are mostly sand. Compost and other organic matter have been added in the past, but recent finding indicate nutrient leaching from organic sources in the media (Liu et al. 2014; Ahearn and Rheaume 2014). Modern mix designs limit organic content in filter media (Liu et al 2014). Filter media amendments have been used to improve nutrient and microbial retention (Ahiablame et al. 2012; Youngblood et al. 2017). An underdrain system is needed if the native underlying soil infiltration is low. Liu et al. (2014) reported that 13 mm/hr or less is a common design value for determining underdrain needs.

Restoring urban hydrology

Volume

BRCs provide stormwater benefits by reducing stormwater runoff volume and decreasing peak discharges. Volume reduction is better for small storms compared to larger storms with reductions of up to 100% (Davis et al. 2012; DeBusk and Wynn 2011; Hatt et al. 2009; Winston et al. 2016b). Yearly mean volume retention greater than 60% was reported for eight of the ten research studies reviewed by Dietz (2007). An internal water storage zone can improve volume retention by increasing the storage time in BRCs with an underdrain, which increases exfiltration and evapotranspiration (Brown and Hunt 2011; Wadzuk et al. 2015; Winston et al. 2016b). Lateral exfiltration was reported as the dominate water loss for BRCs in low permeability soils with the use of an internal water storage zone (Winston et al. 2016b). A BRC mesocosm studied by Wadzuk et al. (2015) had an evapotranspiration rate of 50% for a fully drained system.

Flow rate and timing

Peak flow reductions have been reported between 49% to 100%, and lag times and time to peak discharge can be increased (Davis 2008; DeBusk and Wynn 2011; Jarden et al. 2016; Winston et al. 2016b). Davis (2008) found that peak discharge was delayed by more than six times the inlet time to peak for 36% of monitored storms. Jarden et al. (2016) studied the before and after impact of LID at the neighborhood scale. Lag times to peak discharge were not different with the primary reason being that the monitoring time step was too long at 15 mins (Jarden et al. 2016). However, the runoff hydrograph center of mass lag time increased up to 49 minutes after LID was constructed for one of the monitored neighborhoods.

Water quantity performance

BRCs have also been shown to improve stormwater quality. Reports of nitrogen reduction indicated variability with greater reduction for total nitrogen than nitrate (Chen et al. 2013; Davis

et al. 2006; Hsieh and Davis 2005). In some cases, nitrate is exported (Li and Davis 2014). The use of a saturated zone created by an upturned elbow can reduce nitrate in the effluent (Brown and Hunt 2011; Passeport et al. 2009). Phosphorus reduction has been reported by many (Dietz 2007; Hsieh and Davis 2005; Hunt et al. 2008; Randall 2011; Zhang et al. 2008). Though, phosphorus leaching has also been observed (Dietz and Clausen 2006; Hatt et al. 2009; Paus et al. 2014). Phosphorus sorption can be enhanced by including amendments. Fly ash, steel wool, alum, and iron rich soils have been shown to improve sorption (Erickson et al. 2007; Lucas and Greenway 2011; Zhang et al. 2008; Vogel and Moore 2016). Bacteria have been detected in discharged stormwater from the outlet of BRCs, though removal rates from 64% to 97% have been observed (Ahiablame et al. 2012; Youngblood et al. 2017). BRCs are efficient at filtering total suspended solids (TSS) from stormwater (Dietz 2007; Hsieh and Davis 2005; Hunt et al. 2008; Kandel et al. 2017). TSS removal over 90% is not uncommon (Dietz 2007; Hsieh and Davis 2005).

Tests methods

There is a need for standard tests methods for evaluating SCMs (Adair et al. 2014). Individual infiltration rates measurements with a ring infiltrometer can be used to evaluate drawdown rate Jenkins et al. (2010) measured the drawdown rate of a BRC over a three-year period with a ring infiltrometer. They found that infiltration rate had not statistically significantly changed over three years, though measurements statistically varied between locations in the BRC within the same year. Steady-state flood tests are a valid way to quantify BRC hydraulics (Asleson et al. 2009; Christianson et al. 2012; Nichols and Lucke 2016). Asleson et al. (2009) compared the drawdown rate from flood testing to ring infiltrometer test. Two of the three BRCs in Asleson et al. (2009) had comparable results while the ring infiltrometer overestimated the third BRC's infiltration rate. Christianson et al. (2012) used steady-state flood testing to calibrate and validate a hydraulic model. Nichols and Lucke (2016) successfully flooded small 10-year old BRCs with

synthetic stormwater to measure pollution reduction of synthetic stormwater and infiltration rate. In Nichols and Lucke (2016) flooding study, total suspended solids and total nitrogen increased while total phosphorus decreased when the synthetic stormwater had no pollutants added to it. Concentrations were reduced from inlet to underdrain when the synthetic stormwater was spiked with pollutants.

PERVIOUS CONCRETE

Pervious concrete (PC) is an engineered structural surface that has a network of interconnected pores that allow rapid water drainage. The voids enable storage and infiltration of stormwater making PC a LID technology for stormwater management. PC was not initially created as a stormwater management tool, but as building material. The first reported use of PC in 1852, though intensive use did come about until the 1940's and 1950's (Ghafoori and Dutta 1995). During this time, PC was known as no-fines concrete and was used to construct building a to reduce cost as after World War II (Ghafoori and Dutta 1995). The use of PC for stormwater management in the U. S. came about in the mid 1970's as course overlays. Interest in PC as a conduit for stormwater infiltration has increased over the past two decades as urbanization increases and with the development of improved mix designs (Ghafoori and Dutta 1995; Tennis et al. 2004; Dietz 2007; Kia et al. 2017). PC is also being utilized for other applications. A unique example of this is the application of PC for the creation of artificial reefs for algae farming (Taniguchi et al. 2001). Even with varied uses, PC mixes have similar design specifications.

The basic components of Portland cement based PC are aggregate, Portland cement, and water (Ferguson 2005). PC is created by having proportions of aggregate to cement (A:C) between 2 to 12 and water to cement (W:C) between 0.2 to 0.5 (Kia et al. 2017; Permeable Pavements Task Committee 2015). PC is typically constructed of a narrowly-graded coarse aggregate with D_{50} of 5.75 mm ($3/8^{th}$ inch). Void content is typically around 20%. Sand, water reducers, air entertainers,

and fly ash may be added in addition to the basic components. Sand content may be added at 5% to 10% of the total aggregate content to improve freeze thaw resistance (Permeable Pavements Task Committee 2015). Mix designs have been investigated for strength, freeze thaw resistance, surface finish, albedo, heat island effects, and void content (Bonicelli et al. 2015; Boriboonsomsin and Reza 2007; Dean et al. 2005; Zhang et al. 2015). Increasing voids results in decreased strength but increase infiltration rate (Kia et al. 2017; Schaefer et al. 2006). Sand and fibers can increase freeze thaw resistance (Dean et al. 2005). Additionally, including sand can increase mechanical strength and improve surface finish, though, it reduces infiltration (Bonicelli et al. 2015).

A typical PC system is composed of the top layer of PC, an aggregate base, and separating layer between aggregate and underlying soil. The thickness of the PC layer is based on the structural strength needed for the anticipated driving load, where a parking lot is typically 4 to 6 inches thick (Ferguson 2005). Below the concrete layer is a crushed aggregate base that serves two purposes. It distributes the driving load to the underlying non-compacted native soil and is a reservoir for stormwater storage. Often there is an underdrain in the crushed aggregate layer to drain excess stormwater and ensure there is storage space for successive storm event. The underdrain either drains water from the bottom of the aggregate layer or from an elevated level. The purpose of an elevated underdrain is to increase exfiltration through the native soil and prevent water from backing up into the PC.

Long-term performance

A critical question regarding the implementation and success of PC is performance over time (Li et al. 2017). This includes the how it clogs, what changes occur to infiltration rate, does the surface deteriorate, and how often it needs maintenance. Infiltration rates for PC can vary greatly, with values over 84.7 cm/min (2000 in/hr) to near 0 cm/min for clogged systems (Chopra et al.

2010; Ferguson 2005). Typical design values are on the order of a 4.23 cm/min to 21.2 cm/min (100 in/hr to 500 in/hr) (Permeable Pavements Task Committee 2015). Infiltration rate has been shown to increase exponentially with increasing voids (Neithalath et al. 2010a). Additionally, clogging can drastically reduce infiltration rate.

Clogging

Clogging is the result of the clogging particle type and size, pore size and connectivity, mix design, and stormwater runon quality (Kia et al. 2017). In some cases, clogging is intentional. PC has been applied as the surface filter layer for groundwater recharge facilities in the United States and other countries (Hogland and Niemczynowicz 1986; Teng and Sansalone 2004). This application of PC is termed a unit superstructure. Teng and Sansalone (2004) showed that PC can act as a filter, but there is a need to quantify the clogging rate and particles that were collected from the schmutzdecke. In a laboratory study, Sansalone et al. (2012) found that 80% of sediment was filtered by PC and that 100% of particles were filtered for particles greater than 300µm. Welker et al. (2013) also studied clogging. They found that the majority of the particles removed from the pore space were raveled particles, pieces of the PC, but they highlighted the benefits of clogging; filtration and sorption of pollutants to clogged particles.

Multiple studies have investigated clogging PC that has was not intentionally used as a filter (Balades et al. 1995; Boogaard et al. 2014; Coughlin et al. 2012; Kumar et al. 2016; Lin et al. 2016; Sansalone et al. 2012; Suozzo and Dewoolkar 2012). PC evaluated by Kumar et al. (2016) exhibited a linear relationship between clogging and time over a four-year period. Winston et al. (2016a) and Lim et al. (2015) found that an exponential curve fit the decrease in infiltration rate versus time best. The PC in these studies did not receive runoff from impervious surfaces.

There are many studies that researched clogging in a laboratory setting (Andrés-Valeri et al. 2016; Aryal et al. 2015; Coughlin et al. 2012; Deo et al. 2010; Haselbach 2010; Haselbach et al.

2006; Lim et al. 2015; Nichols et al. 2015; Yong et al. 2008, 2013). Studies that utilize synthetic stormwater and laboratory mixed concrete are limited in their applicability to field installations and large-scale maintenance practices. Laboratory studies have shown that clay clogging is less likely because the particles can pass through the pore, though when clay clogged, the sediments often clog below the surface layer (Coughlin et al. 2012). Though, high levels of clay can cause surface clogging (Haselbach 2010).

Clogging mechanisms and type of clogging material are becoming more actively researched (Kia et al. 2017). Kia et al. (2017) concluded in their review of PC clogging that particles, sized similar to the pore size of the PC, are more likely to cause clogging. Clogging occurs because the particles can enter a pore but not travel through to the underlying rock base. Even though clogging is a major concern for long-term PC research, some have shown that clogged PC is often not the limit layer (Bean et al. 2007; Coughlin et al. 2012; Kia et al. 2017). Instead, the subbase or the underlying native soil are the flow restricting layer, both of which can clog.

Cleaning

Clogged PC can be cleaned to restore infiltration rate. Many studies have evaluated different cleaning methods (Chopra et al. 2010; Haselbach 2010; Hein et al. 2013; Kumar et al. 2016; Suozzo and Dewoolkar 2012; Winston et al. 2016a). Haselbach (2010) showed that infiltration could be restored with sweeping alone because the clogging was near the surface. Others had less success with sweeping alone, but recommend pressure spraying and vacuuming. From a brief literature review, Kumar et al. (2016) recommend pressure spraying water and then suction. Winston et al. (2016a) showed that high-pressure spraying water and vacuuming was an effective way to restore infiltration rate, but the spraying water and vacuuming occurred on a slight delay rather than simultaneously. Pressure washing with water and vacuuming were found to work better together than either independently by Hein et al. (2013). Suozzo and Dewoolkar (2012)

restored the infiltration to 100% of the initial infiltration rate with pressure washing followed by vacuuming. There are many examples showing that a combination of cleaning with spraying water and vacuuming in a single process is effective, but no study has examined the use of a Vactor truck and standard attachments that municipalities may already own.

Characterization of internal features

Destructive methods

Destructive methods involve cutting PC cores to expose internal material. The surface of the cut is polished and then scanned to create digital images of the surface. Many have utilized this methodology to quantify prosody and other pore size parameters with depth in PC (Sumanasooriya and Neithalath 2009, Sumanasooriya et al. 2010, Deo and Neithalath 2010, Kayhanian et al. 2012, Radlińska et al. 2012, Rehder et al. 2014). From the scanned images, porosity and other internal characteristics can be quantified.

Radlińska et al. (2012) evaluated nine PC cores to determine porosity change with depth. Porosity in the upper 1.5 inches ranged from 1% to 10.8% with porosities near the bottom as high as 25.5% but as low as 1.4% (cement to aggregate ratio varied between samples). Haselbach and Freeman (2006) showed that porosity increased in the vertical direction from top to bottom because of compaction during installation. However, porosity can be lower near the bottom because of cement paste drain down (Kia et al. 2017). Cement paste drain down occurs when the water to cement ratio is too high. A limitation of the destructive method is low vertical resolution. Reporated vertical resolutions range from 37.5 mm to 50 mm (Sumanasooriya and Neithalath 2009; Sumanasooriya et al. 2010; Rehder et al. 2014). Additionally, segmentation of void content and solid content is not well defined for surface-scanned cut cores, though, the results are indicated to be validated with visual inspection. Slogging material cannot be accurately accessed because the cutting process can disturb loose particles.

Computer tomography methods

Computed tomography (CT) imaging is the process of taking multiple radiograms and creating two-dimensional images, the cross-section of material densities. A radiogram is an array of all attenuation values that represent the sum of all densities along multiple, often parallel, paths through a material. Gamma and x-ray light emitting and detecting systems are the most common, with x-ray systems being more common than gamma-ray systems. Tomograms of porous media have also been investigated with neutron, resistive, and ultra-sound imaging (Anderson and Hopmans 2013).

CT imaging has been applied to porous media to quantify pore characteristics (Udawatta et al. 2013). Udawatta et al. (2013) imaged the same cores at 190, 74, and 9.6 μm resolutions to quantify pore connectivity and quantity as well as tortuosity. The 190 μ m resolution was adequate for pore number, two-dimensional feature recognition, and pore area, though the 9.6 μm resolution provided information on the pore geometry, tortuosity, and connectivity. CT imaging has been applied to identify and map micro-porosity by coupling it with microscopy.

Pervious concrete studies

The use of x-ray CT imaging for PC research is a more recent relative to CT research as a whole, which dates back to 1973 (Hounsfield 1973). Analysis of pore space with x-ray CT imaging has been applied to PC by researchers (Ahn et al. 2014; Chandrappa and Biligiri 2017; Kuang et al. 2011, 2015; Manahiloh et al. 2012; Sansalone et al. 2008; Teng and Sansalone 2004). Teng and Sansalone (2004) analyzed 20 cross sections of a 69.09 mm core that had a porosity of 0.258 using x-ray tomography. They found that the majority of the pores were approximately 5 mm^2 in area, though some were measured up to 45 mm^2. Sansalone et al. (2008) examined porosity, filtration, and hydraulics of PC cores. Particularly, the hydraulics were studied based on clogging potential and the effective porosity, tortuosity, and pore size distribution. This study imaged 19

cores from field installed PC. Images were collected at a vertical spacing of 0.5 mm and reconstructed at horizontal resolution of 30 μm. Images gathered by Sansalone et al. (2008) were later used by Kuang et al. (2011, 2015) to model the pore structure and relate hydraulic conductivity to total and effective porosity. Porosity profiles were created using x-ray imaging of seven field cores by Kayhanian et al. (2012). The cores were denser near the surface compared to the bottom. In some cases, the upper porosity was less than half the average porosity.

Meulenyzer et al. (2012) x-ray imaged cores made in the lab to relate mix aggregate size to pore size, permeability, porosity, compressive strength, and specific surface area. The voxel resolution was 140 μm. Compressive and tensile strength of PC was examined with x-ray CT by Agar-Ozbek et al. (2013) to view fracture location and patterns. Additionally, gray scale values were correlated to material properties to quantify the composition of the samples. Reported resolution of the scanning equipment was 0.5 μm/voxel. Ahn et al. (2014) imaged laboratory constructed cores with two different x-ray CT machines; one at 450 kV and the other at 225 Kv. They reported that the images were better from the 450 kV system.

Understanding the porosity of PC does not directly produce information regarding the size and shape of the pores within PC. Many studies have characterized pore size and shape (Teng and Sansalone 2004; Sansalone et al. 2008; Sumanasooriya and Neithalath 2009; Neithalath et al. 2010b; Kuang et al. 2011, 2015; Meulenyzer et al. 2012). Common methods include equivalent pore size, two-point correlation function, and granulometry. Teng and Sansalone (2004) analyzed 20 cross sections of a single 69.09 mm using x-ray tomography. The average porosity was determined to be 26% for their cores. They found that most pores were approximately 5 mm^2 in area, though some were measured up to 45 mm^2. This work was followed up by Kuang et al. (2011) through the modeling of pore structure and relating hydraulic conductivity to total and effective porosity. The d_{50} representing their cores was 3.4 mm.

Total and effective porosity, tortuosity, pore size distribution, and specific surface area of PC using x-ray tomography were measured by Kuang et al. (2015). This study examined image resolution and its impact on pore size, total porosity, and specific surface area. Specific surface area is the pore surface area divided by the total volume. The cores were backwashed and porosity was gravimetrically measured prior to imaging. Images were collected on fan beam x-ray tube at 250kV and at a vertically spacing of 0.5 mm. They found that the d_{50} was independent of resolution when based on the weighted area of the pores. Image reconstruction resolution ranged from 35 to 558 μm. Additionally, effective and total porosity was not a function of resolution. This implies that the small pores captured by the finer resolution have limited impact on the hydraulics of the system.

Meulenyzer et al. (2012) x-ray imaged cores made in the lab to relate mix aggregate size to pore size, porosity, and specific surface area. The voxel resolution was 140 μm. They utilized a two-point correlation (TPC) method to determine a representative pore size. Lengths ranged from 0.38 to 1.26 mm for cores with porosities ranging from 22.8% to 35.3%. TPC method has also been applied to PC images by Sumanasooriya and Neithalath (2009). Neithalath et al. (2010) and Deo et al. (2010) analyzed pore size with the TPC function and granulometry. Granulometry involves placing a circle in each void space with a radius of length *l* and then incrementally increasing the radius length. The radius at which the pore no longer surrounds the circle is the assumed pore diameter for that specific pore. Neithalath et al. (2010) found that the TPC function more closely matched the d_{50} from equavivalent pore size than did the characteristic length from granulometery. Characteristic lengths ranged from 1.5 mm to 3.6 mm.

Manahiloh et al. (2012) analyzed x-ray CT images of clogged PC. Based on the porosity from segmented images, clogging had occurred throughout the entire core except in the top 25 cm. Clogging was not directly identified, but inferred from porosity measurements. Porosity was

determined with Otsu image segmentation (Manahiloh et al. 2012; Otsu 1979). Manahiloh et al. (2012) includes many useful figures showing the reconstructed x-ray images. The reconstructed images have noticeable beam hardening on the edges, which appears to have affected the segmentation results (see Figures 7 and 8 in Manahiloh et al. 2012).

Segmentation thresholding is an image process technique that has been used to determine heterogeneity and material quantities (Ahn et al. 2014; Hsieh et al. 1998a, 1998b; Iassonov et al. 2009; Kuang et al. 2015; Tuller et al. 2013). Segmentation is described by Tuller et al. (2013) as the most critical step in CT image analysis prior to any quantification. In short, there are two basic techniques for segmentations. Either images are segmented into binary images or voxels are categorized into multiple categories. Regardless of the number of segmentations, attenuation values are assigned a new discrete value based on threshold levels (Iassonov et al. 2009). The quantity of voxels within each segmentation range can then easily be quantified. Over 100 segmentation methods were reported in literature in 2013, though most were developed for medical or object recognition applications (Tuller et al. 2013). Table 2.1 lists the image acquisition and segmentation method of PC research.

Table 2.1. List of image acquisition method and segmentation (or other method) used to quantify internal characteristics of pervious concrete.

Reference	Image type	Segmentation or other porosity method
Neithalath et al. (2006)	cut and scanned	Segmentation method not specified. Gravimetric was used as validation
Sumanasooriya and Neithalath (2009)	cut and scanned	Manual segmentation.
Deo and Neithalath (2010)	cut and scanned	References Deo et al. 2010
Deo et al. (2010)	cut and scanned	References Sumanasooriya and Neithalath 2009
Neithalath et al. (2010a)	cut and scanned	Not specified. Used a NIST program
Neithalath et al. (2010b)	cut and scanned	Manual segmentation.
Sumanasooriya et al. (2010)	cut and scanned	Manual segmentation.
Sumanasooriya and Neithalath (2009)	cut and scanned	Manual segmentation.
Kayhanian et al. (2012)	cut and scanned	Segmentation method not specified. Gravimetric was used as validation
Radlińska et al. (2012)	cut and scanned	Manual porosity by filling pores in Adobe Photoshop
Rehder et al. (2014)	cut and scanned	Segmentation method not specified. Gravimetric was used as validation
Teng and Sansalone (2004)	x-ray CT	Segmentation method not specified.
Schaefer et al. (2006)	x-ray CT	Not specified
Sansalone et al. (2008)	x-ray CT	Segmentation method not specified. Gravimetric was used as validation
Kuang et al. (2011)	x-ray CT	References Sansalone et al. 2008
Meulenyzer et al. (2012)	x-ray CT	Segmentation method not specified. Gravimetric was used as validation
Manahiloh et al. 2012	x-ray CT	Otsu (1979)
Ahn et al. (2014)	x-ray CT	Otsu (1979)
Kuang et al. (2015)	x-ray CT	Bayes decision theory of pattern recognition (Jain and Dubuisson 1992; Sauer and Bouman 1992; Iassonov et al. 2009)
Chandrappa and Biligiri (2017)	x-ray CT	Segmentation method not specified. Gravimetric was used as validation
Abera et al. (2017)	x-ray CT	Otsu (1979), Pun (1980), Kapur et al. (1985), Johannsen and Bille (1982), and Kittler and Illingworth (1986)

There are two classes of segmentation methods commonly utilized in porous media research; global and locally adaptive. Global methods incorporate data from the entire image for thresholding. Otsu (1979) thresholding technique, a global method, was used to distinguish void locations in PC (Ahn et al. 2014; Manahiloh et al. 2012). The automated thresholding technique developed by Otsu (1979) segments images based on the zeroth and first-order moments of an image's gray scale histogram. Abera et al. (2017) examined the effectiveness of two global thresholding techniques, Otsu (1979) and Kupar et al. (1985), on their ability to classify porosity of PC. Kupar's method was determined to be the most accurate, though, Otsu's method performed better on a column of packed beads. Regardless of the method, the two thresholding techniques only segmented the images into two materials; voids and solid material. There was also visual evidence of beam hardening at the outer edges of the PC cores shown in Figure 5 of Abera et al. (2017), which appears to have affected the segmentation results.

Locally adaptive methods are similar to global methods except that segmentation occurs on a local matrix of voxel values. Indicator kriging, probabilistic fuzzy C-means clustering, edge detection, active contours, and supervised Bayesian segmentation based on the Markov random field framework are locally adaptive methods that have been used to quantify porous media (Tuller et al. 2013). Edge detection based Bayes decision theory was utilized by Kuang et al. (2015) to identify the pores of PC cores. These techniques generate two component binary images, from which the sum of the segmented portions can be easily calculated.

Multiple component segmentation has not been applied to PC. Hsieh et al (1998a) segmented multiple materials from CT images by fitting theoretical histograms to CT images. The segmentation method developed by Hsieh et al. (1998a) allowed for the accurate quantification of gypsum, dolomite, and mixed-components. This method relies heavily on the fundamentals of the creation of CT images from high energy photo sources (x-ray and gamma ray). A brief

explication of CT image capture and reconstruction is presented here because an understanding of how individual voxel values are assigned is important when considering the segmentation methodology and quantifying internal structure from binary images.

Computer tomography theory

Reconstruction of an image is achievable because attenuation of photons is proportional to material density, measured attenuation is a sum of all possible attenuations at the location of the beam, and the integral of all possible projections across a two-dimensional function is composed of unique values. Therefore, individual density values are obtainable by taking the inverse of the measured function. In 1917, Johann Radon (1986) developed proofs showing that the line integral of a series of integrals is a unique transformation of those values. Thus, individual values are obtainable by taking the inverse of what is now known as the Radon function. Hounsfield (1973) and Ambrose (1973) applied this theory to x-ray imaging to create the first computerized two-dimensional scans of the human brain. Figure 2.2 illustrate the basic concept of CT imaging a circular core that contains a denser region (black dot) with a pencil beam photon source.

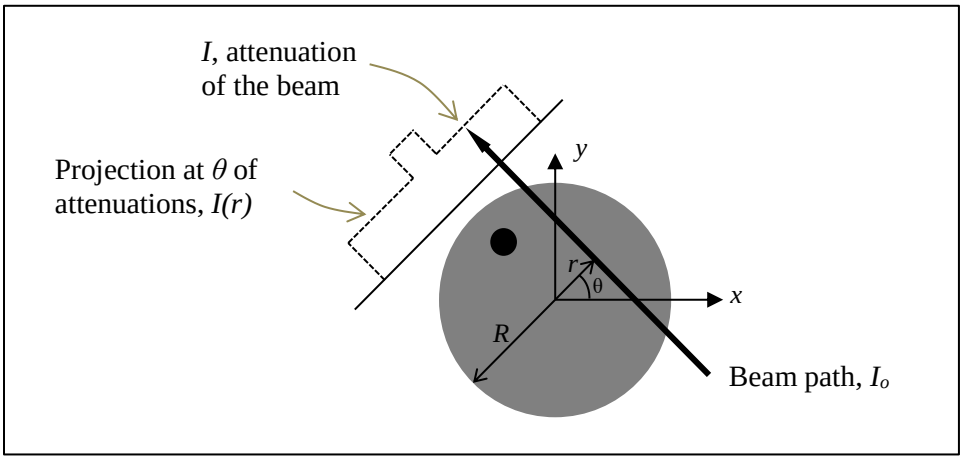

Figure 2.2. Computed tomography single beam imaging schematic and illustrative projection of a circular object with denser object (black dot) within it.

Attenuation of photons is proportional to the density of the material and is defined by Lambert's law (ASTM 2011). For a single beam of photons that pass through a medium the line integral of all attenuation I is

$$I(r,\theta) = I_0 \exp\left(-\int \mu(x,y)ds\right) \tag{2.1}$$

where I_o is the source intensity, $\mu(x,y)$ is the attenuation at location x and y, r is the radial distance from the center to the tangent of the beam path, and s is the beam path. A projection, p, of attenuation values along r is the line integral and is created by varying r for a constant θ. A single projection is defined as

$$p(r,\theta) = \int (\mu(x,y)ds) \tag{2.2}$$

Multiple projections are needed to reconstruct an image. All unique projections can be obtained by incrementing θ between 0 and π.

$$p(r,\theta) = \int_0^{\pi} \int (\mu(x,y)ds) \tag{2.3}$$

The attenuation at any point (x, y) is obtained by back projecting Eq. 2.3 through the space.

$$\mu(x,y) = \int_0^{\pi} \int_{-\infty}^{\infty} p(r,\theta)\, q(x\cos\theta + y\sin\theta - r)\; dr \tag{2.4}$$

where q is a filter function. This method is called convolution-backprojection with a filter and is the most common, though methods others exist (ASTM 2011). The purpose of the filter is to sharpen the convoluted image which is blurred. The basic form of the filter is

$$q(r) = \frac{\pi^2}{2}\left(\frac{\delta(r)}{r} - \frac{1}{r^2}\right) \tag{2.5}$$

where $\delta(r)$ is the Dirac delta function. This is a weighted function that maintains the original information while suppressing the response at a distance of r^{-2}. Many reconstruction and filter methods exist (Lewitt 1983; Tuller et al. 2013), all of which can improve image sharpness. The fastest and most common approach to transfer the projections to Fourier domain with a Fast-Fourier Transformation, apply a filter to increase flow frequency data, and then transfer back to the spatial domain to complete the backprojection (ASTM 2011).

The accuracy of attenuation values is a function of the resolution of the beam and detector, reconstruction resolution, accuracy of the attenuation measurement instrumentation, and the accuracy of the reconstruction (ASTM 2011). Image accuracy decreases because of noise (i.e. normal variations among the data) and artifacts created by variations within the material being imaged, equipment configuration, and image reconstruction. The reconstruction process, as mentioned previously, requires numerical reconstruction and interpolation between or averaging of line integral values, which can result in reduced image accuracy. In addition to issues with accuracy, there are uncertainties of the true proportion of components within a voxel.

Measured attenuation values for a given voxel are dependent upon the material and density within the voxel space. Partial-volume imaging occurs when multiple materials with different density exist in a voxel (Ketcham and Carlson 2001). The attenuation value assigned to that voxel does not represent the true density of material but rather the average density within the voxel space (Brown et al. 1993). Partial-volume reduces contrast of the image and can make material identification complicated. The existence of attention values that occur outside of known material density may be identified as partial-volume errors, though knowing the exact proportion of a material that passes through the partial-volume is not quantifiable. Partial-volume effects are more problematic for very heterogeneous materials and may prevent proper thresholding analysis (Hsieh et al. 1998a; b; Ketcham and Carlson 2001). In PC, mixed component voxels will occur at

the interface between materials. This causes uncertainty when trying to identify the true component content of voxel at the interface between voids and solids. Partial volume voxels can be improperly classified which would lead to inaccurate void and solid content classification. Additionally, clogged PC would be expected to have many edges and partial volume voxel, making quantification difficult.

Meulenyzer et al. (2012) x-ray imaged cores made in the lab to relate mix aggregate size to pore size, permeability, porosity, compressive strength, and specific surface area. The voxel resolution was 140 μm. They utilized a two-point correlation method to determine a representative pore size. This process involves randomly placed different length lines on the image and determines if both ends fall within the same material. Lengths ranged from 0.38 to 1.26 mm. Neithalath et al. (2010) segmented pore sizes with a two-point correlation function and granulometry. Granulometry involves placing a circle in each void space with a radius smaller than the pore and then incrementally increasing the radius. The radius at which the pore no longer surrounds the circle is the assumed pore diameter for that specific pore. The critical pore diameter is calculated as the 50th percentile of the pore distribution. TPC methods have been applied to images in research by Sumanasooriya and Neithalath (2009) and Meulenyzer (2012). Akand et al. (2016) imaged PC cores with a microCT system. Pore location and area was determined and used to make a Fast Fourier Transformation (FFT) distribution. The FFT distribution was then used to create a finite element model of the strength, stiffness, and permeability. Methodologies that do not rely on segmented images have not been explored in PC research.

The use of CT for porous media research is a large field with many techniques that have not been applied to PC (Iassonov et al. 2009; Tuller et al. 2013). Common techniques such as the TPC, tortuosity, and sphericity require image segmentation, which as discussed previously is not often well defined or can have potential accuracy errors. An alternative method is to apply geostatistics

directly to attenuation values measured by the x-ray CT systems. One example is the semivariogram. Vogel et al. (2003) utilized semivariograms to quantify the relative elementary volume of rock cores. Such techniques may be useful for advancing the understanding of internal features of PC without introducing errors through segmentation.

CONCLUSIONS

With an increasing urban population and number of water bodies with TMDLs, there is an immediate need to for targeted LID SCMs designs that will function as designed for many years. This literature covers many topics of LID research. A common theme among research gaps is how LID SCMs will perform as they age and what maintenance will be needed. BRCs are heavily researched, with many results indicating the positive benefits of volume and peak flow mitigation and pollution reduction. However, there is uncertainty related to the performance of amended filter media BRCs. Additionally, testing infiltration rate can be variable when multiple discrete locations are measured. This can be avoided by flooding the entire surface.

Urban landscapes are covered with hardscape impervious surfaces that alter stormwater. PC has been shown as an alternative surface and has gained popularity over past two decades. While mix design for strength and durability have improved, there is a lack of research focused on clogging, cleaning, and mix design. The internal structure of PC has been well documented by destructive and nondestructive techniques; mainly x-ray CT. There, however, are two gaps in the nondestructive research; 1) segmentation techniques for quantifying porosity are often not clearly identified or rely on global methods that do not account for photon statistical errors and 2) clogging has not been directly quantified, but indirectly identified as changes to the porosity. CT has been around for decades and there exist many techniques related to porous media that may be useful for the advancement of PC design.

REFERENCES

Abera, K. A., Manahiloh, K. N., and Motalleb Nejad, M. (2017). "The effectiveness of global thresholding techniques in segmenting two-phase porous media." *Construction and Building Materials*, Elsevier Ltd, 142, 256–267.

Adair, R., Janoch, R., French, C., Lenhart, J., Kloss, C., Brown, C., Jadlocki, S., Sandu, A., Roseen, R., Belan, G., and Brown, S. (2014). Investigation into the Feasibility of a National Testing and Evaluation Program for Stormwater Products and Practices.

Agar-Ozbek, A. S., Weerheijm, J., Schlangen, E., and Van Breugel, K. (2013). "Investigating porous concrete with improved strength: Testing at different scales." *Construction and Building Materials*, 41, 480–490.

Ahearn, D., and Rheaume, A. (2014). "Characterization of pollutant flushing from a newly installed bioretention system: 185th Ave NE, Redmond, WA." *Salish Sea Ecosystem Conference*.

Ahiablame, L. M., Engel, B. A., and Chaubey, I. (2012). "Effectiveness of Low Impact Development Practices: Literature Review and Suggestions for Future Research." *Water, Air, & Soil Pollution*, Springer Netherlands, 223(7), 4253–4273.

Ahn, J., Jung, J., Kim, S., and Han, S. (2014). "X-Ray Image Analysis of Porosity of Pervious." *International Journal of GEOMATE*, 6(1), 796–799.

Akand, L., Yang, M., and Gao, Z. (2016). "Characterization of pervious concrete through image based micromechanical modeling." *Construction and Building Materials*, Elsevier Ltd, 114, 547–555.

Ambrose, J. (1973). “Computerized transverse axial scanning (tomography): Part 2. Clinical application.” *The British Journal of Radiology*, 46(552), 1023–1047.

American Society for Testing and Materials (ASTM). (2011). “ASTM E1441-11: Standard Guide for Computed Tomography (CT) Imaging.” (July), 1–33.

Anderson, S. H., and Hopmans, J. W. (2013). *Soil–Water–Root Processes: Advances in Tomography and Imaging*. SSSA Special Publication, The Soil Science Society of America, Inc.

Andrés-Valeri, V., Marchioni, M., Sañudo-Fontaneda, L., Giustozzi, F., and Becciu, G. (2016). “Laboratory Assessment of the Infiltration Capacity Reduction in Clogged Porous Mixture Surfaces.” *Sustainability*, 8(8), 751.

Aryal, R., Beecham, S., and Lee, B. K. (2015). “Evaluation of particle transport in permeable pavements under oil loadings.” *KSCE Journal of Civil Engineering*, 19(7), 2000–2004.

Asleson, B. C., Nestingen, R. S., Gulliver, J. S., Hozalski, R. M., and Nieber, J. L. (2009). “Performance Assessment of Rain Gardens.” *JAWRA Journal of the American Water Resources Association*, Blackwell Publishing Ltd, 45(4), 1019–1031.

Balades, J., Legret, M., and Madiec, H. (1995). “Permeable pavements: Pollution management tools.” *Water Science and Technology*, 32(1), 49–56.

Bean, E. Z., Hunt, W. F., and Bidelspach, D. A. (2007). “Field Survey of Permeable Pavement Surface Infiltration Rates.” *Journal of Irrigation and Drainage Engineering*, 133(3), 249–255.

Bonicelli, A., Giustozzi, F., and Crispino, M. (2015). “Experimental study on the effects of fine sand addition on differentially compacted pervious concrete.” *Construction and Building Materials,* Elsevier Ltd, 91, 102–110.

Boogaard, F., Lucke, T., and Beecham, S. (2014). “Effect of Age of Permeable Pavements on Their Infiltration Function.” *CLEAN - Soil, Air, Water,* 42(2), 146–152.

Boriboonsomsin, K., and Reza, F. (2007). “Mix Design and Benefit Evaluation of High Solar Reflectance Concrete for Pavements.” *Transportation Research Record: Journal of the Transportation Research Board*, Transportation Research Board of the National Academies, 2011, 11–20.

Brown, G. O., Stone, M. L., and Gazin, J. E. (1993). “Accuracy of gamma ray computerized tomography in porous media.” *Water Resources Research*, 29(2), 479–486.

Brown, R. A., and Hunt, W. F. (2011). “Underdrain Configuration to Enhance Bioretention Exfiltration to Reduce Pollutant Loads.” *Journal of Environmental Engineering*, 137(11), 1082–1091.

Chandrappa, A. K., and Biligiri, K. P. (2017). “Relationships Between Structural, Functional, and X-Ray Microcomputed Tomography Parameters of Pervious Concrete for Pavement Applications.” *Transportation Research Record: Journal of the Transportation Research Board*, 2629(2629), 51–62.

Chen, X., Peltier, E., Sturm, B. S. M., and Young, C. B. (2013). “Nitrogen removal and nitrifying and denitrifying bacteria quantification in a stormwater bioretention system.” *Water Research,* Elsevier Ltd, 47(4), 1691–1700.

Chopra, M., Kakuturu, S., Ballock, C., Spence, J., and Wanielista, M. (2010). “Effect of Rejuvenation Methods on the Infiltration Rates of Pervious Concrete Pavements.” *Journal of Hydrologic Engineering*, 15(6), 426–433.

Christianson, R. D., Brown, G. O., Chavez, R. A., and Storm, D. E. (2012). “Modeling Field-Scale Bioretention Cells with Heterogeneous Infiltration Media.” *Transactions of the ASABE*, 55(4), 1193–1201.

Claytor, R. A., and Schueler, T. R. (1996). *Design of Stormwater Filtering Systems*. *Environmental Protection*.

Correll, D. L. (1998). “The Role of Phosphorus in the Eutrophication of Receiving Waters: A Review.” *Journal of Environment Quality*, 27(2), 261.

Coughlin, J. P., Campbell, C. D., and Mays, D. C. (2012). “Infiltration and Clogging by Sand and Clay in a Pervious Concrete Pavement System.” *Journal of Hydrologic Engineering*, 17(1), 68–73.

Davis, A. P. (2008). “Field Performance of Bioretention: Hydrology Impacts.” *Journal of Hydrologic Engineering*, 13(2), 90–95.

Davis, A. P., Shokouhian, M., Sharma, H., and Minami, C. (2006). “Water Quality Improvement through Bioretention Media: Nitrogen and Phosphorus Removal.” *Water Environment Research*, 78(3), 284–293.

Davis, A. P., Traver, R. G., Hunt, W. F., Lee, R., Brown, R. A., and Olszewski, J. M. (2012). “Hydrologic Performance of Bioretention Storm-Water Control Measures.” *Journal of Hydrologic Engineering*, 17(5), 604–614.

Dean, S., Montes, F., Valavala, S., and Haselbach, L. (2005). “A New Test Method for Porosity Measurements of Portland Cement Pervious Concrete.” *Journal of ASTM International*, 2(1), 12931.

DeBusk, K. M., and Wynn, T. M. (201). “Storm-Water Bioretention for Runoff Quality and Quantity Mitigation.” *Journal of Environmental Engineering*, 137(9), 800–808.

Deo, O., and Neithalath, N. (2010). “Compressive behavior of pervious concretes and a quantification of the influence of random pore structure features.” *Materials Science and Engineering A*, Elsevier B.V., 528(1), 402–412.

Deo, O., Sumanasooriya, M., and Neithalath, N. (2010). “Permeability Reduction in Pervious Concretes due to Clogging: Experiments and Modeling.” Journal of Materials in Civil Engineering, 22(7), 741–751.

Dickson, D. W., Chadwick, C. B., and Arnold, C. L. (2011). “National LID Atlas: A Collaborative Online Database of Innovative Stormwater Management Practices.” *Marine Technology Society Journal*, 45(2). Database access 2017-03-28.

Dietz, M. E. (2007). “Low Impact Development Practices: A Review of Current Research and Recommendations for Future Directions.” *Water, Air, and Soil Pollution*, Springer Netherlands, 186(1–4), 351–363.

Dietz, M. E., and Clausen, J. C. (2006). “Saturation to Improve Pollutant Retention in a Rain Garden.” *Environmental Science & Technology*, American Chemical Society, 40(4), 1335–1340.

Ding, L. H.,, Ren, M., Li, C., and Wang, H. (2017). “Sponge City Construction in China: A Survey of the Challenges and Opportunities.” *Water*, Multidisciplinary Digital Publishing Institute, 9(9), 594.

Erickson, A. J., Gulliver, J. S., and Weiss, P. T. (2007). “Enhanced Sand Filtration for Storm Water Phosphorus Removal.” *Journal of Environmental Engineering*, 133(5), 485–497.

Ferguson, B. K. (2005). *Porous pavements*. Taylor & Francis.

Fletcher, T. D., Shuster, W., Hunt, W. F., Ashley, R., Butler, D., Arthur, S., Trowsdale, S., Barraud, S., Semadeni-Davies, A., Bertrand-Krajewski, J.-L., Mikkelsen, P. S., Rivard, G., Uhl, M., Dagenais, D., and Viklander, M. (2015). “SUDS, LID, BMPs, WSUD and more – The evolution and application of terminology surrounding urban drainage.” *Urban Water Journal*, 12(7), 525–542.

Ghafoori, N., and Dutta, S. (1995). “Building and Nonpavement Applications of No-Fines Concrete.” *Journal of Materials in Civil Engineering*, 7(4), 286–289.

Haselbach, L. M. (2010). “Potential for Clay Clogging of Pervious Concrete under Extreme Conditions.” *Journal of Hydrologic Engineering*, 15(1), 67–69.

Haselbach, L. M., and Freeman, R. M. (2006). “Vertical Porosity Distributions in Pervious Concrete Pavement.” ACI Materials Journal, 103(6), 452–458.

Haselbach, L. M., Valavala, S., and Montes, F. (2006). “Permeability predictions for sand-clogged Portland cement pervious concrete pavement systems.” *Journal of Environmental Management*, 81(1), 42–49.

Hatt, B. E., Fletcher, T. D., and Deletic, A. (2009). “Hydrologic and pollutant removal performance of stormwater biofiltration systems at the field scale.” *Journal of Hydrology*, 365(3–4), 310–321.

Hein, D. K., Strecker, E., Poresky, A., Roseen, R., and Venner, M. (2013). *Permeable Shoulders With Stone Reservoirs*. American Association of State Highway and Transportation Officials (AASHTO).

Hogland, W., and Niemczynowicz, J. (1986). “The unit Superstructure-A New Construction to prevent groundwater depletion.” *Conjunctive Water Use (Proceedings of the Budapest Symposium, July 1986*, 513–522.

Hounsfield, G. N. (1973). “Computerized transverse axial scanning (tomography): I. Description of system.” *British Journal of Radiology*.

Hsieh, C.-H., and Davis, A. P. (2005). “Evaluation and Optimization of Bioretention Media for Treatment of Urban Storm Water Runoff.” *Journal of Environmental Engineering*, 131(11), 1521–1531.

Hsieh, H. T., Brown, G. O., and Stone, M. L. (1998a). “Quantification of porous media using computerized tomography and a statistical segregation threshold.” *Transactions of the ASAE*, 41(6), 1697–1706.

Hsieh, H. T., Brown, G. O., Stone, M. L., and Lucero, D. A. (1998b). “Measurement of porous media component content and heterogeneity using gamma ray tomography.” *Water Resources Research*, 34(3), 365–372.

Hunt, W. F., Smith, J. T., Jadlocki, S. J., Hathaway, J. M., and Eubanks, P. R. (2008). "Pollutant Removal and Peak Flow Mitigation by a Bioretention Cell in Urban Charlotte, N.C." *Journal of Environmental Engineering*, 134(5), 403–408.

Iassonov, P., Gebrenegus, T., and Tuller, M. (2009). "Segmentation of X-ray computed tomography images of porous materials: A crucial step for characterization and quantitative analysis of pore structures." *Water Resources Research*, 45(9), 1–12.

Jarden, K. M., Jefferson, A. J., and Grieser, J. M. (2016). "Assessing the effects of catchment-scale urban green infrastructure retrofits on hydrograph characteristics." *Hydrological Processes*, 30(10), 1536–1550.

Jenkins, J. K. G., Wadzuk, B. M., and Welker, A. L. (2010). "Fines Accumulation and Distribution in a Storm-Water Rain Garden Nine Years Post Construction." *Journal of Irrigation and Drainage Engineering*, 136(12), 862–869.

Johannsen, G. and Bille, J. (1982). "A threshold selection method using information measures." in: 6th International Conference on Pattern Recognition, pp. 140–143.

Kandel, S., Vogel, J., Penn, C., and Brown, G. (2017). "Phosphorus Retention by Fly Ash Amended Filter Media in Aged Bioretention Cells." Water, Multidisciplinary Digital Publishing Institute, 9(10), 746.

Kapur, J. N., Sahoo, P. K., and Wong, A. K. C. (1985). "A new method for gray-level picture thresholding using the entropy of the histogram." *Computer Vision, Graphics, and Image Processing*, 29(3), 273–285.

Kayhanian, M., Anderson, D., Harvey, J. T., Jones, D., and Muhunthan, B. (2012). "Permeability measurement and scan imaging to assess clogging of pervious concrete pavements in parking lots." *Journal of Environmental Management*, Elsevier Ltd, 95(1), 114–123.

Ketcham, R. A., and Carlson, W. D. (2001). "Acquisition, optimization and interpretation of x-ray computed tomographic imagery: Applications to the geosciences." *Computers and Geosciences*, 27(4), 381–400.

Kia, A., Wong, H. S., and Cheeseman, C. R. (2017). "Clogging in permeable concrete: A review." *Journal of Environmental Management*, Elsevier Ltd, 193, 221–233.

Kittler, J., and Illingworth, J. (1986). "Minimum error thresholding.", *Pattern Recogn.* 19 (1) 41–47, http://dx.doi.org/10.1016/0031-3203(86)90030-0.

Kuang, X., Sansalone, J., Ying, G., and Ranieri, V. (2011). "Pore-structure models of hydraulic conductivity for permeable pavement." *Journal of Hydrology*, Elsevier B.V., 399(3–4), 148–157.

Kuang, X., Ying, G., Ranieri, V., and Sansalone, J. (2015). "Examination of Pervious Pavement Pore Parameters with X-Ray Tomography." *Journal of Environmental Engineering*, 141(10), 1–13.

Kumar, K., Kozak, J., Hundal, L., Cox, A., Zhang, H., and Granato, T. (2016). "In-situ infiltration performance of different permeable pavements in a employee used parking lot – A four-year study." *Journal of Environmental Management*, Elsevier Ltd, 167, 8–14.

Lewitt, R. M. (1983). "Reconstruction algorithms: Transform methods." *Proceedings of the IEEE*, 71(3), 390–408.

Li, L., and Davis, A. P. (2014). “Urban Stormwater Runoff Nitrogen Composition and Fate in Bioretention Systems.” *Environmental Science & Technology*, 48(6), 3403–3410.

Liu, J., Sample, D., Bell, C., and Guan, Y. (2014). “Review and Research Needs of Bioretention Used for the Treatment of Urban Stormwater.” *Water*, Multidisciplinary Digital Publishing Institute, 6(4), 1069–1099.

Lim, E., Fwa, T. F., and Tan, K. H. (2015). “Laboratory evaluation of clogging behavior of porous concrete pavements.” *Bituminous Mixtures and Pavements VI - Proceedings of the 6th International Conference on Bituminous Mixtures and Pavements, ICONFBMP 2015*, 1603–1612.

Lin, W., Park, D.-G., Ryu, S. W., Lee, B.-T., and Cho, Y.-H. (2016). “Development of permeability test method for porous concrete block pavement materials considering clogging.” *Construction and Building Materials*, Elsevier Ltd, 118, 20–26.

Lucas, W. C., and Greenway, M. (2011). “Phosphorus Retention by Bioretention Mesocosms Using Media Formulated for Phosphorus Sorption: Response to Accelerated Loads.” *Journal of Irrigation and Drainage Engineering*, 137(3), 144–153.

Manahiloh, K. N., Muhunthan, B., Kayhanian, M., and Gebremariam, S. Y. (2012). “X-Ray Computed Tomography and Nondestructive Evaluation of Clogging in Porous Concrete Field Samples.” *Journal of Materials in Civil Engineering*, 24(8), 1103–1109.

Meulenyzer, S., Stora, E., and Perez, F. (2012). “Impact of Pervious Concrete Porosity on Permeability by 3D Image Analysis.” *Pervious Concrete*, ASTM International, 100 Barr Harbor Drive, PO Box C700, West Conshohocken, PA 19428-2959, 1–25.

Neithalath, N., Weiss, J., and Olek, J. (2006). “Characterizing Enhanced Porosity Concrete using electrical impedance to predict acoustic and hydraulic performance.” Cement and Concrete Research, 36(11), 2074–2085.

Neithalath, N., Bentz, D., and Sumanasoorlya, M. (2010a). “Predicting the Permeability of Pervious Concrete: Advances in Characterization of Pore Structure and Transport Properties.” *Concrete International*, 32(5), 35–40.

Neithalath, N., Sumanasooriya, M. S., and Deo, O. (2010b). “Characterizing pore volume, sizes, and connectivity in pervious concretes for permeability prediction.” *Materials Characterization*, Elsevier Inc., 61(8), 802–813.

Nichols, P. W. B., White, R., and Lucke, T. (2015). “Do sediment type and test durations affect results of laboratory-based, accelerated testing studies of permeable pavement clogging?” *Science of The Total Environment*, Elsevier B.V., 511, 786–791.

Nichols, P., and Lucke, T. (2016). “Evaluation of the Long-Term Pollution Removal Performance of Established Bioretention Cells.” *International Journal of GEOMATE*, 11(24), 2363–2369.

Oklahoma Cooperative Extension Service (OCES). 2017. Bioretention Cell Design Guidance for Oklahoma. BAE-1536.

Otsu, N. (1979). “A Threshold Selection Method from Gray-Level Histograms.” *IEEE Transactions on Systems, Man and Cybernetics*, 9(1).

Passeport, E., Hunt, W. F., Line, D. E., Smith, R. A., and Brown, R. A. (2009). "Field Study of the Ability of Two Grassed Bioretention Cells to Reduce Storm-Water Runoff Pollution." *Journal of Irrigation and Drainage Engineering*, 135(4), 505–510.

Paul, M. J., and Meyer, J. L. (2001). "Streams in the Urban Landscape." *Annual Review of Ecology and Systematics*, 32(1), 333–365.

Paus, K. H., Morgan, J., Gulliver, J. S., and Hozalski, R. M. (2014). "Effects of Bioretention Media Compost Volume Fraction on Toxic Metals Removal, Hydraulic Conductivity, and Phosphorous Release." *Journal of Environmental Engineering*, 140(10), 4014033.

Permeable Pavements Task Committee. (2015). *Permeable pavements*. (B. Eisenberg, K. C. Lindow, and D. R. Smith, eds.), American Society of Civil Engineers.

Pitt, R., Field, R., Lalor, M., and Brown, M. (1995). "Urban Stormwater Toxic Pollutants: Assessment, Sources, and Treatability." Water Environment Research, 67(3), 260–275.

Radlińska, A., Welker, A., Greising, K., Campbell, B., and Littlewood, D. (2012). "Long-Term Field Performance of Pervious Concrete Pavement." *Advances in Civil Engineering*, 2012, 1–9.

Radon, J. (1986). "On the Determination of Functions from Their Integral Values along Certain Manifolds." *IEEE transactions on medical imaging*, 5(4), 170–176.

Randall, M. (2011). "Bioretention Gardens for the Removal of Nitrogen and Phosphorous from Urban Runoff." The University of Guelph.

Rehder, B., Banh, K., and Neithalath, N. (2014). “Fracture behavior of pervious concretes: The effects of pore structure and fibers.” *Engineering Fracture Mechanics*, Elsevier Ltd, 118, 1–16.

Sansalone, J., and Buchberger, S. G. (1997). “Partitioning and First Flush of Metals in Urban Roadway Storm Water.” *Journal of Environmental Engineering*, 123(2), 134–143.

Sansalone, J., Kuang, X., and Ranieri, V. (2008). “Permeable Pavement as a Hydraulic and Filtration Interface for Urban Drainage.” *Journal of Irrigation and Drainage Engineering*, 134(5), 666–674.

Sansalone, J., Kuang, X., Ying, G., and Ranieri, V. (2012). “Filtration and clogging of permeable pavement loaded by urban drainage.” *Water Research*, Elsevier Ltd, 46(20), 6763–6774.

Schaefer, V., Wang, K., Suleiman, M., and Kevern, J. (2006). *Mix design development for pervious concrete in cold weather climates*. Center for Transportation Research and Education, Iowa State University.

Sumanasooriya, M. S., Bentz, D. P., and Neithalath, N. (2010). “Planar image-based reconstruction of pervious concrete pore structure and permeability prediction.” *ACI Materials Journal*, 107(4), 413–421.

Sumanasooriya, M. S., and Neithalath, N. (2009). “Stereology- and morphology-based pore structure descriptors of enhanced porosity (Pervious) concretes.” *ACI Materials Journal*, 106(5), 429–438.

Suozzo, M., and Dewoolkar, M. (2012). “Long-Term Field Monitoring and Evaluation of Maintenance Practices for Pervious Concrete Pavement in Vermont.” *Transportation Research Record: Journal of the Transportation Research Board*, 2292(2292), 94–103.

Taniguchi, K., Yamane, H., Sasaki, K., Agatsuma, Y., and Arakawa, H. (2001). “Marine afforestation of the kelp Eisenia bicyclis in coralline flats by introduction of porous-concrete reefs.” *Bulletin of the Japanese Society of Scientific Fissheries (Japan)*.

Teng, Z., and Sansalone, J. (2004). “In situ partial exfiltration of rainfall runoff. II: Particle separation.” *Journal of Environmental Engineering-Asce*, 130(9), 1008–1020.

Tennis, P. D., Leming, M. L., and Akers, D. J. (2004). *Pervious Concrete Pavements*. *EB302.02,* Portland Cement Association, Skokie, Illinois, and National Ready Mixed Concrete Association, Silver Spring, Maryland, USA.

Tuller, M., Kulkarni, R., Fink, W., Anderson, S. H., and Hopmans, J. W. (2013). “Segmentation of X-Ray CT Data of Porous Materials: A Review of Global and Locally Adaptive Algorithms.”

United Nations Department of Economic and Social Affairs (UN DESA). (2014). World’s population increasingly urban with more than half living in urban areas. (2014, July 10). Retrieved April 18, 2016, from http://www.un.org/en/development/desa/news/population/world-urbanization-prospects-2014.html

U.S. Census Bureau. (2010). 2010 Census Urban and Rural Classification and Urban Area Criteria. Retrieved April 18, 2016, from https://www.census.gov/geo/reference/ua/urban-rural-2010.html

U.S. Environmental Protection Agency (USEPA). (1997). *Urbanization and Streams: Studies of Hydrologic Impacts*. Washington, D.C.

U.S. Environmental Protection Agency (USEPA). (2017). "National Summary of State Information, Water Quality Assessment and TMDL Information." <https://ofmpub.epa.gov/waters10/attains_nation_cy.control> (Sep. 7, 2017).

Udawatta, R. P., Anderson, S. H., Gantzer, C. J., Assouline, S., Anderson, S. H., and Hopmans, J. W. (2013). "Computed Tomographic Evaluation of Earth Materials with Varying Resolutions."

Viessman, W., and Lewis, G. L. (2003). *Introduction to hydrology*. 5th edition. Prentice Hall.

Vogel, J. R., and Brown, G. O. (2003). "Geostatistics and the representative elementary volume of gamma ray tomography attenuation in rock cores." *Geological Society, London, Special Publications*, Geological Society of London, 215(1), 81–93.

Vogel, J. R., Moore, T. L., Coffman, R. R., Rodie, S. N., Hutchinson, S. L., McDonough, K. R., McLemore, A. J., and McMaine, J. T. (2015). "Critical Review of Technical Questions Facing Low Impact Development and Green Infrastructure: A Perspective from the Great Plains." *Water Environment Research*, 87(9), 849–862.

Vogel, J. R., and Moore, T. L. (2016). "Urban Stormwater Characterization, Control, and Treatment." *Water Environment Research*, 88(10), 1918–1950.

Wadzuk, B. M., Hickman, J. M., and Traver, R. G. (2015). "Understanding the Role of Evapotranspiration in Bioretention: Mesocosm Study." *Journal of Sustainable Water in the Built Environment*, 1(2), 4014002.

Walsh, C. J., Roy, A. H., Feminella, J. W., Cottingham, P. D., Groffman, P. M., and Morgan, R. P. (2005). “The urban stream syndrome: current knowledge and the search for a cure.” *Journal of the North American Benthological Society*, 24(3), 706–723.

Welker, A. L., Jenkins, J. K. G., McCarthy, L., and Nemirovsky, E. (2013). “Examination of the Material Found in the Pore Spaces of Two Permeable Pavements.” *Journal of Irrigation and Drainage Engineering*, 139(4), 278–284.

Winston, R. J., Al-Rubaei, A. M., Blecken, G. T., Viklander, M., and Hunt, W. F. (2016a). “Maintenance measures for preservation and recovery of permeable pavement surface infiltration rate – The effects of street sweeping, vacuum cleaning, high pressure washing, and milling.” *Journal of Environmental Management*, Elsevier Ltd, 169, 132–144.

Winston, R. J., Davidson-Bennett, K. M., Buccier, K. M., and Hunt, W. F. (2016b). “Seasonal Variability in Stormwater Quality Treatment of Permeable Pavements Situated Over Heavy Clay and in a Cold Climate.” *Water, Air, & Soil Pollution*, Water, Air, & Soil Pollution, 227(5), 140.

Yong, C. F., Deletic, A., Fletcher, T. D., and Grace, M. R. (2008). “The clogging behaviour and treatment efficiency of a range of porous pavements.” *11th International Conference on Urban Drainage*, 1–12.

Yong, C. F., McCarthy, D. T., and Deletic, A. (2013). “Predicting physical clogging of porous and permeable pavements.” *Journal of Hydrology*, 481, 48–55.

Youngblood, S., Vogel, J., Brown, G., Storm, D., McLemore, A., and Kandel, S. (2017). “Field Studies of Microbial Removal from Stormwater by Bioretention Cells with Fly-Ash Amendment.” *Water*, Multidisciplinary Digital Publishing Institute, 9(7), 526.

Zhang, R., Jiang, G., and Liang, J. (2015). “The Albedo of Pervious Cement Concrete Linearly Decreases with Porosity.” *Advances in Materials Science and Engineering*, Hindawi Publishing Corporation, 2015, 1–5.

Zhang, W., Brown, G. O., Storm, D. E., and Zhang, H. (2008). “Fly-Ash-Amended Sand as Filter Media in Bioretention Cells to Improve Phosphorus Removal.” *Water Environment Research*, 80(6), 507–516.

CHAPTER III

HYDRAULIC ANALYSIS AND POLLUTANT LEACHING POTENTIAL OF TWO ESTABLISHED BIORETENTION CELLS AMENDED WITH FLY-ASH

This chapter will be submitted the Journal of Environmental Engineering, an American Society of Civil Engineers journal.

ABSTRACT

In this study, established bioretention cells that are amended with fly ash are subjected to controlled flooding tests to quantify hydraulics, leaching potential, and how performance compares to post construction flooding tests and common design standards. Low impact development practices can improve urban stormwater water runoff, but long-term performance is not well documented. Two 8-year-old bioretention cells treated on average 23.8 mm of runoff prior to overflow, which is close to the design storage capacity of 25.4 mm. From the inlet to the underdrain, steady-state flow rates were reduced by 90% on average. Measured drawdown rates at steady-state flow were 86.5 mm/hr and 28.5 mm/hr. Electrical conductivity, chloride, nitrate, pH, and turbidity had significantly lower levels from the inlet to the underdrain even though the bioretention cells were flushed with treated municipal water. Measured at the underdrain, *E. coli*,

enterococci, electrical conductivity, nitrate, pH, and turbidity all had lower levels during the latter of two back-to-back flooding tests. Both studied bioretention cells had drawdown times less than 48 hours. The results of this study are applicable to future BRC designs and stormwater management planning.

INTRODUCTION

Long-term performance of aged low impact development stormwater infrastructure is not well understood. Bioretention cells (BRCs) have been used in practices for over two decades (PGCo 2001). Knowing the performance of aged BRCs is essential to the development of long-term stormwater management goals; principally, offsetting the negative alterations urbanization has on stormwater runoff. Increased flow rates and surface runoff volumes caused by urbanization can create flooding and erosion of downstream waterways (Paul and Meyer 2001). Pollutants produced by urban activities collect on impervious surfaces. These pollutants can be transported by stormwater to nearby ecosystem, where they can negatively alter the ecosystems (Paul and Meyer 2001). A BRC is an infiltration based LID practice that can mitigate the negative effects of urban stormwater runoff with physical, chemical, and biological processes. Maintaining storage and drawdown rate of the BRC surface is critical for long-term success. Research investigating the long-term performance of BRCs is needed (Ahiablame et al. 2012; Emerson and Traver 2008; Vogel et al. 2015)

For over two decades BRC have been used in practice (PGCo 2001). BRCs are shallow depressions in the landscape where stormwater runoff collects. The main components of BRCs include an inlet, ponding area, filter media, overflow, and often a drainpipe (known as an underdrain) at the bottom of filter media. In general, BRCs are sized to store and treat runoff produced by small to medium sized precipitation events on relative small (lot to neighborhood) catchment areas (Vogel et al. 2015). Design specifications for the volume of runoff to be treated

by BRCs ranges from 12.7 to 30.5 mm (0.5 to 1.2 in.), and is commonly the first 25.4 mm (1.0 in.) of runoff from the contributing area (Vogel et al. 2015). Stormwater storage capacity of a BRC includes the ponded surface and voids in the soil media. The ponded surface is for short-term storage and is typically designed to drain in 24 to 48 hours. BRC filter media varies, but the main component is usually a low-fines, sandy soil. The sandy soil provides storage and filtration, and is the medium in which biological and chemical sorption can occur. Infiltration capacity at the surface and percolation through soil media are key attributes for the long-term application and reliability of BRCs as a stormwater control measure.

BRCs has been well documented for their ability to restore the runoff hydrograph from urban landscapes to a more natural condition (Dietz 2007; DeBusk and Wynn 2011; Ahiablame et al. 2012; Davis et al. 2012). This includes reduction of runoff volumes by up to 100% for smaller storms (Davis et al. 2012; DeBusk and Wynn 2011; Youngblood et al. 2017). Peak flow reductions have been reported between 49% and 99%, and lag times and time to peak discharge can be increased (Davis 2008; DeBusk and Wynn 2011; Jarden et al. 2016; Winston et al. 2016). Davis (2008) found that peak discharge was delayed by more than six times the inlet time to peak discharge for 36% of monitored storms.

BRCs have also been shown to improve stormwater quality. Reports of nitrogen reduction indicated variability with greater reduction for total nitrogen than nitrate (Chen et al. 2013; Davis et al. 2006; Hsieh and Davis 2005). In some cases, nitrate is exported (Li and Davis 2014). The use of a saturated zone created by an upturned elbow can improve nitrate reduction compared to traditional bottom underdrain BRCs (Brown and Hunt 2011; Passeport et al. 2009). Phosphorus reduction has been reported by many (Dietz 2007; Hsieh and Davis 2005; Hunt et al. 2008; Randall 2011; Zhang et al. 2008). Though, phosphorus leaching has also been observed (Dietz and Clausen 2006; Hatt et al. 2009; Paus et al. 2014). Bacteria removal rates have been reported

and range from 64% to 97% (Ahiablame et al. 2012; Youngblood et al. 2017). BRCs are efficient at filtering total suspended solids (TSS) from stormwater (Dietz 2007; Hsieh and Davis 2005; Hunt et al. 2008, 2012; Kandel et al. 2017). TSS removal over 90% is not uncommon (Dietz 2007; Hsieh and Davis 2005). Chloride movement through BRCs is not well documented and concentrations are considerably impacted by winter salting (Dietz 2007).

Pollution retention can be increased with the use of amendments in the filter media (Zhang et al. 2008, Kandel et al. 2017). Zhang et al. (2008) demonstrated through laboratory studies that fly ash at 5% by weight mixed with sand improved phosphorus retention. Later, Kandel et al. (2017) determined that 7-year-old BRCs that were amended with 5% fly ash weight still had available sorption sites based on laboratory analysis of aged filter media and stormwater monitoring. Electrical conductivity and pH can be influenced by filter media amendments (Reddy et al. 2014). With laboratory batch experiments, Reddy et al. (2014) showed that calcite, zeolite, sand, and iron filing increased pH but decreased EC. The impact fly ash has on the filter media infiltration rate and storage capacity is not well documented.

Stormwater benefits from BRCs rely heavily on infiltration into the filter media. The infiltration rate into the filter media at steady-state is the drawdown rate and is a good measure of performance. The drawdown rate of BRC filter media can be evaluated by monitoring stormwater events, conducting spot infiltration tests, and/or artificially flooding the ponded area (Emerson and Traver 2008; Jenkins et al. 2010; Komlos and Traver 2012; Johnson and Hunt 2016; Nichols and Lucke 2016). It can be useful to know how drawdown rate changes with time to estimate the life expectancy and maintenance needs of a BRC. Individual infiltration rates measurements with a ring infiltrometer can be used to evaluate drawdown rate. Jenkins et al. (2010) measured the drawdown rate of a BRC over a three-year period with a ring infiltrometer. They found that infiltration rate had not significantly changed over three years, though measurements varied

significantly at separate locations in the BRC within the same year. Variability within the BRC can be avoided by flooding the entire ponded area.

Two types of flooding methods have been used on BRCs; mimicking storm events and steady-state flood testing. Anderson (2012) evaluated how well established residential BRCs meet local standards with a storm runoff simulator. The local design storm was 30.2 mm SCS-Type II 30-min event. The use of controlled flooding allowed this test to be conducted on 12 difference BRCs over a shorten time span. Their design storm would be expected to naturally occur about once per year. Nichols and Lucke (2016) successfully flooded small 10-year old BRCs with synthetic stormwater to measure pollution reduction of synthetic stormwater and infiltration rate. In the Nichols and Lucke (2016) flooding study, total suspended solids and total nitrogen increased while total phosphorus decreased when the synthetic stormwater had no pollutants added to it. Concentrations were reduced from inlet to underdrain when the synthetic stormwater was spiked with pollutants.

Fire hydrants as the water source, which are common in urban setting where BRCs are often placed, can be used for controlled flooding tests. Flood tests have been shown to be a useful way to quantify BRC hydraulics (Asleson et al. 2009; Christianson et al. 2012; Minnesota Stormwater Manual 2017). Asleson et al. (2009) compared the drawdown rate from flood testing to ring infiltrometer test. Two of the three BRCs had comparable results while the third BRC had its infiltration rate over estimated by the ring infiltrometer method. Christianson et al. (2012) used steady-state flood testing one year after installation on BRC amended with fly ash. While the primary focus of Christianson et al. (2012) was to calibrate and validate a model, steady-state flow rate, volume, and timing parameters can be determined from the reported results. Three flooding tests were completed by Christianson et al (2012): (1) Grove High School (GHS)-dry, GHS-wet, and Grand Lake Association (GLA)-dry. Parameters describing the flooding

experiments are shown in Table 3.1. Overall, validation of flood testing methods are limited, and the evaluation of aged BRCs that have measured benchmark data from controlled flood tests is not present in the literature.

Table 3.1. Results from Christianson et al. (2012) bioretention cell flooding test at Grove High School (GHS) and Grand Lake Association (GLA).

	GHS-dry	GHS-wet	GLA-dry
Steady-state flow rate (L/s)			
Inflow *	9.9	9.2	15.1
Overflow	6.5	5.3	9.0
Underdrain	1.2	1.2	2.6
Volume (m^3)			
Inflow	217.5	108.0	384.3
Overflow	69.8	19.0	128.0
Underdrain	49.4	37.6	150.0
Flow start time (minutes)			
Underdrain	48	32	14
Overflow	120	117	149
Steady-state start time (minutes)			
Inflow	0*	0*	0*
Overflow	270	174	149
Underdrain	270	174	352
End of flow time (hr)			
Inflow	6.1	3.3	7.1
Overflow	21.3	18.2	48.0
Underdrain	6.8	3.7	7.73

*Inflow was measured at fire hydrant.

The objectives of this are to (1) quantify hydraulics and leaching potential of two 8-year old BRCs amended with fly ash, (2) compare current hydraulic performance to the flood tests results of Christianson et al. (2012) completed seven years prior, and (3) determine if the BRCs are meeting design specifications and common BRC design standards.

MATERIAL AND METHODS

Study site description

Two BRCs located in Grove, Oklahoma and constructed in 2007 were evaluated in this study (Figure 3.1). The filter media of the BRCs were designed to be identical and is a mixture of Dougherty Sand and 5% fly ash (Chavez et al. 2015). Both cells were constructed with sand plugs to reduce long-term clogging potential. The sand plugs, which were constructed with Dougherty Sand, span from the surface through growth media to the filter media and occupy approximately 25% of surface area. A 0.3 m thick layer of local top soil was installed around the sand plugs as a growth media for vegetation. The two BRCs in this study are the same ones Christianson et al. (2012) studied; Grove High School (GHS) and Grand Lake Association (GLA).

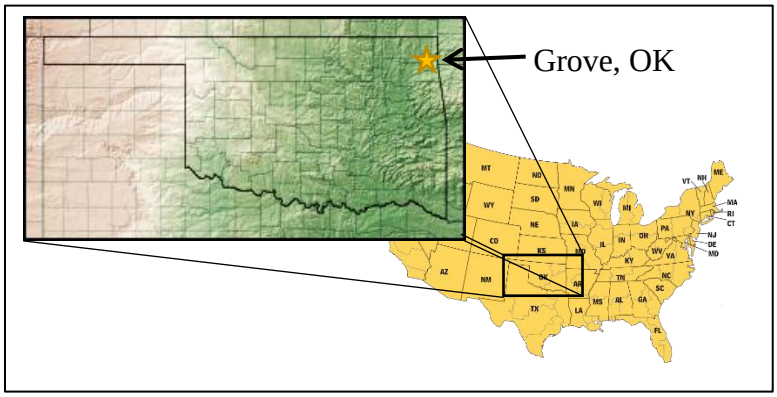

Figure 3.1. Map showing the location of Grove, Oklahoma, which is the where the bioretention cells are located (OKtag 2007; U.S. Government 2016).

The GHS BRC has 149 m^2 of surface area and 2600 m^2 of contributing area, which is an asphalt parking lot. GLA has a cell surface area of 320 m^2 and a contributing area of 4000 m^2. The contributing area to GLA is mostly asphalt pavement with a mix of turf and gravel in-between the BRC inlet and asphalt pavement. GHS ponding depth is 0.20 m and GLA ponding depth is 0.17 m. Both cells were sized to store 13 mm of runoff in filter media and an additional 13 mm on the surface before the cells would overflow. The 90th percentile precipitation event in Grove,

Oklahoma is 27.9 mm, which produces 22.6 mm of runoff when modeled with a 98 curve number. Chavez et al. (2015) provides detailed description of the design and construction of the GHS and GLA BRCs.

Flood testing

To determine the hydraulics of the two BRCs in the study, each was flooded at a constant flow rate. The flooding test methods used in this study were similar but not identical to the methods used by Christianson et al. (2012). Water from a fire hydrant was piped near the inlet of the BRCs with firehose. The fire hydrant was opened to produce a constant flow rate. A Hose Monster was fitted to the end of the hose for stability (Hose Monster Company, Lake Zurich, IL). Water was discharged onto an impermeable surface and allowed to flow overland to the inlet of the BRC. There was approximately 3 m of shallow concentrated flow through grass at GHS before reaching the BRC inlet and 21 m of shallow concentrated flow over grass and gravel at Grand Lake Association before reaching the BRC inlet. A constant flow rate was maintained at the inlet until the underdrain and overflow reach a constant flow rate.

Two flood tests were completed on the GHS BRC. The first flood test was to assess the cell's performance when the media was in a dry condition. The dry condition test was completed in November of 2015. The most recent precipitation event was 5 days prior and was 7.87 mm. Three grab samples of the filter media were collected to assess soil moisture content; one from the near the inlet, one in the middle, and one near the overflow. All samples were collected from the filter media immediately below the growth media. Sampling volume was 87 cm^3. The second flood test was completed a day after the dry condition tests to evaluate the hydraulics when the cell media is at a wet condition. The cell was allowed to drain prior to completing the wet condition test. Grab samples to measure soil moisture were collected prior to starting the wet condition test near the

same locations as the dry condition samples. Only a dry condition test was completed on the GLA BRC. This sequence of tests aligns with those completed by Christianson et al. (2012).

Flow rate at the inlet, underdrain, and overflow at GHS was measured every minute with an ISCO 720 submerged flow pressure module and logged by an ISCO 6712 automatic sampler. Inlet flow was measured with a 0.31 m H-flume, underdrain flow was measured with a 0.076-m Palmer-Bowlus flume, and overflow was measured with a 0.762-m sharp crested rectangular weir. At GLA, inlet flow was measured with a 0.31-m H-flume, underdrain flow was measured with a 0.102-m Palmer-Bowlus flume, and overflow was measured with a 1.05-m sharp-crested rectangular weir. Water samples were collected by the ISCO 6712 automatic samplers at set time intervals at the inlet and underdrain. Overflow samples were collected by hand at set time intervals. The samples were analyzed for electrical conductivity (EC), chloride, nitrate, orthophosphate, pH, turbidity, total coliform, *E. Coli*, and enterococci. EC was determined using Method 2510 B from Standard Methods for the Examination of Water and Wastewater (2005). Chloride was determined using a Lachat instrument and chloride analysis method from U.S. EPA (1979). Lachat method 12-107-04-1-B was used for nitrate analysis, and Lachat method 10-115-01-1-A was used for orthophosphate analysis. A Hach 2100Q benchtop turbidity meter will be used to measure turbidity (Hach Company, Loveland, CO). Total coliform and *E. coli* was analyzed using Standard Methods 9223B and enterococci was analyzed using ASTM D6503–14 (Standard Method 2005; ASTM 2014).

Flooding tests were conducted with a steady inflow rate and stopped once the overflow and underdrain reached a steady-state flow rate. Flow rates were assumed steady-state when the level remained within 0.5 cm for at least a 10-minute period. The median value within the steady-state period was taken as the steady-state flow rate. Exfiltration is the movement of water out of a BRC

through the surrounding native soil. Steady-state flow rates were used to estimate exfiltration rates. Exfiltration rate is calculated as

$$Q_E = Q_I - (Q_O + Q_{UD}) \tag{3.1}$$

where Q is flow rate and subscripts E, I, O, and UD represent exfiltration, inlet, overflow, and underdrain, respectively.

Bioretention cell surface drawdown

Filtering and storage within the media of a BRC requires adequate infiltration rate to meet stormwater management needs. As BRCs age, the surface may clog and result in decreased drawdown rate and an increased drawdown time. Drawdown rate of the filter media is calculated as

$$I = \frac{Q}{A_{cell}} \tag{3.2}$$

where I is the drawdown (infiltration) rate, Q is a flow rate and A_{cell} is the BRC surface area. Time to drain the surface of a BRC is known as the drawdown time. Often, the goal in BRC design to denote a maximum drawdown time to ensure adequate storage space for successive storm events and to prevent stagnant water issues such as mosquitoes. Drawdown time is calculated as

$$t_{DD} = \frac{d_{BRC}}{I} \tag{3.3}$$

where t_{dd} is the drawdown time and d_{BRC} is the surface ponding depth.

Equivalent curve number

The NRCS curve number (CN) model can be used to estimate runoff depths produced by a depth of rainfall on a known surface cover, hydrologic soil type, and antecedent runoff condition (NRCS 1986). Runoff depth (Q_{CN}) is calculated as

$$Q_{CN} = \frac{(P - 0.2\,S)^2}{(P + 0.8\,S)} \tag{3.4}$$

where *P* is the rainfall depth and *S* the potential maximum retention after runoff begins; all variables have unites of inches. *S* is determined with the CN as

$$S = \frac{1000}{CN} - 10 \tag{3.5}$$

where the CN is an empirical variable that has a value between 0 and 100. Common CN values are listed in NRCS (1986). An equivalent CN produced by the volume reduction of a BRC can be back calculated with Eqs. 3.4 and 3.5 to estimate the equivalent hydrologic condition a BRC on the contributing catchment. Depth variables, *P* and Q_{CN}, are calculated as

$$P = \frac{V_{In}}{A_{CA}} \tag{3.6}$$

and

$$Q = \frac{V_{Out}}{A_{CA}} \tag{3.7}$$

where V_{In} is the inlet volume of the BRC, V_{Out} is the total outflow volume of the BRC, and A_{CA} is the area of the catchment.

Statistical methods

Performance of the BRCs for leaching of water-quality constituents were tested for differences using non-parametric analyses. Anderson-Darling tests for normality was completed to determine if non-parametric statistics were appropriate; data were defined as non-parametric when the alpha value was less than 0.05. Differences between inlet, overflow, and underdrain water-quality constituents were determined with a Kruskal-Wallis tests and pairwise comparison analysis. Difference between underdrain water-quality parameters for the dry and wet experiments were

determined with Wilcoxon rank-sum tests at a 95% confidence level. Statistical tests were completed with MATLAB (The MathWorks Inc 2016).

RESULTS AND DISCUSSION

Water quantity

Steady-state flow rates

BRCs are often installed to mitigate peak flow rates from impervious surfaces. In this study, steady-state peak flow rates were reduced. Average flow rate during periods of steady-state flow are compared. Table 3.2 shows steady-state flow rates, volumes, and timing based parameter results for 1-year and 8-year after installation. One-year after values are from Christianson et al. (2012). GHS-dry and -wet flood tests hydrographs for the inlet, overflow, and underdrain of the 8-years after installation are shown in Figures 3.2. Hydrographs for GLA-dry flood test completed for this study, showing the inlet, overflow, underdrain, and total outflow, are shown in Figure 3.3. Antecedent dry period of GHS-dry was 5 days, where the antecedent dry period is defined as the number of day prior with less than 0.1 inches of precipitation. GHS-wet was completed approximately 24 hrs after GHS-dry, antecedent dry period of 0 days. GLA-dry antecedent dry period was 8 days.

Underdrain steady-state flow rates were much less than inlet steady-state flow rates. GHS-dry underdrain was 0.57 L/s, a 95% reduction. GHS-wet was 0.55 L/s, also a 95% reduction. GLA-dry underdrain was 2.2 L/s, an 81% reduction. Lower percent reduction during GLA-dry is attributed to surface area and potential seepage of groundwater upslope of the BRC. GLA has 2.1 times the surface area as GHS, thus has potentially 2.1 times as much infiltration capacity. GLA is located at the bottom of hill near Grand Lake, and the long overland flow path between the firehose outlet and the inlet of GLA may be a source of groundwater seepage. Some flow likely

infiltrated and became groundwater before reaching the inlet. Nevertheless, an 81% reduction in peak flows rate is substantial.

Table 3.2. Flooding test results: steady-state flow rate, volume, flow start time, steady-state start time, and end of flow time for Grove High School (GHS) dry and wet flooding tests and Grand Lake Association (GLA) dry flooding test. Results from Christianson et al. (2012) (1-year after construction) and this study are included (8-years after construction).

	GHS-dry		GHS-wet		GLA-dry	
	1-year	8-year	1-year	8-year	1-year	8-year
Steady-state flow rate (L/s)						
Inflow *	9.9	11.80	9.2	11.60	15.1	11.40
Overflow	6.5	8.27	5.3	8.27	9.0	8.87
Underdrain	1.2	0.57	1.2	0.55	2.6	2.20
Volume (m^3)						
Inflow	217.5	106.0	108.0	108.0	384.3	126.3
Overflow	69.8	34.5	19.0	43.9	128.0	37.8
Underdrain	49.4	14.7	37.6	14.8	150.0	125
Flow start time (minutes)						
Underdrain	48	12	32	4	14	12
Overflow	120	86	117	64	149	87
Steady-state start time (minutes)						
Inflow	0*	17	0*	14	0*	130
Overflow	270	94	174	62	149	152
Underdrain	270	126	174	108	352	167
End of flow time (hr)						
Inflow	6.1	2.9	3.3	3.0	7.1	4.9
Overflow	21.3	16.8	18.2	18.6	48.0	73.0
Underdrain	6.8	3.0	3.7	3.1	7.73	4.2

*Inflow was measured at fire hydrant and not the entrance of the BRC.

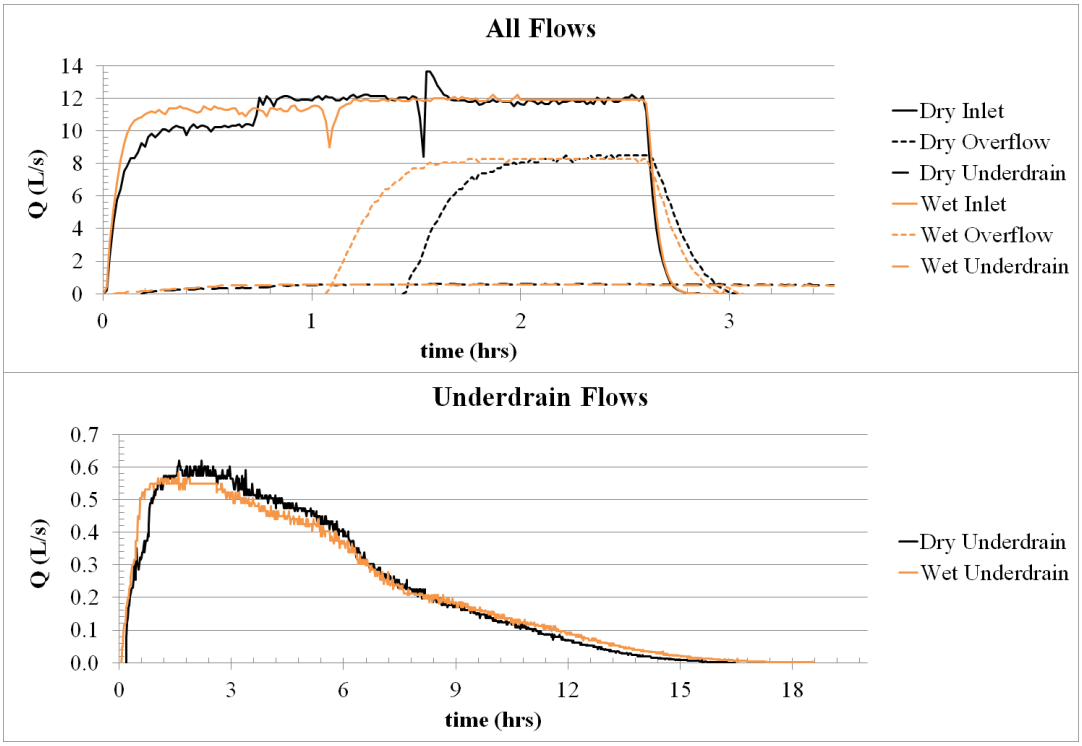

Figure 3.2. Hydrographs for Grove High School (GHS) flood experiments.

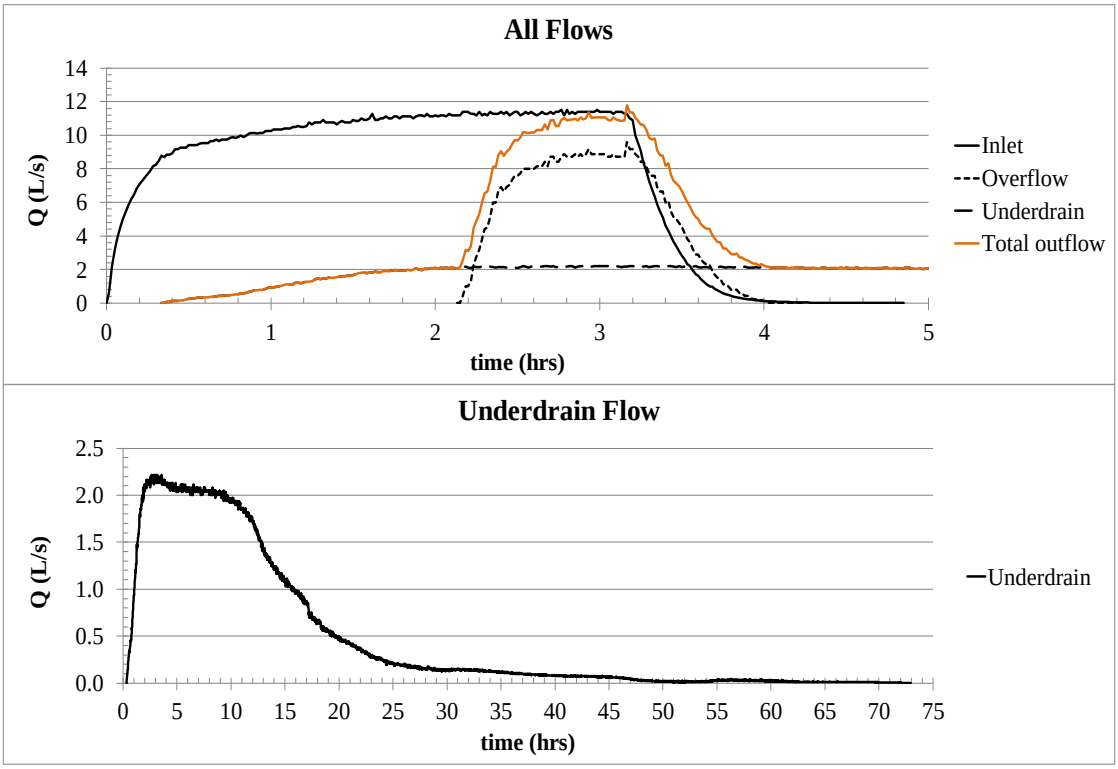

Figure 3.3. Hydrographs for the Grand Lake Association (GLA) flood experiment.

Steady-state overflow rates and the total steady-state outflow rates (overflow and underdrain combined) were more than four times greater than steady-state underdrain flow rates for all flooding tests. Once the storage space in the BRCs filled, overflow rate increased rapidly. The increase is visible in Figures 3.2 and 3.3. There is a 25% reduction between the inlet steady-state flow rate and total steady-state outflow rate for GHS-dry and a 26% reduction for GHS-wet. The GLS-dry inlet steady-state flow rate reduction was only 2.9% once the underdrain and overflow reached steady-state. The 0.3 L/s that was not measured is assumed to be exfiltration. A low estimation for the exfiltration rate may be contributed to a shallow groundwater table as previously mentioned. GHS, however, did have an estimated exfiltration rate of 3.0 L/s and 3.1 L/s for GHS-dry and GHS-wet, respectively. These flow rates are higher than the underdrain steady-state flow rate indicating that water flowing into the media is more likely to become groundwater than underdrain discharge at the studied inlet steady-state flow rate.

A critical question regarding the performance of aged BRCs is what changes occur to the underdrain and exfiltration flow rates. For GHS, the underdrain steady-state flow rate was on average 13% of the inlet for the 1-year after flooding tests while it was on average 4.8% of the inlet for the 8-years after flooding tests. Percentage of the underdrain steady-state flow rate during GLA-dry tests increased by 2% from 17% from 1-year to 8-years after construction. These percentages are influenced by the differences between the inlet steady-state flow rates. Comparing the steady-state flow rates from the underdrain is a better indicator of performance since the underdrains experienced similar hydraulic heads between both tests. The difference between the underdrain steady-state flow rates decreased for all tests on both BRCs. A decrease of 0.63 L/s for GHS-dry, 0.65 L/s for GHS-wet, and 0.4 L/s for GLA-dry. It appears, based on the underdrains, that the filter media at GHS is clogging as the BRCs aged. However, comparison of the exfiltration rates suggests that GHS is not clogged, but is more hydraulically connected to the surrounding soil. The exfiltration rate increased by 0.76 L/s for GHS-dry and 0.38 L/s for GHS-

wet. GLA-dry exfiltration decreased by 3.17 L/s. This reduction may be caused by clogging and compaction of the filter media. Though, at least a partition of the decrease could be attributed to the seepage that occurred before the inlet of GLA-dry during the 8-year after test. Additionally, the inlet flow rate during the 1-year after test was measured at the fire hydrant. If seepage had occurred, it would have not been excluded from the inlet and would be in exfiltration estimate and underdrain flow.

Volume

Impervious surfaces typically increase the volume of stormwater runoff; this can be mitigated with BRCs. A volume balance analysis was completed on the GHS-dry, GHS-wet, and GLA-dry experiments. Volumes were calculated from the hydrographs shown in Figure 3.2 and 3.3 and are listed in Table 3.2. GLA-dry is mostly excluded from the volume analysis discussion because the measured total outflow volume was greater than the inflow volume. GLA-dry 8-year after exported 36.5 m^3. Exporting water from GLA-dry further suggests that seepage from up slope of the inlet contributed to underdrain flow and exfiltration.

Runoff that entered the BRCs is this study became surface storage first. After which, the runoff water either exited the cell as overflow or entered the filter media. A portion could have evaporated from the surface. Flooding tests at GHS were completed in November and the average max air temperature was 17.6^{o}C for the 2 days during the tests. The evapotranspiration during this period is on the order of a 0.5 cm or 0.75 m^3 from GHS. This volume is negligible compare to the total inflow volume of 214 m^3 for GHS-dry and -wet combined. 34.5 m^3 (33%) of the inflow volume exited the cell as overflow for GHS-dry. The remainder entered the filter media with 14.7 m^3 (14%) coming out of the underdrain. The remaining 56.8 m^3 (53%) of the inflow water was retained by the BRC. The retained water was stored in the filter media, exfiltrated to the surrounding native soil, or became evapotranspiration. GHS-wet inflow volume was 108 m^3 and

43.9 m^3 (41%) became overflow. Underdrain volume was 14.8 m^3 (14%) and 49.3 m^3 (45%) was retained. The dry test performed better on volume retention bases than the wet flooding test; being dry increased the retention by 5.4 m^3 (8%). Differences can be attributed to the time to reach a steady-state drawdown rate into the media, which influenced the overflow beginning time. More water was stored in the soil because the moisture content was lower at the start of the dry test compared to the wet test. Filter media moisture content was 11% by weight before starting GHS-dry and 15% by volume before starting GHS-wet. The difference accounts for approximately 1.6 m^3 of pore space in the filter media. The surrounding native soil is assumed to have had similar difference in moisture content. A portion of the extra retention was in the filter media, but ultimately some of the retention was in the surrounding soil.

Retention and filtration performance between the 1-year after and the 8-year after flooding tests are compared by analyzing volumes normalized to the inlet volume of their respective test. For GHS-dry, the underdrain volume decreased from 23% to 14% from the 1-year tests to the 8-year tests. The decrease was greater for GHS-wet; from 35% to 14%. The decreases were caused in part by a decrease in the underdrain steady-state flow rates and an increase in the inlet steady-state flow rates. A decrease as the BRC aged can have negative and positive effects. It lowered the overall percentage of the inflow that was filtered, but increased the percentage that became exfiltration. The 1-year after exfiltration volume percentages were 68% for GHS-dry and 48% for GHS-wet. The 8-year after exfiltrations are similar at 67% and 46% for GHS-dry and -wet, respectively. These results further suggest the hydraulic connectivity of the filter media with the native soil increased as the BRC aged.

Hydrograph timing

An important parameter when trying to mimic natural hydrology with LID practices is the timing of the runoff hydrograph. Urbanized areas tend to shorten the time to the beginning of direct

runoff, time to the end of direct runoff, and time to peak. In this study, inlet flow rates increased quickly and reached steady state in 17 minutes for GHS-dry and 14 minutes for GHS-wet. Within 12 minutes after the inlet started, the underdrain began to flow for GHS-dry, and GHS-wet underdrain began to flow in 4 minutes. Underdrain flow began 8 minutes sooner when the filter media was wet, compared to when the media was dry. The corresponds to an extra 3.37 m^3 of runoff being stored before underdrain flow started for GHS-dry. This is equivalent to approximately 9% of the BRC media total porosity and 30% of the water holding capacity of filter media, based on a loamy fine sand soil texture.

The inlet flow for GLA-dry test increased less rapidly than the inlet flow for the GHS flooding tests, though the underdrain started to flow at a similar time, 12 minutes after inlet flow began. GLA-dry inlet reached steady-state discharge 130 minutes after the test began. There was an apparent short-circuiting of water to the underdrain near the inlet as indicated by the short times for underdrain flow to begin. The storage volume exists in the BRC, but an almost immediate discharge from the underdrain is occurring because of the underdrain design and infiltration rate. The underdrains of the BRCs in the study have multiple literately drainage pipes. These drainage pipes expanse covers the entire bottom of the BRC, thus allowing from almost anywhere along the bottom of the BRC. Short circuiting could be alleviated with an upturned elbow and sufficient exfiltration into the native soil between storm events. This would work best during the dry season when the antecedent dry period is longer. Decreasing the BRC infiltration rate could also reduce short-circuiting. An alternatively underdrain design that could decrease short-circuiting would be to position the underdrain as far away from the inlet as possible. This would require specific design changes such as sloping the bottom of the BRC towards the underdrain. While design changes may prevent the short circuiting, the near immediate flow at the underdrain is not necessarily a negative result. Given the relatively small underdrain flow rates, the initial flow might mimic the natural hydrology better than if the entire BRC must fill before any water

discharges. Additionally, the water discharged from the underdrain is filtered as it passes through the media. This means that a BRC can treat more than the design storage volume. All three flooding tests filtered or retained the design storm because of the continual flow through filter media. Figure 3.5 shows the equivalent runoff depths that were filtered or retained for each flooding test.

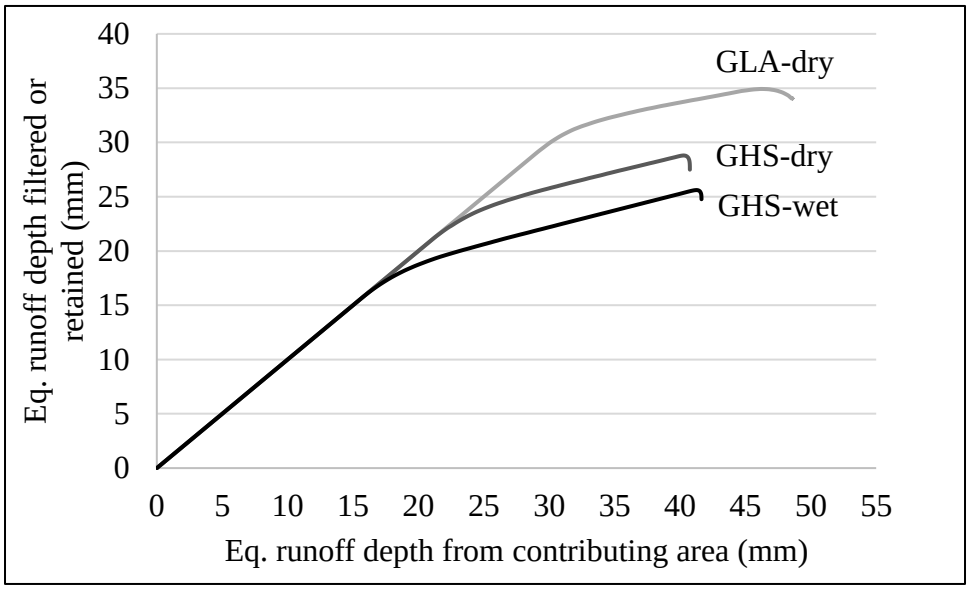

Figure 3.5. Equivalent runoff depth from the contributing area and the equivalent runoff depth that is filtered or retained by the BRC for the Grove High School dry and wet flooding tests and Grand Lake Association dry flooding tests.

The timing of the overflow discharge is important because the overflow rates contributed the majority of the flow to the total outflow rate. Discharge from the overflow began 86 minutes after the inflow for GHS-dry, 64 minutes after inflow for GHS-wet, and 87 minutes after the inflow for GLA-dry. These times follow a similar trend as the underdrain; dry condition flooding tests stored and filtered more water before discharge began. Time to reach steady-state flow rate was also shorter for GHS-wet compared to GHS-dry. A steady-state flow rate occurred 126 minutes (2.1 hrs) into the flood test for GHS-dry, while a steady-state flow rate occurred 108 minutes (1.8 hrs) into the flood test for GHS-wet. GLA-dry reached steady-state overflow discharge 167

minutes (2.8 hrs) into the test. The delay to steady-state flow rate is used here as a surrogate for the impact BRCs? have on peak flows. The delays of steady-state flow rates were 109 minutes (1.8 hrs) for GHS-dry and 94 minutes (1.6 hrs) for GHS-wet. GLA-dry's steady-state flow rate delay was 37 minutes. The shorter delay to peak as well as the longer time to reach stead-state at the inlet is probably the result of groundwater seepage upslope of the BRC inlet.

Time to the end of direct runoff was increased more than the other hydrograph time parameters. The separate hydrograph plots for the underdrains in Figures 3.2 and 3.3 illustrate the differences between the inlet flow durations and the underdrain flow durations. Inflow ended 2.9 hrs, 3.0 hrs, and 4.9 hrs into the flooding test for GHS-dry, GHS-wet, and GLA-dry, respectively. Underdrain flow lasted an additional 13.9 hrs for GHS-dry and 15.6 hrs for GHS-wet. The underdrain during GLA-dry discharged water for 68.1 hrs after the inlet stopped; however, the flow rate did not exceed 0.07 L/s approximately 45 hrs after the inlet stopped. Even though the underdrain flow rate was during GLA-dry was low, the drainage time was more than twice that of GHS-dry and -wet underdrain flow. This is caused by the increased storage volume in the GLA BRC, increased inflow volumes (GLA-dry inlet flow lasted 40 minutes longer than GHS at approximately the same steady-state flow rate), and potential shallow groundwater at the site and seepage upslope of the BRC. Both BRCs in this study lengthened the hydrographs resulting in a more natural runoff condition. The time to the end of direct runoff would only be approximately 40 minutes if the parking lot is modeled as woods and grass in good condition over a type D soil (CN=79) and was exposed to a constant rainfall equivalent to the inflow runoff from the flooding tests. This basic modeling does not account for the contribution retained water has on the timing of base flow discharge. For the simple pre-developed model, the retained runoff percentage was 81%. Part of which would likely become groundwater. At the GHS BRC, having a wet condition increased the hydrograph length. At the start of the GHS-wet tests the native soil surrounding the BRC had a

higher moisture content than the GHS-dry test. This would cause less water to exfiltrate the BRC. The extra water that was discharged during GHS-wet caused the lengthened discharge time from the underdrain.

Water quality

Pollutant concentration reduction

The BRCs in this study were amended with fly ash to provide water quality improvements in addition to hydrologic improvements to stormwater runoff. Flooding tests were completed with municipally treated water from the City of Grove, OK, thus the water quality analysis presented here focuses on leaching potential from BRCs based on concentrations. There are significant differences between the inlet and underdrain for EC, Cl, NO3-N, pH, and turbidity. Orthophosphate concentration did not significantly change from inlet to overflow or underdrain. In general, bacteria were detected in underdrain samples, but not in inlet or overflow samples. A mass analysis for differences between parameters from the inlet to underdrain follow the volume reductions previously discussed because differences between concentrations are relatively small compared to the volume differences. This is important because even though the underdrain discharged contained specific parameters, the total mass leaving the BRC is small relative to the total inflow.

Median values and pairwise comparison of significant differences are listed in Table 3.3. GHS and GLA BRCs reduced EC and Cl in the runoff water. The differences are small because the incoming water was treated municipal water. Turbidity decreased from the inlet to the underdrain for the GHS flooding test but not GLA. A decrease during the GHS flooding tests is unexpected because the incoming water is treated. There is an approximately a 15 cm drop from the parking lot down to a grassed area before the runoff entered the GHS inlet. It is suspected that minor erosion at the drop caused elevated turbidity levels. Regardless, the magnitudes of the turbidity

medians are lower than typical stormwater runoff. Only during GHS-wet did the pH significantly decrease from the inlet to the underdrain. The chemical reduction of nitrate to nitrogen gas produces hydroxyl ions that should cause an increase of pH. Perhaps the pH increase is the result of nitrification of ammonia to nitrite, which produces hydrogen ions. However, this does not explain the decreased nitrate concentration from inlet to underdrain during the wet condition tests. The pH levels for all samples have similar magnitudes. Significant differences of pH may be the result of a type 1 statistical error or the result of unknown processes within the BRC.

Table 3.3. Median water-quality results of samples collected for the entire duration of the Grove High School (GHS)-dry GHS-wet, Grand Lake Association (GLA)-dry flooding tests.. Statistical differences at a 95% confidence level base on Kruskal-Wallis and pairwise comparison. Medians within individual flooding test that do not share a letter are significantly different. Medians without letters have no significant differences.

	GHS-dry			GHS-wet			GLA-dry		
	Inlet	Overflow	Under-drain	Inlet	Overflow	Under-drain	Inlet	Overflow	Under-drain
Number of samples	6	6	11	7	8	14	7	7	14
EC (µS/cm)	314 A	316 A	288 B	299 A	312 A	257 B	262 A	263 A	297 B
Cl (ppm)	14 A	13 AB	8 B	14 A	16 A	9 B	20 A	23 A	8 B
NO_3-N (ppm)	0.40 A	0.38 A	0.59 B	0.38 A	0.37 AB	0.30 B	1.05 A	1.03 A	0.55 B
Orthophos-phate (ppm)	0.04 A	0.04 A	0.03 A	0.03 A	0.03 A	0.03 A	0.04 A	0.05 A	0.04 A
pH	7.7 A	7.7 A	7.6 A	7.7 A	7.6 A B	7.5 B	7.5 A	7.5 A	7.7 A
Turbidity (NTU)	7.80 A	0.91 B	0.84 B	1.44 A	2.02 A	0.47 B	0.78 A	1.23 A	0.75 A

NO3-N concertation reduction varied between flooding experiments. The median NO3-N concentration increased from the inlet to underdrain by 0.19 mg/L during GHS-dry, decreased by

0.08 mg/L for GHS-wet and decreased by 0.50 gm/L during the GLA-dry condition tests. Nitrate leaching from a dry bioretention cell is expected because nitrates can accumulate in the media between storm events (Hsieh et al. 2007). Results from the flooding experiments contradicts this finding. The varied results may be in part attributed to two conditions of the flooding tests; (1) inlet NO3-N at GLA is twice that of GHS-day or -wet and (2) a potential shallow groundwater table at GLA. If the GLA site had a shallow groundwater table, then the groundwater could have diluted the filtered runoff water. The dilution may have cause the measured significant reduction of NO3-N from inlet to underdrain.

Bacteria were found to leach from the GHS BRC during the flooding tests. *E. coli* was detected in all the underdrains samples but in none of the inlet samples and in one of the overflow samples from GHS-wet and GHS-dry combined. The median most probable number (MPN) for underdrain samples during GHS-dry and -wet were 215 MPN and 66 MPN for GHS-dry and -wet, respectively. The single overflow samples for GHS-wet was 10 MPN. Enterococci was detected in all underdrain samples but in none of the inlet or overflow sample for GHS-dry. From GHS-wet, only three underdrain samples, one inlet sample, and two overflow samples had positive enterococci detections. The median was 41 MPN for the three positive underdrain samples from GHS-wet. 10 MPN was the value of the single positive enterococci GHS-wet inlet sample, and 37 MPN was the median of the two positive enterococci GHS-wet overflow samples. The detection limit for all samples was 5.9 MPN on average and ranged from 2 to 10 MPN. Having most samples below the detection limit at the inlet is expected because the inflow water was treated municipal water and travel a short distance before being sampled. Under sample non-detects is most likely occurring because inlet water if flow straight through without interacting with plants for media. In general, there was an evident flushing of bacteria from the BRC's filter media as indicated by the number of positive samples from the underdrain and limited number of

detectable samples from the inlet and overflow. Comparisons of underdrain bacteria samples between dry and wet flooding tests are presented in the antecedent dry period effects section.

Antecedent dry period effects

The antecedent dry period influenced the water quality at the underdrain between GHS-dry and GHS-wet. The median *E. coli*, enterococci, EC, NO3-N, pH, and turbidity levels from underdrain samples were significantly lower during GHS-wet than GHS-dry based on Wilcoxon rank-sum tests and an alpha of 0.05. Box plots of this data are shown in Figure 3.5. P-values for differences are 0.003, <0.001, 0.009, <0.001, 0.002, and 0.001 for *E. coli*, enterococci, EC, NO3-N, pH, and turbidity, respectively. There appears to be a flushing effect from the BRC that was more pronounced during the dry condition flooding tests. Cl and orthophosphate concertation's at the underdrain did differ between the GHS-dry and GHS-wet flooding tests.

Implication on design and performance

Infiltration drawdown rate and time

Long-term success of BRC is very dependent on their ability to infiltrate stormwater and prevent prolonged ponding. During the 7-year period between flooding tests, GHS drawdown rate changed by only 1.0 mm/hr. The average drawdown rate 1 year after installation was 87.5 mm/hr and the average was 86.5 mm/hr 8 years after. In contrast, the drawdown rate for GLA-dry changed from 82 mm/hr to 28.5 mm/hr; a 65% reduction. According to Christianson et al. (2012), the drawdown time 1 year after installation was on average 2.3 hrs for GHS and 2.1 hrs for GLA-dry. These are short times compared to the often 24 to 48 hr maximum time recommended for BRCs. This is in part a result of installing sand plugs to the growth media of the BRCs to ensure adequate drainage. A short drawdown time allows for clogging as a BRC ages while ensuring it meets design standards. After 8 years in the field, drawdown at GHS was 2.3 hrs based on both the dry and wet condition flooding tests. Drawdown time was 6 hrs for GLA-dry, 8 years after

installation. It is expected that both studied BRCs will continue to provide stormwater benefits and meet a 24 hr drawdown time for many years to come if the BRCs progress as they have in the past. It also appears that the use of fly ash in filter media is not preventing drainage in these BRCs.

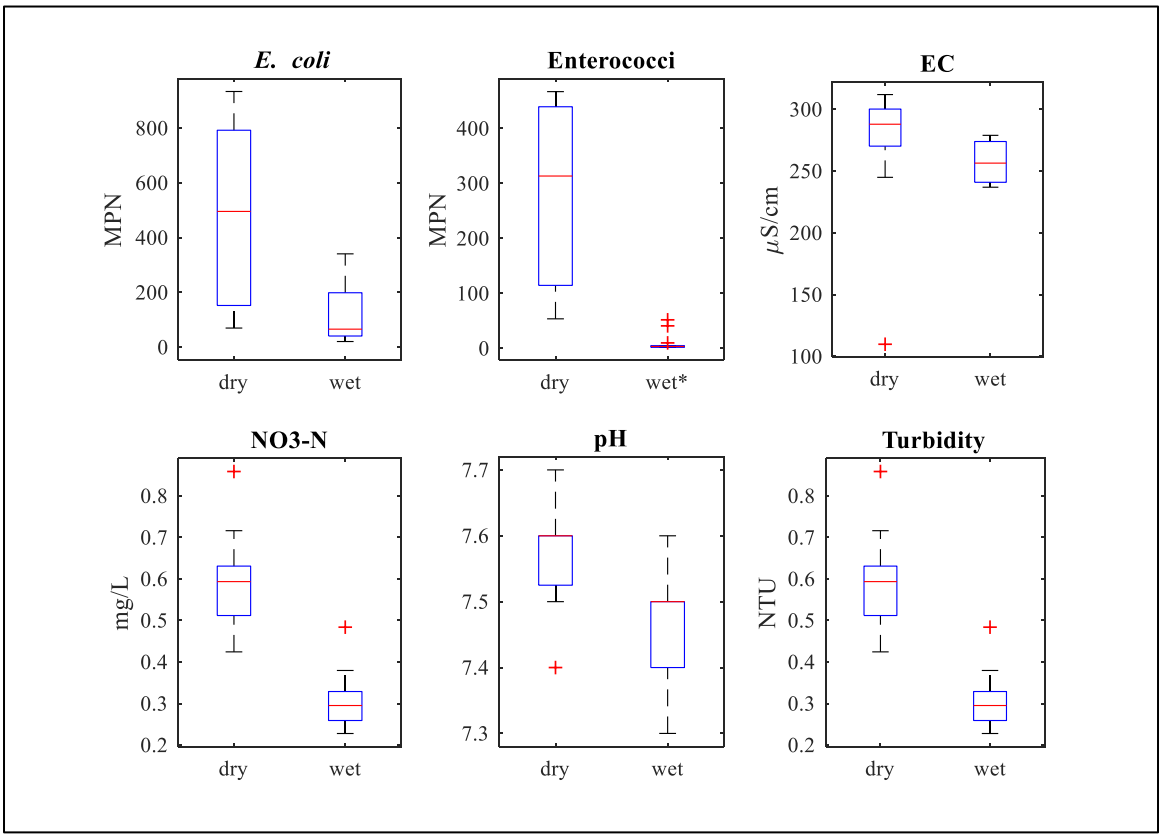

*Figure 3.5. Box plots of data from the underdrain during the dry and wet experiments at Grove High School. Center red line is the median, upper and lower edges of the box are the 75th and 25th percentiles respectively, the whiskers extend to include 99.3% of the data, and the plus (+) symbol indicate outliers. * Enterococci samples that were below the detection limit (11 of 14 samples) were assigned a value of half the detection limit (10 MPN for four the samples and 4 MPN for the seven of the samples).*

Why GHS exhibited minor change and GLA decrease by over 50% is not evident through the data collected. However, the two BRCs have differences that are worth mentioning here. The surface and vegetation of GHS are maintained by the Grove Public School system. During the

study, the GHS BRC was full of vegetation, some of which was installed and some was volunteer. A landscaping company kept the GLA BRC free of miscellaneous plant growth and minimized leaf litter (Figure 3.6). Increased organic matter from plants along with root growth has been shown to improve soil infiltration rates by improving soil structure and creating macropores (Saxton and Rawls 2006; Skorobogatov, 2014; Lefevre et al., 2013). Maintenance activities in the GLA site require repeated trips by a technician through the cell. Over time, this could lead to compaction in the heavily traveled areas. Soils with higher bulk densities will have lower hydraulic conductivities compared to less dense soils with similar textural classifications (Saxton and Rawls 2006).

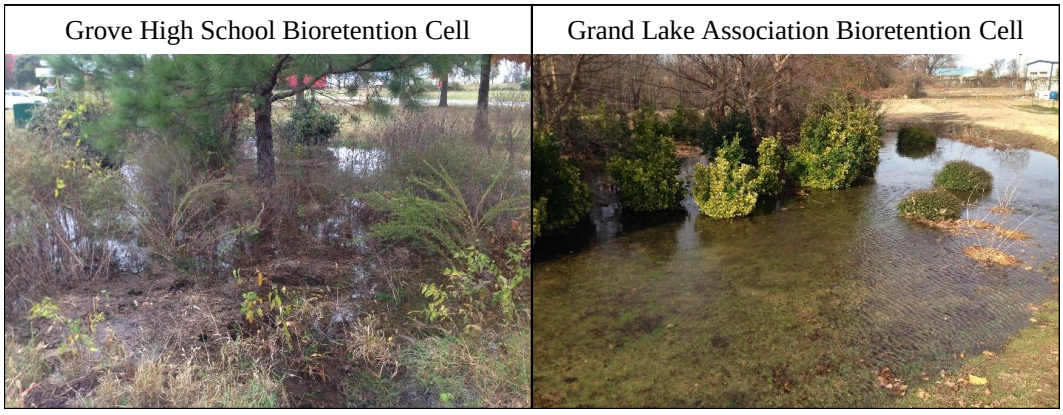

Figure 3.6. Picture of flooding tests at Grove High School and Grand Lake Association bioretention cells during the Fall of 2015.

Stormwater storage capacity

Inflow volume before overflow occurred was quantified to evaluate the first flush treatment capacity of the BRCs. The BRCs are designed to capture 25.4 mm of stormwater. This value is approximately the runoff that would be produced by the 90th percentile storm event in Grove, OK based on a curve number of 98. Table 3.4 list the equivalent runoff depth that would have produced the inflow volumes for GHS-dry, GHS-wet, and GLA-dry flooding tests up to the beginning of overflow. Additionally, the rainfall amount need to create the runoff depth using the

SCS curve number method and a curve number of 98 (impervious surface) is listed. GHS-dry effectively treated the runoff that would be produced by a 25.4 mm storm event. The increased moisture content of the filter media prevented GHS from treating the first 25.4 mm before overflow. GLA-dry treated nearly 25.4 mm. Both of the BRCs treated nearly the design volume 8 years after installation. The difference between GHS-dry and GHS-wet illustrate that moisture content is an important factor. BRCs may need to be overbuilt if they are specifically designed to capture successive storm events.

Compared to 1-year after construction, the storage capacity before overflow began performance for 8-years after varied. GHS-dry was less effective 1-year than 8-years after. This was not expected given that the steady-state flow rate during the 1-year after study was less than the 8-year after study by 1.9 L/s. This suggest that the aging has improved the hydraulics of the BRC. It is suspected that the GHS BRC became more hydraulically connected to the surrounding native soil. This would occur as plant roots grew between the two difference soils. Additionally, there was visual evidence of water flowing up through animal burrowing holes outside of the cell during the flooding tests. Performance GHS-wet decrease by only 0.2 mm of runoff depth before overflow began. The difference is small but may be influenced by reduced porosity caused by settling of the filter median over time. Though, it is important to note that the inlet steady-state flow rate of the 1-year after was 2.4 L/s less than the 8-year after flooding test. GLA-dry retention efficiency of before overflow began decreased by 15.2 mm. The difference is large compared the GHS flooding tests. It also reflects the decrease in drawdown rate for GLA and the greater inlet steady-state flow rate during the 1-year after flooding test.

Often a primary goal of LID is to mimic the natural hydrology of drainage area. The effectiveness of GHS BRC to restore the curve number of their drainage area is presented in Table 3.5. Only GHS was included in this analysis because the volume balance for GLA was effected by

unmeasured flow as described previously. Currently the drainage area is an asphalt parking lot with underlying soil classified as a hydrologic soil group type D. Historically, this site was probably meadow of continuous grass without grazing, which is classified as curve number of 78 for type D soils. When the filter media was drier, the inflow water retained by the GHS BRC lowered the effective curve number to 90 for the 8-years after installation flooding test and 84 for the 1-year after flooding test. Neither time has the BRC restored the native curve number of the site. When wet, GHS lowered the curve number to 92 and 91 for the 8-year and 1-year after installation flooding tests, respectively. To restore the curve number of the site, the retention needs to be 82.5%. This site would benefit from an upturned elbow underdrain because it would prevent the short-circuiting of flow out the underdrain. Additionally, this would provide storage for runoff to exfiltrate the cell rather than leave as underdrain flow.

Table 3.4. Equivalent runoff depths and corresponding rainfall amounts that would create the runoff based on a curve number of 98 for Grove High School dry and wet and GLA-dry flooding tests. Results are presented for this study and from Christianson et al. (2012) 1-year after construction flooding tests.

	GHS-dry		GHS-wet		GLA-dry	
	1 year	8 year	1 year	8 year	1 year	8 year
Equivalent runoff depth from contributing watershed before overflow started (mm)	17.8	21.3	16.2	16.0	33.7	18.5
Equivalent rainfall depth before overflow started, assume CN = 98 (mm)	23.0	26.7	21.4	21.1	39.3	23.8

Table 3.5. Equivalent rainfall depth in and out for the Grove High School bioretention cell based on the inflow volume and outflow volumes during the flooding tests and the contributing area. Additionally, included are the percent reduction and curve number produced by the reduction in runoff depth.

	Equivalent runoff depth		Reduction (%)	Curve number
	In (mm)	Out (mm)		
8-yr dry	40.9	19.1	54	90
8-yr wet	41.7	22.6	46	92
1-yr dry	83.6	45.7	45	84
1-yr wet	41.4	21.8	48	91

Water quality implications

Flooding experiment provided a unique opportunity to evaluate leaching potential of fly ash amended BRCs when flushed with treated municipal water. While the results do not directly mimic stormwater events, they provide insight into the performance back-to-back storm events. Pollutants that accumulated, or possible originated from, the GHS BRC were flushed out in higher concentrations when with the 5-day antecedent dry period flooding test compared to the day-after flooding test. Bacteria level may have been influenced by animals living in the GHS BRC. Voles were visually identified to have created burrows through and out of the GHS BRC. Ortho-phosphate was a water quality parameter that did not have significant differences between the inlet and outlets nor between antecedent dry period at GHS. The BRCs in this study were specifically designed to reduced phosphorus levels entering the nearby lake by amending the filter media with fly ash. Phosphorus export from BRCs has been document by others (Dietz and Clausen 2006; Hatt et al. 2009; Paus et al. 2014). The BRCs in this study appear to be retaining accumulated phosphorus. However, it is important to note that total phosphorus was not quantified in this study.

CONCLUSIONS

Controlled flooding tested were employed to quantify the hydraulics and leaching potential of two BRCs in Grove, OK. Repeated flooding tests were conducted on the GHS BRC to evaluate the impact of soil moisture. Increased soil moisture did not affect peak discharge attenuation, but did reduce retention efficiency and time to peak discharge. The increased soil moisture flooding test, wet condition, was conducted the day after the dry condition test. A flushing effect occurred that caused the underdrain water quality to be better from the wet-condition flooding test. GHS BRC is expected to performed better hydrologically during the dry season when the filter media moisture content is lower, though what quality is expected to be better during the wet season. Peak discharge was reduced by 95% from the inlet to the underdrain for both GHS tests. The retention efficiency was 53% for GHS-dry and 41% GHS-wet. The BRC also increased time until discharge stopped by an average of 14.8 hrs.

The second BRC in this study, GLA, was only flooded once. A volume balance could not be conducted because of unknown sources of discharge from the underdrain, which may be the result of a shallow groundwater table or restrictive layer. Subsurface features can influence the performance a BRC and should be thoroughly investigated if designing to meet specific hydrologic requirements. GLA-dry did delay the peak discharge time and extend the hydrograph to over 45 hrs past when the inlet discharge stopped. It is evident from the GHS and GLA flooding tests that BRCs provide water quality and quantity benefits.

Modified designs could further enhance the benefits of BRCs. Reconfigure the underdrain would prevent the short circuiting of inflow water to the underdrain at the beginning of the runoff event. The underdrain could be placed away from the inlet rather than extending near it. This would force the stormwater to travel a longer distance through the filter media when the filter media is not saturated or increase surface flow distance through the ponded area. To ensure the cell drains

adequately, the excavated surface at the bottom of the filter media would need to be sloped to the underdrain. Another option would be to install a flow restricting outlet where a traditional underdrain would be placed. This could be accomplished by the decreasing the size or number of opening in the underdrain or reducing the size of the underdrain. If the goal is to maximize the percentage of stormwater filtered, a multiple flow rate outlet could be installed. This would be comparable to stormwater detention riser outlets and could be achieved by inverting an upturned elbow underdrain and adding addition, restrictive, lateral pipes at lower elevations.

Flooding tests were a recreation of the flooding tests completed by Christianson et. al (2012), which were conducted 1 year after the BRCs were installed. This allowed for comparison of hydraulics as BRCs age and comparison to design specifications. GHS drawdown rate had minor change over the 7-year period, increased by 1.0 mm/hr, which corresponds to less than 0.1 hr change to the drawdown time. At GLA, drawdown rate increased by 53%, resulting in 6.0 hr drawdown time. Both BRCs drained in less than 24 hrs indicating that the BRCs do not, and according to a linear regression model, will not clog over the next 20 years. Both cells continued to function near design specifications, treating on average 23.8 mm of runoff before overflow began. The addition of fly ash in the filter media does not appear to have a negative effect on long-term infiltration performance. BRCs, when designed appropriately, can be expected to mitigate urban stormwater issues for years. The cell in this study that had the least amount of change from post installation measurements had more vegetation, which was minimally maintained. Controlled flooding testing BRCs proved to be a valid method that may be useful for other LID best management practices.

ACKNOWLEDGEMENTS

The authors thank Brad Rogers and Jason Walker for assistance with the flooding experiments. We also thank the Oklahoma State University fire service training for equipment. Finally, we are

very grateful to Grove Public School and the Grand Lake Association for their commitment to stormwater management by maintaining their BRCs and allowing us to research them.

REFERENCES

Ahiablame, L. M., Engel, B. A., and Chaubey, I. (2012). "Effectiveness of Low Impact Development Practices: Literature Review and Suggestions for Future Research." *Water, Air, & Soil Pollution*, Springer Netherlands, 223(7), 4253–4273.

Anderson, A. R. (2012). "Hydrologic Evaluation of Established Rain Gardens Using a Stormwater Runoff Simulator." University of Nebraska.

Asleson, B. C., Nestingen, R. S., Gulliver, J. S., Hozalski, R. M., and Nieber, J. L. (2009). "Performance Assessment of Rain Gardens." *JAWRA Journal of the American Water Resources Association*, Blackwell Publishing Ltd, 45(4), 1019–1031.

ASTM. (2014). "Standard Test Method for Enterococci in Water Using Enterolert. ASTM D6503-14" ASTM International, West Conshohocken, PA. www.astm.org

Brown, R. A., and Hunt, W. F. (2011). "Underdrain Configuration to Enhance Bioretention Exfiltration to Reduce Pollutant Loads." *Journal of Environmental Engineering*, 137(11), 1082–1091.

Chavez, R. A., Brown, G. O., Coffman, R. R., and Storm, D. E. (2015). "Design, Construction and Lessons Learned from Oklahoma Bioretention Cell Demonstration Project." *Applied Engineering in Agriculture*, 31(1), 63–71.

Chen, X., Peltier, E., Sturm, B. S. M., and Young, C. B. (2013). "Nitrogen removal and nitrifying and denitrifying bacteria quantification in a stormwater bioretention system." *Water Research*, Elsevier Ltd, 47(4), 1691–1700.

Christianson, R. D., Brown, G. O., Chavez, R. A., and Storm, D. E. (2012). "Modeling Field-Scale Bioretention Cells with Heterogeneous Infiltration Media." *Transactions of the ASABE*, 55(4), 1193–1201.

Davis, A. P. (2008). "Field Performance of Bioretention: Hydrology Impacts." *Journal of Hydrologic Engineering*, 13(2), 90–95.

Davis, A. P., Shokouhian, M., Sharma, H., and Minami, C. (2006). "Water Quality Improvement through Bioretention Media: Nitrogen and Phosphorus Removal." *Water Environment Research*, 78(3), 284–293.

Davis, A. P., Traver, R. G., Hunt, W. F., Lee, R., Brown, R. A., and Olszewski, J. M. (2012). "Hydrologic Performance of Bioretention Storm-Water Control Measures." *Journal of Hydrologic Engineering*, 17(5), 604–614.

DeBusk, K. M., and Wynn, T. M. (2011). "Storm-Water Bioretention for Runoff Quality and Quantity Mitigation." *Journal of Environmental Engineering*, 137(9), 800–808.

Dietz, M. E. (2007). "Low Impact Development Practices: A Review of Current Research and Recommendations for Future Directions." *Water, Air, and Soil Pollution*, Springer Netherlands, 186(1–4), 351–363.

Dietz, M. E., and Clausen, J. C. (2006). "Saturation to Improve Pollutant Retention in a Rain Garden." *Environmental Science & Technology*, American Chemical Society, 40(4), 1335–1340.

Emerson, C. H., and Traver, R. G. (2008). "Multiyear and Seasonal Variation of Infiltration from Storm-Water Best Management Practices." *Journal of Irrigation and Drainage Engineering*, 134(5), 598–605.

Hatt, B. E., Fletcher, T. D., and Deletic, A. (2009). “Hydrologic and pollutant removal performance of stormwater biofiltration systems at the field scale.” *Journal of Hydrology*, 365(3–4), 310–321.

Hsieh, C.-H., and Davis, A. P. (2005). “Evaluation and Optimization of Bioretention Media for Treatment of Urban Storm Water Runoff.” *Journal of Environmental Engineering*, 131(11), 1521–1531.

Hsieh, C.-H., Davis, A. P., and Needelman, B. A. (2007). “Nitrogen Removal from Urban Stormwater Runoff Through Layered Bioretention Columns.” *Water Environment Research*, 79(12), 2404–2411.

Hunt, W. F., Davis, A. P., and Traver, R. G. (2012). “Meeting Hydrologic and Water Quality Goals through Targeted Bioretention Design.” *Journal of Environmental Engineering*, 138(6), 698–707.

Hunt, W. F., Smith, J. T., Jadlocki, S. J., Hathaway, J. M., and Eubanks, P. R. (2008). “Pollutant Removal and Peak Flow Mitigation by a Bioretention Cell in Urban Charlotte, N.C.” *Journal of Environmental Engineering*, 134(5), 403–408.

Jarden, K. M., Jefferson, A. J., and Grieser, J. M. (2016). “Assessing the effects of catchment-scale urban green infrastructure retrofits on hydrograph characteristics.” *Hydrological Processes*, 30(10), 1536–1550.

Jenkins, J. K. G., Wadzuk, B. M., and Welker, A. L. (2010). “Fines Accumulation and Distribution in a Storm-Water Rain Garden Nine Years Post Construction.” *Journal of Irrigation and Drainage Engineering*, 136(12), 862–869.

Johnson, J. P., and Hunt, W. F. (2016). “Evaluating the spatial distribution of pollutants and associated maintenance requirements in an 11 year-old bioretention cell in urban Charlotte, NC.” *Journal of Environmental Management*, 184, 363–370.

Kandel, S., Vogel, J., Penn, C., and Brown, G. (2017). “Phosphorus Retention by Fly Ash Amended Filter Media in Aged Bioretention Cells.” *Water*, Multidisciplinary Digital Publishing Institute, 9(10), 746.

Komlos, J., and Traver, R. G. (2012). “Long-Term Orthophosphate Removal in a Field-Scale Storm-Water Bioinfiltration Rain Garden.” *Journal of Environmental Engineering*, 138(10), 991–998.

LeFevre, G. H., Hozalski, R. M., and Novak, P. J. (2013). “Root Exudate Enhanced Contaminant Desorption: An Abiotic Contribution to the Rhizosphere Effect.” *Environmental Science & Technology*, American Chemical Society, 47(20), 11545–11553.

Li, L., and Davis, A. P. (2014). “Urban Stormwater Runoff Nitrogen Composition and Fate in Bioretention Systems.” *Environmental Science & Technology*, 48(6), 3403–3410.

Minnesota Stormwater Manual, (2017). “Design criteria for bioretention.” Retrieved Sept. 9 2016 from https://stormwater.pca.state.mn.us/index.php?title=Design_criteria_for _bioretention&oldid=31585.

Nichols, P., and Lucke, T. (2016). “Evaluation of the Long-Term Pollution Removal Performance of Established Bioretention Cells.” *International Journal of GEOMATE*, 11(24), 2363–2369.

Natural Resource Conservation Service (NRCS). (1986). “Urban Hydrology for Small Watersheds, Technical Report 55.” United State Department of Agriculture. https://www.nrcs.usda.gov/Internet/FSE_DOCU- MENTS/stelprdb1044171.pdf

OKtag. (2007). “Public Domain Relief Map Modified with Oklahoma Outlined.” National Weather Service. 20th January 2007.

Passeport, E., Hunt, W. F., Line, D. E., Smith, R. A., and Brown, R. A. (2009). “Field Study of the Ability of Two Grassed Bioretention Cells to Reduce Storm-Water Runoff Pollution.” *Journal of Irrigation and Drainage Engineering*, 135(4), 505–510.

Paul, M. J., and Meyer, J. L. (2001). “Streams in the Urban Landscape.” *Annual Review of Ecology and Systematics*, 32(1), 333–365.

Paus, K. H., Morgan, J., Gulliver, J. S., Leiknes, T., and Hozalski, R. M. (2014). “Assessment of the Hydraulic and Toxic Metal Removal Capacities of Bioretention Cells After 2 to 8 Years of Service.”

Prince George’s County (PGCo). (2001). “The bioretention manual.” Programs & Planning Division, Dept. of Environmental Resources, Prince George’s County, Md.

Reddy, K. R., Xie, T., and Dastgheibi, S. (2014). “PAHs Removal from Urban Storm Water Runoff by Different Filter Materials.” *Journal of Hazardous, Toxic, and Radioactive Waste*, 18(2), 4014008.

Randall, M. (2011). “Bioretention Gardens for the Removal of Nitrogen and Phosphorous from Urban Runoff.” The University of Guelph.

Saxton, K. E., and Rawls, W. J. (2006). "Soil Water Characteristic Estimates by Texture and Organic Matter for Hydrologic Solutions." *Soil Science Society of America Journal*, Soil Science Society, 70(5), 1569.

Skorobogatov, A. (2014). "Hydrological Functionality of Plants and Its Application to Stormwater Management." Master's Thesis, Graduate Program in Environmental Design, University of Calgary, Calgary, Alberta. 79 pp. Accessed online on August 11, 2017 at http://theses.ucalgary.ca/bitstream/11023/1813/2/ucalgary_2014_skorobogatov_ anton.pdf.

Standard Methods for the Examination of Water and Wastewater. (2005). 21th Edition. Pp 2-47 to 2-48. (Method 2510 B; water EC)

Standard Methods for the Examination of Water and Wastewater. (2005). 21th Edition. (Method 9223 B)

The Mathworks Inc. (2016). "MATLAB - MathWorks." *www.mathworks.com/products/matlab*, <http://www.mathworks.com/products/matlab/>.

U.S. Environmental Protection Agency (EPA). (1979). "*Methods for Chemical Analysis of Water and Wastes*. Pages 353.2-1 to 353.2-5 (nitrate analysis) and 325.2-1 to 325.2-2 (chloride analysis).

U.S. Government. (2016). "Public Domain Map of the United State." Derivative of Map of the geographic boundaries of the various United States Courts of Appeals and United States District Courts. http://www.uscourts.gov/uscourts/images/CircuitMap.pdf. 26th August 2016.

Vogel, J. R., Moore, T. L., Coffman, R. R., Rodie, S. N., Hutchinson, S. L., McDonough, K. R., McLemore, A. J., and McMaine, J. T. (2015). "Critical Review of Technical Questions

Facing Low Impact Development and Green Infrastructure: A Perspective from the Great Plains." *Water Environment Research*, 87(9), 849–862.

Winston, R. J., Davidson-Bennett, K. M., Buccier, K. M., and Hunt, W. F. (2016). "Seasonal Variability in Stormwater Quality Treatment of Permeable Pavements Situated Over Heavy Clay and in a Cold Climate." *Water, Air, & Soil Pollution*, Water, Air, & Soil Pollution, 227(5), 140.

Youngblood, S., Vogel, J., Brown, G., Storm, D., McLemore, A., and Kandel, S. (2017). "Field Studies of Microbial Removal from Stormwater by Bioretention Cells with Fly-Ash Amendment." *Water*, Multidisciplinary Digital Publishing Institute, 9(7), 526.

Zhang, W., Brown, G. O., Storm, D. E., and Zhang, H. (2008). "Fly-Ash-Amended Sand as Filter Media in Bioretention Cells to Improve Phosphorus Removal." *Water Environment Research*, 80(6), 507–516.

CHAPTER IV

PERVIOUS CONCRETE LONG-TERM CLOGGING TRENDS AND EVALUATION OF CLEANING METHODS

This chapter will be submitted the Journal of Hydrologic Engineering, an American Society of Civil Engineers journal.

ABSTRACT

Pervious concrete is a low impact development practice that can provide long-term stormwater benefits when properly constructed and maintained. In this study, the performance of five different pervious concretes were evaluated by monitoring infiltrations rates, assessing restorative cleaning methods, and correlating results with mix design parameters. The tests plots were not maintained during the monitoring period to assess clogging trends. Tests plots were installed on a slope and received stormwater runoff from an upslope impervious surface. Infiltration rates went through three phases: 1) initial decrease, 2) steady infiltration rate, and 3) secondary decrease. The average duration of phases 1 and 2 combined was 650 days, after which the tests plots began to experience considerable performance decreases from clogging. Restorative cleaning methods were tested on clogged tests plots. Water jets and simultaneous

Vactor truck, significantly improved infiltration rates while four other methods did not. Cleaning performance was improved with the addition of water compared to vacuuming dry as indicated by the capture efficiency of small particles. The results indicate that regular maintenance should occur at least annually. Monitoring infiltration rate can improve long-term performance and reduce maintenance by preventing secondary clogging. Additionally, there is potential to influence maintenance requirements with mix design. Increased sand content and water to cement content were negatively related to initial infiltration rate, phase 1 duration, and phase 2 duration. However, increased sand content was positively correlated with cleaning performance. Future pervious concrete applications should consider the impact of mix design on maintenance and clogging rate.

INTRODUCTION

Pervious concrete (PC) is a Low Impact Development practice that when working properly can mitigate many of the negative impacts impervious surfaces have on the ecosystem. Stormwater runoff in urban areas often contains sediments that can cause siltation in waterways (Paul and Meyer 2001). When the polluted stormwater is intercepted by PC, sediments can be captured. Sediments will collect on the PC surface and in the pores or migrate to the subbase. Over time, accumulation of sediments will clog the pores and prevent PC from meeting stormwater management goals. Once clogged, PC must be cleaned to reopen the voids and allow stormwater movement through the PC. In this study, infiltration rate of PC is tracked over time to evaluate clogging trends, and cleaning methods are evaluated for their effectiveness at restoring the infiltration rate of clogged PC.

A typical PC system is composed of the top layer of PC, an aggregate base, and a separating layer between aggregate and underlying soil. PC is made of Portland cement, aggregates, and optionally with admixtures and fines, such as sand, at proportions that create an interconnected pore network. It is the pores that enable infiltration of stormwater, making PC an ideal alternative

for hard surfaces in the urban landscape. The thickness of the PC layer is based on the structural strength needed for the anticipated driving load, where a parking lot is typically 4 to 6 inches thick (Ferguson 2005). The aggregate used for PC is a narrowly-graded coarse aggregate with D_{50} of 5.75 mm ($3/8^{th}$ inch). Void content should be around 20% which is achieved with a water to cementitious material ratio (W:(C+A)) between 0.27 and 0.34. Sand content may range from 5% to 10% of the aggregate portion (S:(S+A)), though sand is not always included (Permeable Pavements Task Committee 2015). Mix design has been investigated for strength, freeze thaw resistance, surface finish, albedo, heat island effects, and void content (Bonicelli et al. 2015; Boriboonsomsin and Reza 2007; Dean et al. 2008). Increasing voids results in decreased strength (Schaefer et al. 2006). The addition of sand to the mix can improve mechanical strength and surface finish, through it reduces infiltration (Bonicelli et al. 2015). Additionally, sand has been added to improve freeze thaw resistance (Kevern et al. 2008). The relationship between mix design and infiltration rate, clogging, and cleaning has not been investigated.

Infiltration rates for PC can vary greatly with values over 84.7 cm/min (2000 in/hr) to near 0 cm/min for clogged systems (Chopra et al. 2010; Ferguson 2005). Typical design values are on the order of a 4.23 cm/min to 21.2 cm/min (100 in/hr to 500 in/hr) (Permeable Pavements Task Committee 2015). Infiltration rate has been shown to increase exponentially with increasing voids (Neithalath et al. 2010). Measuring voids during installation is difficult, therefore density, measured as the fresh unit weight, is often used as the design parameter in place of voids and infiltration rate.

Multiple studies have investigated clogging PC (Balades et al. 1995; Boogaard et al. 2014; Coughlin et al. 2012; Kumar et al. 2016; Lim et al. 2015; Sansalone et al. 2012; Suozzo and Dewoolkar 2012). PC evaluated by Kumar et al. (2016) exhibited a linear relationship between clogging and time over a four-year period. Winston et al. (2016) and Lim et al. (2015) found that the best fit equation to predict infiltration rate versus time was an exponential curve. The PC in

these studies did not receive runoff from impervious surfaces. There are many studies that explore clogging only in a laboratory setting (Andrés-Valeri et al. 2016; Aryal et al. 2015; Coughlin et al. 2012; Deo et al. 2010; Haselbach 2010; Lim et al. 2015; Nichols et al. 2015). Studies that utilize synthetic stormwater and laboratory mixed concrete are limited in their applicability to field installations and large-scale maintenance practices. There is a need to investigate clogging of field installed applications, especially ones that are installed on a slope and receive stormwater runon from impervious surfaces. The influence slope and stormwater runon have on clogging has not be thoroughly investigated.

Clogging is typically considered an issue because it results in reduced infiltration rate and increased cost for cleaning. However, PC has been intentionally used as the surface filter layer for groundwater recharge facilities in the United States and other countries (Hogland and Niemczynowicz 1986; Teng and Sansalone 2004). This application of PC is termed a unit superstructure. Teng and Sansalone (2004) showed that PC can act as a filter, but there is a need to quantify the clogging rate and particles that collect on the surface. In a laboratory study, Sansalone et al. (2012) found that 80% of sediment was filtered by PC and that 100% of particles were filtered for particles greater than 300µm. Welker et al. (2013) also studied clogging. They found that the majority of the particles removed from the pore space were raveled particles, pieces of the PC, but they highlighted the benefits of clogging; filtration and sorption of pollutants to clogged particles. PC concrete as a filter has the potential to provide targeted stormwater treatment, but the long-term usage is reliant on the ability to restore the infiltration rate.

Clogged PC can be cleaned to restore infiltration rate. Many studies have evaluated different cleaning methods (Haselbach 2010; Hein et al. 2013; Kumar et al. 2016; Suozzo and Dewoolkar 2012; Winston et al. 2016). Haselbach (2010) showed that infiltration could be restored with sweeping alone because the clogging was near the surface. Others had less success with sweeping

alone, but recommend pressure spraying and vacuuming. From a brief literature review, Kumar et al. (2016) recommend pressure spraying water and then suction. Winston et al. (2016) showed that high-pressure spraying water and vacuuming was an effective way to restore infiltration rate, but the spraying water and vacuuming occurred on a slight delay rather than simultaneously. Pressure washing with water and vacuuming were found to work better together than either independently by Hein et al. (2013). Suozzo and Dewoolkar (2012) restored the infiltration to 100% of the initial infiltration rate with pressure washing followed by vacuuming. There are many examples showing that a combination of cleaning with spraying water and vacuuming in a single process is effective, but no study has examined the use of a Vactor truck and standard attachments that municipalities may already own.

This paper has three main objectives: 1) quantify and analyze infiltration rate versus time trends without completing maintenance, 2) test and evaluate cleaning methods for restoring clogged PC, and 3) link results from the first two objectives to PC mix design parameters through correlation and regression analysis. The goal of objective 1 is to determine if and how different mixes of PC clog when installed on a slope and receive stormwater runoff from an upslope imperious surface. Objective 2 involves the use of multiple cleaning methods to determine effectiveness to restore clogged PC. This is different from routine maintenance because the PC plots were allowed to clog. Five PC mixes are included in this study, which allows for correlations and regression models be fitted to long-term infiltration rate trends and cleaning performance data.

MATERIALS AND METHODS

Study site description

Five different PC mixtures were installed as demonstration and test plots in Tulsa, OK. The test plots were installed in an existing parking lot (Figure 4.1). Each mix was poured and finished by the same installer and measured 6.1 m by 3.05 m and 0.15 m thick. There is a joint separating each the five mixes in half along the 6.1 m length to create two equally sized sides. Each side is

approximately the size of a standard parking stall. Mixes are numbered 1 through 5 from west to east with the equally sized sides labeled A and B from west to east. Runoff from the impervious area up gradient drains to the test plots and is outlined with a dashed line in Figure 4.1. The contributing impervious area is 344 m^2. The loading ratio, which is the ratio of the contributing impervious area to PC area, is 3.7. The parking lot slope, including the test plots, is 3% on average. Down gradient of the test plots is an impervious concrete apron and curb designed to drain excess stormwater from the site. A slight crown runs north to south through the middle of test plot 4.

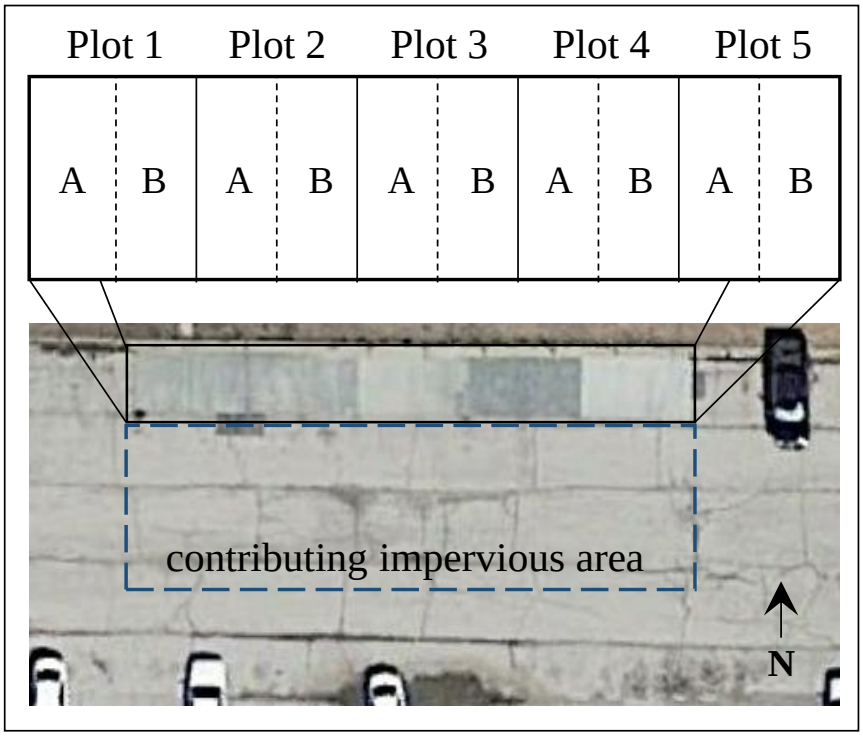

Figure 4.1. Arial view of the pervious concrete plots in Tulsa, OK. There are five different plots which are distinguishable by the different shades of gray in the northern edge of the parking lot.

Mix designs for each of the plots except plot 2 are listed in Table 4.1. Each plot has a different mix design. All but one plot had sand in the mix and the other mix constituents were different except the median aggregate size. The mix proportions were not specifically selected for this research study but rather donated by different companies as demonstrations for the community.

Plots were installed on the same day by a certified company. The PC was delivered to the site in standard concrete mixing trucks. A concrete chute off the back of the mixing truck was used to place the PC. The end of the chute extended to the finished elevation of the PC. Leveling was completed with a vibratory screed. All the plots except side B of plot 5 were finished with a roller. Sides B of plot 5 was finished with hand tools in a similar manner as traditional concrete.

Table 4.1. Pervious concrete mix designs by plot. The mix design for plot 2 is proprietary and not disclosed in this document.

		Plot Number			
Description	**Units**	**1**	**3**	**4**	**5**
Aggregate (A)	(kg)	1130	925	1090	998
Sand (S)	(kg)	68.0	231	68.0	0.0
A+S	(kg)	1198	1157	1158	998
Cement (C)	(kg)	204	280	218	256
Flay Ash (FA)	(kg)	68.0	49.0	38.1	0.0
C+FA	(kg)	272	329	256	256
Water (W)	(kg)	81.6	82.2	69.1	82.9
W/(C+FA)		0.30	0.25	0.27	0.32
(A+S)/(C+FA)		4.40	3.52	4.52	3.90
C/FA		3.00	5.71	5.71	0.00
Sand	(%)	5.7	20	5.9	0
Median Aggregate Size	(cm)	0.95	0.95	0.95	0.95
Design voids	(%)	18	na	na	26.1
Fresh unit weight	(kg/m^3)	2012	2047	1855	2079

Long-term infiltration testing

Infiltration rate was measured on each plot over a period of 2.5 years. During this period, the PC was used daily, but not maintained. The total precipitation during the study period was 97.4 inches and was 0.9 inches below average based on a yearly data. Infiltration measurements were collected according to ASTM C 1701. These long-term measurements were collected near the center of side A on plots 1 through 4 and the center of side A and B on plot 5. Additional infiltration rate measurements were taken during the last four months of the 2.5-year period.

During this time, infiltration rate was measured at 12 locations per plot to increase the spatial distribution of the data set. During these four months, spatial infiltration tests were collected to have 4 infiltration rate measurements per plot in the up, middle, and down gradient regions for a total of 12 infiltration rate tests per plot. Up gradient is located closest to the impervious area and down gradient is near the concrete apron. The spatial tests were completed monthly during the four-month period. Linear regression analysis was completed to quantify trends among the long-term data. Two-sample t-tests were used to test difference between the spatial infiltration rate data to identify clogging trends along the slope. These statistical tests were completed in Microsoft Excel with the Analysis ToolPak.

Cleaning methods

Five different cleaning methods were evaluated: 1) hand vacuum dry, 2) hand vacuum wet, 3) street sweeper dry, 4) street sweeper wet, and 5) Vactor truck wet. Evaluation of cleaning methods began following the spatial infiltration tests. Methods 1 through 4 were evaluated within a month-long period. The total precipitation during this test period was 4.8 inches. Method 5 was completed size months after the spatial test because there were concerns that cold temperatures would cause freeze thaw issues. There was a total of 11.74 inches of precipitation from the end of the first set of cleaning test and the evaluation of method 5. Hand vacuuming was completed with a 3 hp Shop Vac was a 1.25-in diameter brush fitting. Wet hand vacuuming water was completed with the same vacuum and the addition of water sprayed in front of the intake to the vacuum. Water was sprayed through a fan nozzle attached to a garden hose and held at an angle of approximately 45^{o} to the concrete. Direction of the water jet came from opposite the vacuum inlet to encourage uptake of dislodged particles by the vacuum. The street sweeper used in the study was a Tymco 600 regenerative street sweeper with a steel gutter broom. Wet street sweeping was completed by wetting the PC plots with sprinklers overnight prior to cleaning. The street sweeper was driven over the plots multiple times for even coverage with the gutter broom. A Vactor 2100

series was used at a low suction and spraying rate. A 4-nozzle spray attachment was fixed the intake hose of the Vactor truck. Each nozzle produced a jet, so the hose and nozzles were moved back and forth across the pavement surface for even coverage. Figure 4.2 shows dry hand vacuuming, wet street sweeping, and Vactor truck cleaning methods.

Figure 4.2. Pervious concrete cleaning methods. Left: hand vacuuming; Center: street sweeper; Right: Vactor truck

Cleaning methods were completed in sequence as described. Since the tests plots are approximately the size of parking stalls, the street sweeper had to be completed on the entire demonstration surface. To be consistent, the other cleaning methods were also completed on the entire plot. This means that successive cleaning methods were cleaning an area that had already been cleaned by the previous method. After completing each cleaning method, infiltration rate was measured on the spatial grid as described previously. Differences between cleaning methods were quantified with an Analysis of Variance (ANOVA), which was completed in Minitab 17 (Minitab Inc. 2010).

Clogging material characterization

Material collected by the hand vacuum, both wet and dry, was saved for laboratory analysis. Wet vacuum collected material was dried in an oven at 105ºC until all the water was evaporated based on a visual inspection and then for an additional 24 hours. The dry material, from dry and wet vacuuming, was separated using a dry sieving process to particles size ranges shown in Figure 4.3. Many of the particles had cement paste on them indicating that they had broken off the PC through a process known as raveling. Particles greater than 4 mm were visually determined to be

raveled particles because they were covered in cement paste (Figure 4.3). Particles less than 4 mm are therefore classified as clogging particles. After being separated, the mass within each range was measured. Dry and wet vacuuming particle analyses were completed independently.

Statistical relationship to mix design.

Correlations between long-term performance and mix design were quantified with linear regression analysis, which was completed in Microsoft Excel with the Analysis ToolPak and MATLAB (The MathWorks Inc 2016). Pearson's correlations coefficients were calculated between cleaning effectiveness, mix design, and infiltration rate with the Analysis ToolPak in Microsoft Excel.

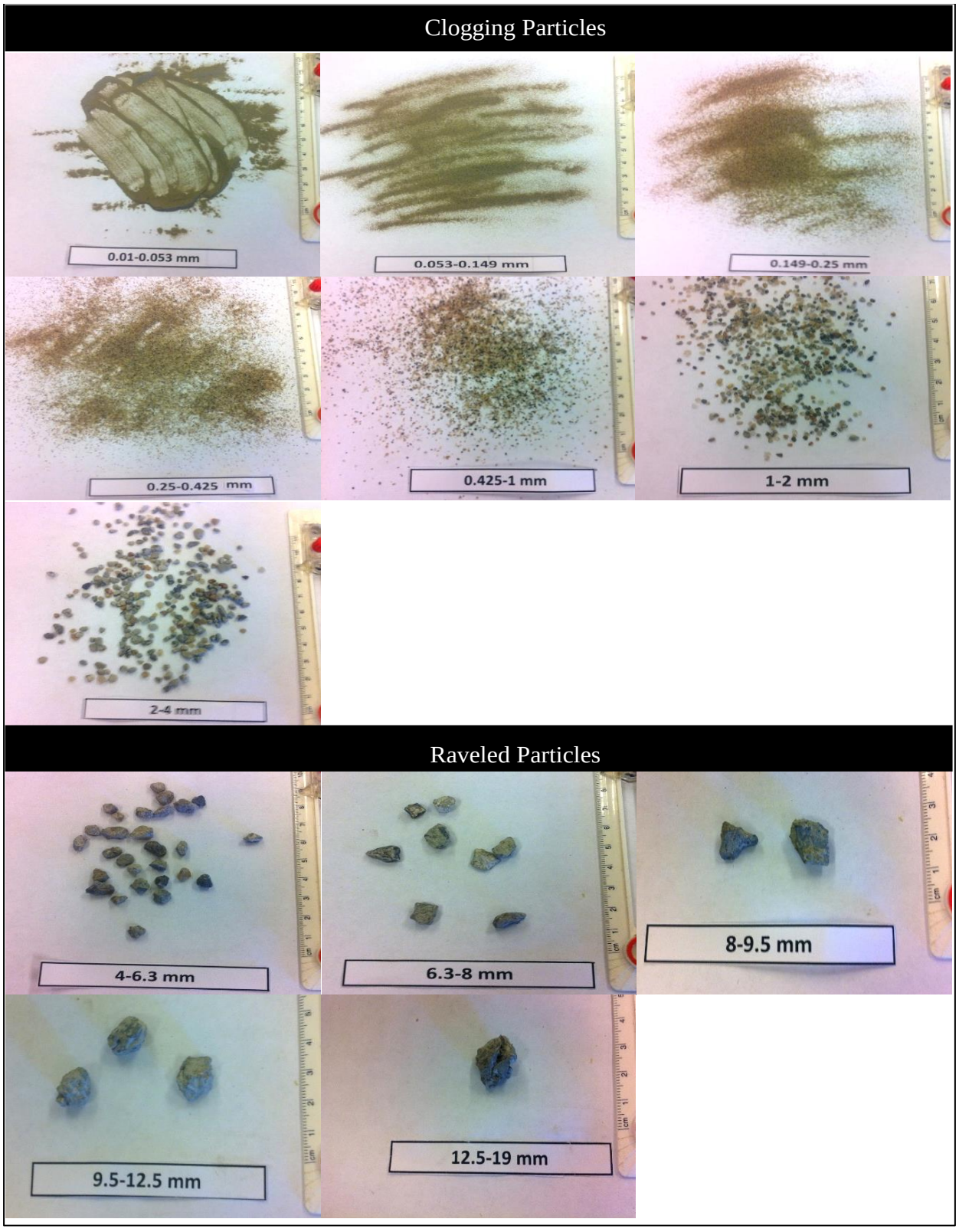

Figure 4.3. Images of particle for each range of sizes analyzed for hand vacuum dry and hand vacuum wet methods. Particles were collected only from side A of each test plot.

RESULTS AND DISCUSSION

Long-term infiltration rate performance

Infiltration rate trends

Infiltration rate for each plot changed phases. There was an initial decrease of infiltration rate for approximately the first 200 days. After which, the infiltration rate remained more constant. After phase 2, another decrease of infiltration rate occurred for all but plot 4. Average slope of linear regression fits for all plots in second phase was -0.006 cm/day, while the slope was -0.10 cm/day on average for the 1st phase. The third phase has an average slope -0.07 cm/day. Measured infiltration rates versus time and fitted linear regression lines to phases 1, 2, and 3 are for all plots and sides A and B of plot 5 are shown in Figure 4.4. Details of the regression fits, durations, and infiltrations rates are listed in Table 4.2. The second phase lasted on average 401 days, with plot 4 remaining in this phase throughout the duration of the study. Plot 3 was in phase 2 for 179 days, the shortest of all the plots. Linear regression fits to phases 1 and 3 were strong with R^2 values above 0.81 for all with an average of 0.94. There was no statistically signification relationship at a 95% confidence level between duration and infiltration rate during phase 2 for any of the plots.

The slope of the PC and the upgradient impervious surface is the probable cause of the three-phase clogging progression. It is theorized that Phase 1 is the result of small pores clogging by sediments transported by wind, on vehicles, or suspended in stormwater runon. The infiltration rate remained steady in phase 2 as larger pores remained open to flow. Long-term infiltration rate measurements were taken in the center of the plots, which is the midpoint along the gradient. There was visible evidence that larger sediments were washing onto the plots from upgradient. Over time, the large particle clogging progressed down the gradient until it reached the location of the long-term measurements. This resulted in the secondary decrease of infiltration rate, the third phase.

Impact of a gradient and contributing impervious surface

Decrease of the infiltration rate with time indicated that the PC was clogging over time. Spatially intensive infiltration rate measurements were completed monthly from June to August to determine if there were differences along the gradient, as it was suspected and visually confirmed that a large particle clogging front was progressing from upslope to downslope. Box plots and individual data points grouped by gradient for plots 1, 2, and 4 are shown in Figure 4.5. These plots have significant differences between the infiltration rates on the gradients. Table 4.3 lists the P-value for the t-tests between gradients for these plots. Up gradient is significantly lower than the down gradient on plots 1 and 2 with P-values of 0.027 and 0.013, respectively, at an alpha of 0.05. Plot 4 does not follow this trend, suggesting that it is not clogging and supports the findings that it remained in phase 2 throughout the duration of the study.

The statistical significance between down-gradient and middle-gradient for plot 4 illustrates the variability among the infiltration rates of the plots, though, the magnitude between differences within plot 4 are minimal compared to infiltration rates between plots. Natural variability of infiltration rate within plots may be the reason that no differences were detected along the gradient for plots 3 and 5. Although, lack of significant differences along the gradient in plots 3 and 5 may also be contributed to the phase 3 ending time; 827 days and 725 days for plots 3 and 5, respectively. Plots 1 and 2 did not end until 921 days. Based on the spatial infiltration rate measurements, nearly the entire surface of plots 3 and 5 were clogged. Clogging at all spatial measurement points suggests that the large-particle clogging front had migrated down the entire gradient.

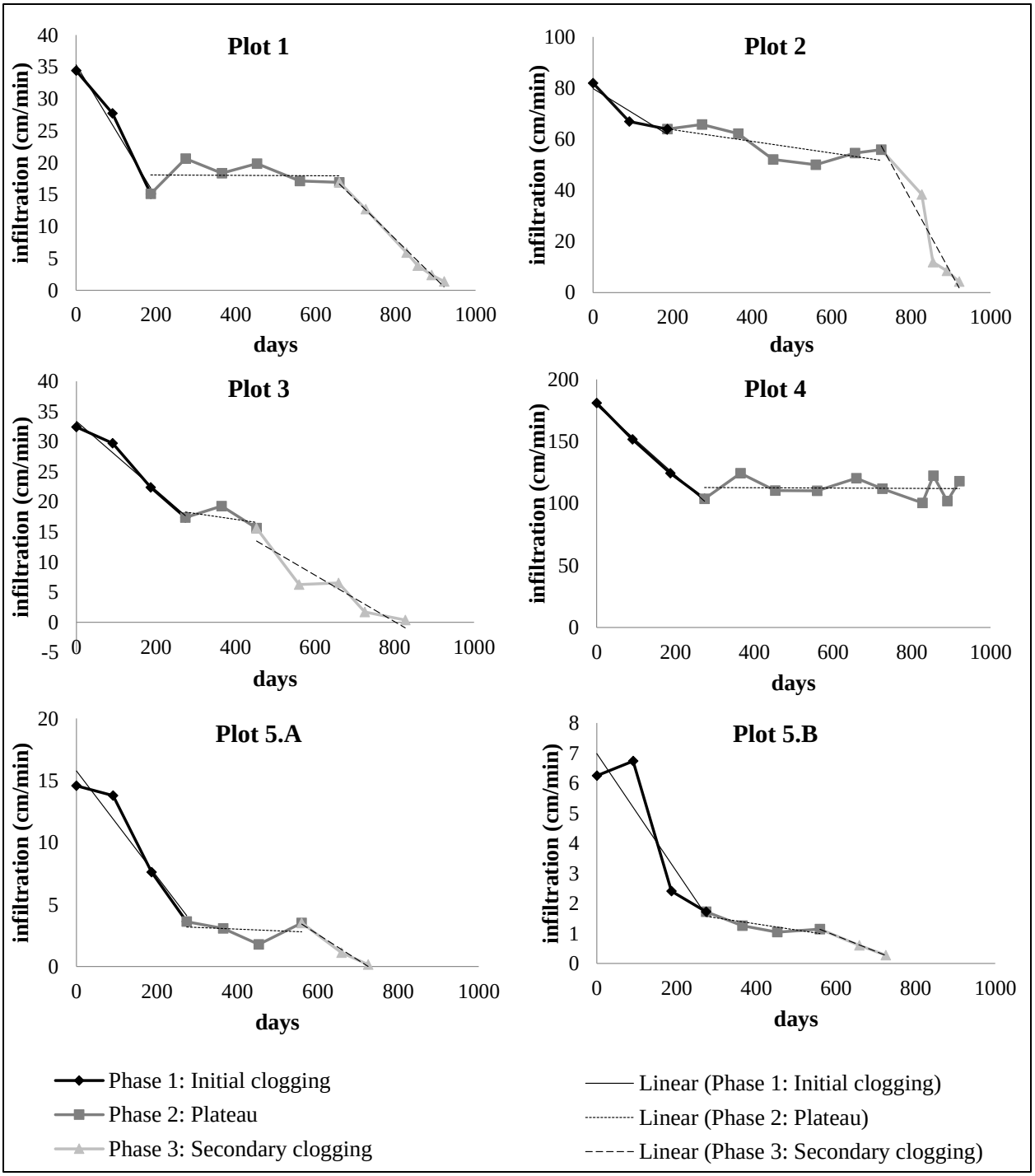

Figure 4.4. Long-term infiltration rates and linear regression fit to clogging phases. No cleaning occurred during the presented time period.

Table 4.2. Long-term infiltration rate linear regression slopes, intercepts, and fits.

		Plot					
		1	2	3	4	5.A	5.B
Phase 1	initial infiltration rate (cm/min)	34.4	82.0	32.4	181.0	14.6	6.2
	duration (days)	187	187	274	274	274	274
	slope (cm/min/day)	-0.104	-0.096	-0.057	-0.282	-0.043	-0.020
	intercept (cm/min)	35.4	79.8	33.4	179.2	15.8	6.98
	R-sq	0.98	0.86	0.98	>0.99	0.94	0.81
Phase 2	mean infiltration rate (cm/min)	18.0	57.8	17.4	112.3	3.0	1.3
	duration (days)	472	538	179	647[1]	286	286
	slope (cm/min/day)	0.000	-0.023	-0.010	-0.001	-0.001	-0.002
	intercept (cm/min)	18.1	68.3	20.9	113	3.56	2.12
	R-sq	<0.01	0.55	0.22	<0.01	0.04	0.67
Phase 3	duration (days)	262	196	374	na[1]	165	165
	slope (cm/min/day)	-0.006	-0.283	-0.039	na[1]	-0.021	-0.005
	intercept (cm/min)	57.2	263	30.9	na[1]	15.0	4.08
	R-sq	0.99	0.91	0.87	na[1]	0.98	>0.99

[1]Plot 4 remained in the phase 2 throughout the duration of the experiment.

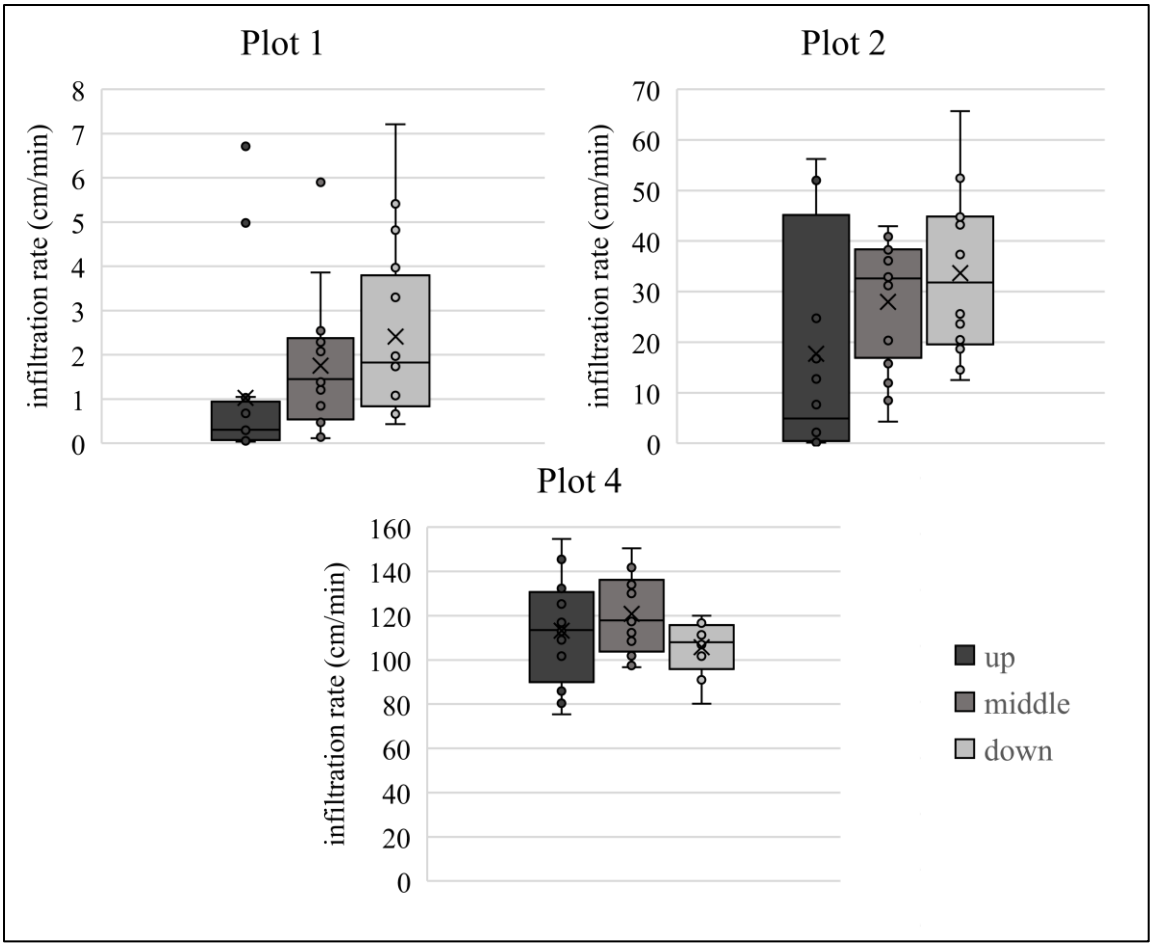

Figure 4.5. Box plots of infiltration rates prior to cleaning for plots 1, 2, and 4 by gradient location. The circles are individual data points, X *is the mean, the bar inside the box is the median, the bottom and top of the box are the 25th and 75th percentiles, respectively, and the upper and lower whiskers cover 99.3% of the distribution.*

Table 4.3. P-values from 2 sample t-tests between gradients (down, middle, and up) based on non-paired data. Grayed values are significant at an alpha of 0.05.

	PLOT 1	PLOT 2	PLOT 4
DOWN VS. UP	0.027	0.013	0.128
DOWN VS. MIDDLE	0.148	0.129	0.003
MIDDLE VS. UP	0.124	0.062	0.152

Cleaning performance

Cleaning method performance

Once PC is completely clogged, it must undergo intensive cleaning to restore the infiltration rate. This is different from routing cleaning, which is intended to maintain PC that has sufficient infiltration to meet stormwater management goals. Multiple restorative cleaning methods were tested, but only the Vactor truck cleaning method statistically improved infiltration rate from the other cleaning methods and the pre-cleaned infiltration rate for plots 1, 2, 3, and 5 (P-value<0.001). Cleaning methods performed on Plot 4 did not significantly change the infiltration rate, though Vactor cleaning was not performed on this plot. Plot 4 was not clogged as indicated by the measured infiltration rates that were still at phase 2 values, therefore Vactor cleaning was not necessary. There were also concerns that the already raveled surface would be further damaged and potentially ruined by the water jets from the Vactor cleaning.

Infiltration rate after Vactor cleaning was similar to the mean Phase 2 infiltration rate but not the initial infiltration rate. Figure 4.6 shows the phase 2 mean infiltration rate, pre-clean mean infiltration rate, and post Vactor clean mean infiltration rate normalized to the initial infiltration rate for plots 1, 2, 3, 5.A, and 5.B. None of the plots had their infiltration rates restored to the initial infiltration rate. At best, the post Vactor clean infiltration rate was restored to 47% of the initial infiltration rate for plot 3. However, Vactor cleaning improved the infiltration rate from the pre-cleaned condition for all plots tested. Plot 2 infiltration rate increased by 4 times pre-clean rate, the minimum of the plots tested, and plot 3 increased by 86 times pre-clean rate, the maximum of the plots tested. Relative to its own infiltration rate, plot 3 was most effectively cleaned. Plot 3 has the closest post Vactor clean mean infiltration rate to its phase 2 mean infiltration rate at 87%. The percent of phase 2 infiltration rate after Vactor cleaning is 69% for plot 1, 45% for plot 2, 77% for plot 5.A, and 53% for plot 5.B. Resorting the infiltration rate to phase 2 does not necessarily indicate high infiltration rates. Plot 2 was the least well cleaned, but

the infiltration rate after Vactor cleaning was the greatest at 25 cm/min. Plot 3, the next greatest infiltration rate after cleaning, was restored to 15 cm/min. The phase 2 infiltration rate may be a better indicator of long-term performance and a realistic infiltration rate for maintenance purposes. Although, higher infiltration rates may be sustainable with regular maintenance prior to reaching phase 2.

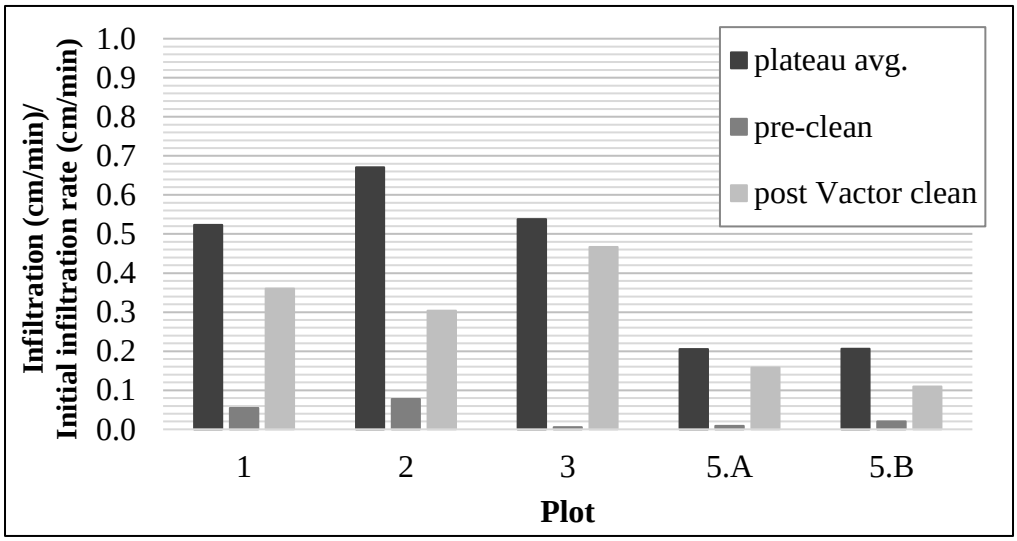

Figure 4.6. Initial, before cleaning, after Vactor cleaning, and phase 2 average infiltration rate relative to the initial rate.

Particle size analysis

Particles collected during hand vacuuming cleaning methods were used to evaluate clogging particles that had accumulated on the surface of the PC plots. The cumulative mass collected during hand vacuuming varies between tests plots. Cumulative mass and cumulative mass distributions are presented in Figure 4.7. These distributions are based on particles size classifications shown in Figure 4.3. It is assumed that no single plot was receiving a meaningfully different quantity or size distribution of washed-on particles because the plots shared a common upgradient impervious surface. Plot 3 differs from the others with the most mass collected over the entire range of particles. This corresponds with the results of the Vactor cleaning. Additionally, plot 3 was the most improved relative to its pre-clean infiltration rate. Plot 3

aggregate content was 20% sand; this may have influenced the performance. Over 50% of the particles collected from plot 4, which maintained the highest infiltration rate over the duration of the study, were raveled particles. The lack of clogging particles from plot 4 supports the long-term results, maintaining an infiltration rate in the phase 2. Plot 1, 3, and 5 have similar cumulative mass distribution curves. Raveling particles are approximately 10% of the cumulative particles for each of these plots. These plots have limited deterioration compared to plots 2 and 4. Fresh unit weights for plots 2 and 4 were the lowest of the test plots in the study at 1954 kg/m^3 and 1855 kg/m^3, respectively.

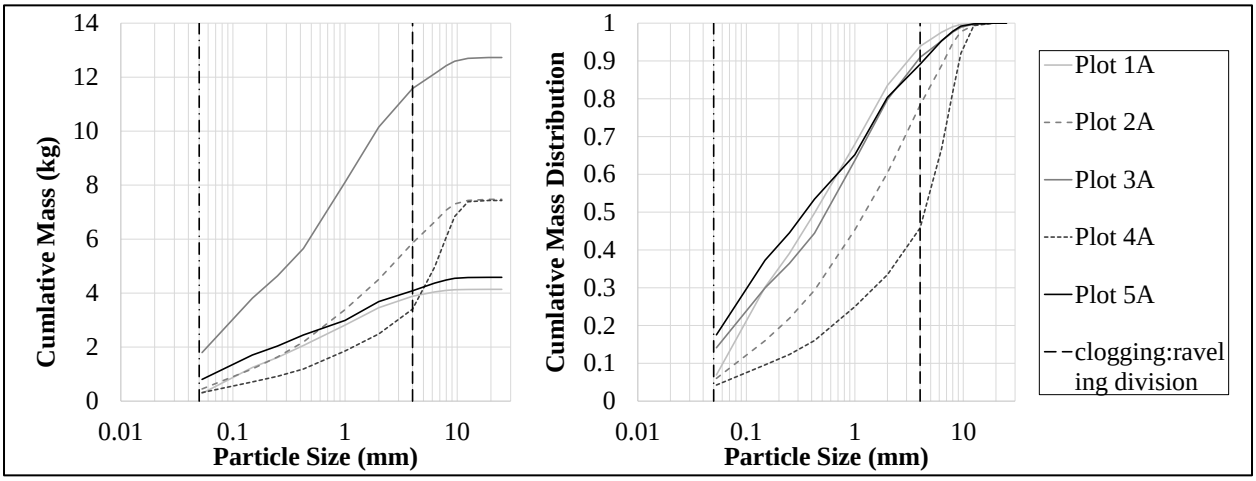

Figure 4.7. Cumulative mass particle size distribution of particles collected during hand vacuuming. Cumulative mass includes particles collected during dry and wet vacuuming.

Impact of water on cleaning performance

Differences between dry and wet hand vacuuming methods were compared to determine if the use of water influences cleaning. Though neither of the hand vacuuming methods significantly improved the infiltration rate, the distribution of particles cleaned from the surface provide insight into the role of water when cleaning. Figure 4.8 shows the percent of particles collected by dry versus wet cleaning for the distribution of particles analyzed. Dry hand vacuuming method was completed first; therefore, it had the first opportunity to collect particles. If both methods were equally effective across all particles sizes than the percentages would not vary greatly, but this is

not the case. Large particles were more successfully collected compared to small particles during dry hand vacuuming than wet hand vacuuming. The percent of particles collected by wet cleaning increased as the particle size decreased in Figure 4.8. This indicates that vacuuming with water was increasingly more efficient at removing clogging particles from the PC surface compared to dry vacuuming.

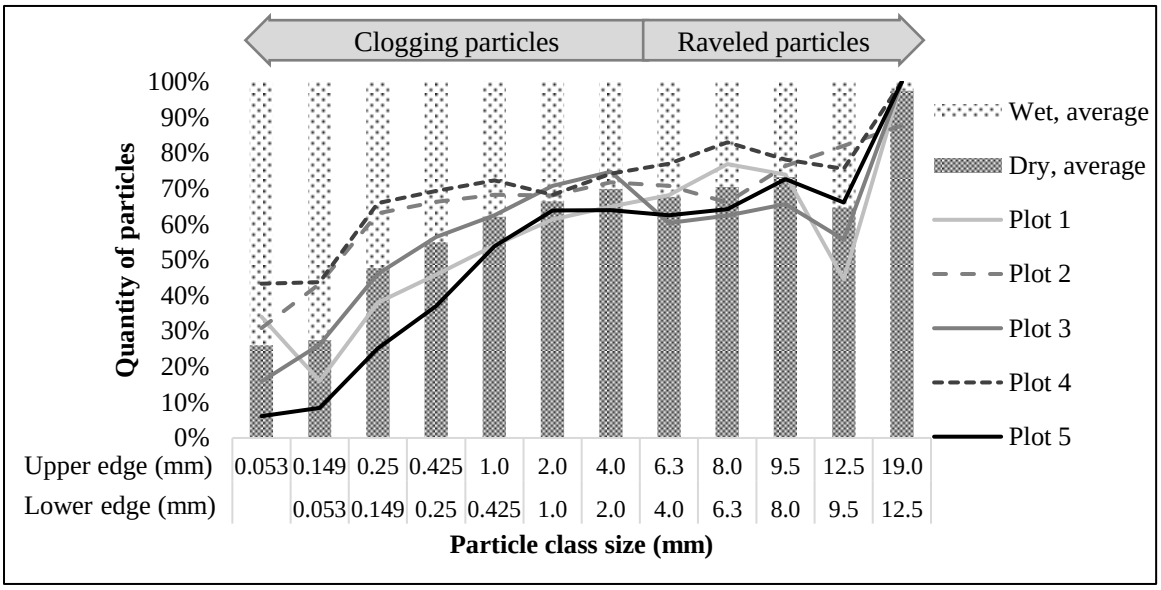

Figure 4.8. Percentage of particles by size from dry- and wet-hand vacuum cleaning for each pervious concrete plot and the average of all pervious concrete plots.

Correlations between clogging, cleaning, and mix design

The unique set of data in this study enable the development of regression equations that link performance over time and cleaning effectiveness to PC mix design. A routinely measured parameter during installation, fresh unit weight, was statistically related to the initial infiltration rate, phase 2 mean infiltration rate, and phase 2 duration. Plotted data and best fit power regression equations of these relationships are shown in Figure 4.9. All the best-fit equations indicate that fresh unit weight is inversely related to parameters shown in Figure 4.9. These relationships are expected because PC with greater fresh unit weight will have in general lower

porosity than low unit weight PC (Kevern et al. 2008; Kia et al. 2017). Infiltration rate and clogging are influenced by porosity (Kia et al. 2017).

The power fit exponents for all the fit equations has a small range, from -18.18 to -18.67, indicating that initial infiltration rate, Phase 2 mean infiltration rate, and Phase 2 duration are related. Initial infiltration rates and phase 2 mean infiltration rates have a strong positive correlation, 0.99 Pearson's correlation coefficient. There is a strong positive correlation between the initial infiltration rate and phase 2 duration, 0.806 Pearson's correlation coefficient. Phase 2 mean infiltration rate and duration also have strong positive correlation, 0.822 Pearson's correlation coefficient. Since these independent variables are actually correlated, measuring one would enable the prediction of the others.

Linking long-term performance measures to mix properties enables the development of tailored PC mixes to meet specific needs. In this study, sand content ratio (S:(S+A)) and the water to cementitious material ratio (W:(C+FA)) were linearly related to the initial infiltration rate, phase 2 mean infiltration rate, and phase 2 duration. Best fit equations and 1:1 plots of these relationships are shown in Figure 4.10. The sand content and the water to cementitious material ratio are negatively related to the each of the dependent variables. A strong fit for each regression model, R^2 values greater than 0.95, was expected because of the strong correlations between the independent variables as described previously.

The ability to predict the long-term performance before clogging occurs provides information about maintenance scheduling. Phase 2 is a period of relatively stable infiltration rates that can be predicated based on mix design and installed fresh unit weight. From the models presented in Figure 4.9 and 4.10, mix parameters can be determined if there is a desired maintenance schedule. For example, a yearly maintenance schedule (365 days) means that the fresh unit weight at install should be at least 2009 kg/m^3. The mix design can vary to achieve a yearly maintenance schedule.

For example, if the sand content is 5% then the W:(C+FA) ratio needs to be 0.30, but if the sand content is 0% then the W:(C+FA) ration needs to be 0.32. Additionally, setting a minimum maintenance cycle allows the designer to determine an expected infiltration rate that can be used to evaluate stormwater management capabilities of PC. For the examples presented here, the phase 2 infiltration rate would be 26.7 cm/min, 20.5 cm/min, and 16.8 cm/min (631 in/hr, 484 in/hr, and 395 in/hr) respectively. A table of Pearson's correlation values for all parameter is provided as supplemental information.

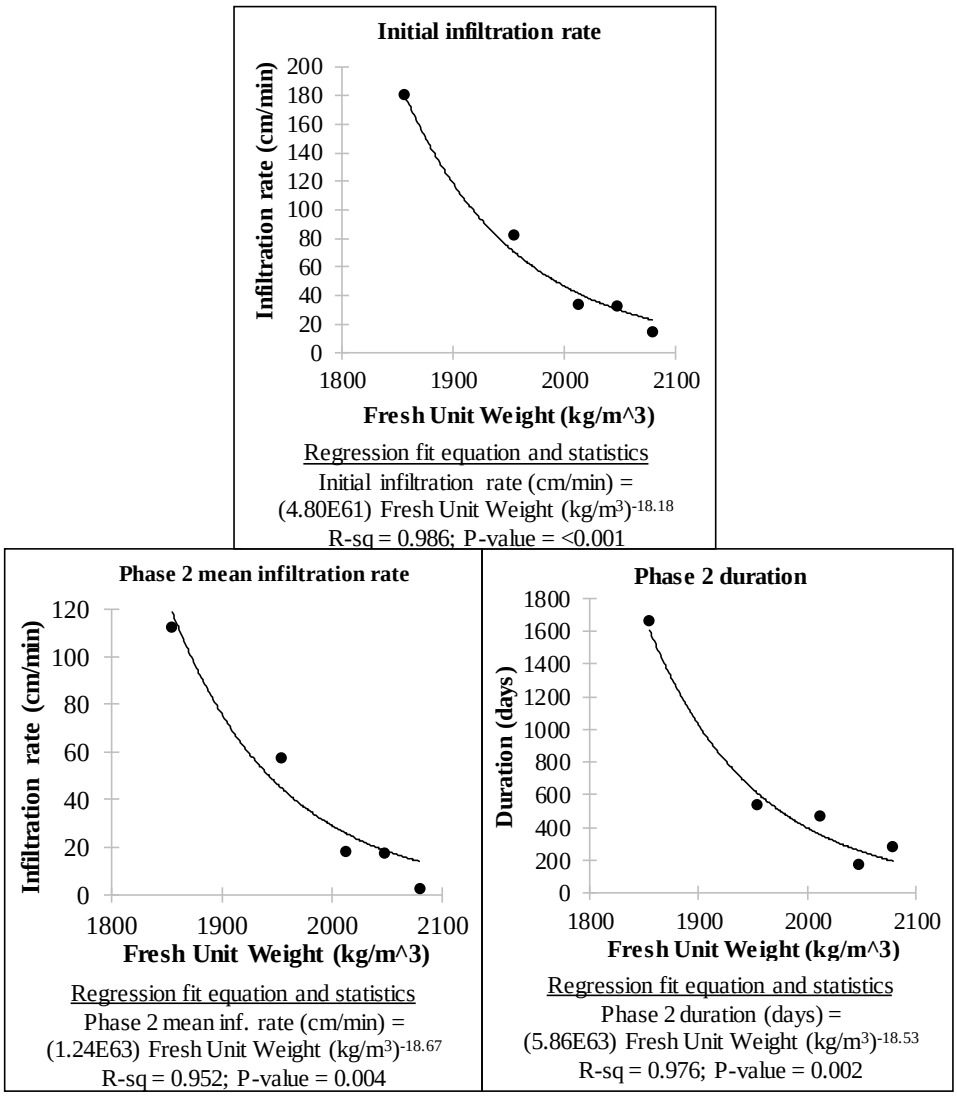

Figure 4.9. Fresh unit weight regression equations with the initial infiltration rate, phase 2 mean infiltration rate, and phase 2 duration.

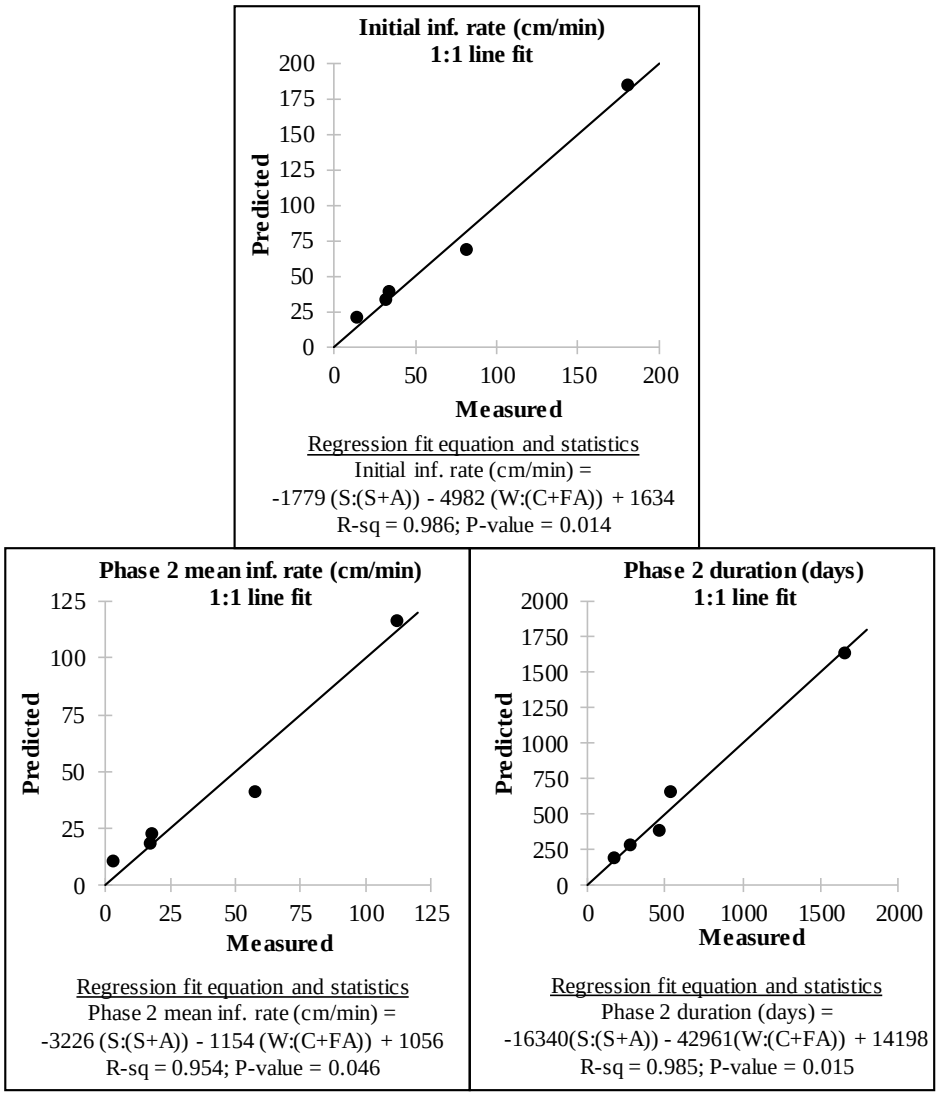

Figure 4.10. Sand content (S:(S+A)) and water content (W:(C+FA)) regression 1:1 fit lines for the initial infiltration rate, phase 2 mean infiltration rate, and phase 2 duration.

An important parameter to consider when designing PC is how well it can be cleaned. From this study, it is apparent that infiltration rate for some mixes can be rejuvenated better than others. Ability to be cleaned as defined by the percent of infiltration rate recovered relative to the phase 2 mean infiltration rate is correlated to mix properties and initial infiltration rate. Pearson's correlation coefficients between the infiltration recovery and multiple parameters are listed in Table 4.4. Fresh unit weight has a strong positive correlation, 0.879, with cleaning performance. This indicates that PC with higher densities are more easily rejuvenated. A PC mix with a very

high fresh unit weight will have little to no pores space. It makes sense that a concrete with little to no pores is effectively cleaned because clogging material cannot enter the pores as there are few of them. If pores do begin to clog, the clogging material will not be able migrate deep within the pores because the pores will be smaller. The opposite occurs when the fresh unit weight is low. In this case, the PC does not clog because clogging material can pass through the pores. While designing for a low fresh unit weight might prevent the need of maintenance do to clogging, it can lead to alternative negative results. Low fresh unit weight PC in this study had increased deterioration as indicated by the quantity of raveled particles collected during cleaning. Decreased strength has been shown to be related to low fresh unit weight (Kevern et al. 2008) There is also the potential for long-term clogging of the geosynthetic material below the sub-base with the material that passes through.

Table 4.4. Pearson's correlation coefficient between the % of the recovery from Vactor cleaning to various parameters.

Parameters	Pearson's correlation coefficient
Fresh Unit Weight (kg/m^3)	**0.88**
S:(A+S)	0.53
W:(C+FA)	-0.42
(A+S)/(C+FA)	-0.63
Initial infiltration rate (cm/min)	**-0.87**

CONCLUSIONS

Five different PC tests plots, which were retrofitted into an asphalt parking lot, were evaluated for clogging and cleaning. The test plots had a slight slope and received stormwater runon from an upgradient impervious surface. Infiltration rate of these plots over a 2.5-year period changed in a patterned that was categorized by three phases. The second phase was a period of relatively constant infiltration rate. The test plots that did not stay in the phase 2 region clogged and needed enhanced cleaning to restore infiltration rate. Allowing PC to clog to phase 3 conditions is not advised, therefore the duration phase 2 may be an indicator of routine maintenance needs. The initial infiltration rate, phase 2 mean infiltration rate, and phase 2 duration are strongly correlated

with the fresh unit weight, sand content, and water content. Regression fit models linking these parameters have R^2 values greater than or equal to 0.952.

An upgradient impervious surface and slope caused the PC plots to clog in the upgradient region first. A clogging front of larger particles progressed down the gradient, eventually clogging the majority of the PC surface. At which point, cleaning was needed to restore the infiltration rate. The clogging front from up to down gradient was evaluated by measuring infiltration rate at multiple locations on the surface of the PC. This type of analysis need to be completed on additional plots to further understand the progression of clogging in PC. Two of the plots in the study were fully clogged by the time spatial analysis was completed, therefore, no differences were measurable even though visual evidence suggested a clogging front from the up-gradient region to the down-gradient region.

Hand vacuuming, street sweepers, and Vactor truck cleaning methods were evaluated to restore the infiltration rate. The addition of water during cleaning improved the removal of smaller particles compared to dry cleaning. The Vactor truck, which involved spraying water while simultaneously vacuuming, was the only method that significantly improved the infiltration rates from clogged conditions. Infiltration rates were restored to values near the phase 2 mean infiltration rate further suggesting the importance of phase 2 as useful parameter for design and maintenance. PC mix impacts not only the infiltration rate, but also the ability to successfully clean or even need to clean the PC surface. The mix that had the most sand experienced better cleaning results, but will require more frequent cleaning because its phase 2 duration is shorter than the others. The mix with the highest fresh unit weight remained in phase 2 throughout the duration of the study suggesting that is an ideal PC if maintenance is not an option. However, this PC plot is weaker than the others and has major issues with raveling.

The results in this study are based on a relatively small set of data points, 5 different mixes, for correlations between mix design and long-term and cleaning performance. These relationships should be further investigated with new mix recommendations and tested in real applications. Additionally, the link between mix design and actual installed PC needs to be further investigated. The only field measured parameter of the mix design was fresh unit weight. Specification for fresh unit weight were listed in the mix design specifications for Plot 4 as 2401 kg/m^3 (149.9 lb/ft^3), while the measured value was 2047 kg/m^3 (127.8 lb/ft^3). This highlights the importance of field measured mix parameters.

REFERENCES

Andrés-Valeri, V., Marchioni, M., Sañudo-Fontaneda, L., Giustozzi, F., and Becciu, G. (2016). "Laboratory Assessment of the Infiltration Capacity Reduction in Clogged Porous Mixture Surfaces." *Sustainability*, 8(8), 751.

Aryal, R., Beecham, S., and Lee, B. K. (2015). "Evaluation of particle transport in permeable pavements under oil loadings." *KSCE Journal of Civil Engineering*, 19(7), 2000–2004.

Balades, J., Legret, M., and Madiec, H. (1995). "Permeable pavements: Pollution management tools." *Water Science and Technology*, 32(1), 49–56.

Bonicelli, A., Giustozzi, F., and Crispino, M. (2015). "Experimental study on the effects of fine sand addition on differentially compacted pervious concrete." *Construction and Building Materials*, Elsevier Ltd, 91, 102–110.

Boogaard, F., Lucke, T., and Beecham, S. (2014). "Effect of Age of Permeable Pavements on Their Infiltration Function." *CLEAN - Soil, Air, Water*, 42(2), 146–152.

Boriboonsomsin, K., and Reza, F. (2007). "Mix Design and Benefit Evaluation of High Solar Reflectance Concrete for Pavements." *Transportation Research Record: Journal of the Transportation Research Board*, Transportation Research Board of the National Academies, 2011, 11–20.

Chopra, M., Kakuturu, S., Ballock, C., Spence, J., and Wanielista, M. (2010). "Effect of Rejuvenation Methods on the Infiltration Rates of Pervious Concrete Pavements." *Journal of Hydrologic Engineering*, 15(6), 426–433.

Coughlin, J. P., Campbell, C. D., and Mays, D. C. (2012). “Infiltration and Clogging by Sand and Clay in a Pervious Concrete Pavement System.” *Journal of Hydrologic Engineering*, 17(1), 68–73.

Dean, S. W., Kevern, J. T., Schaefer, V. R., Wang, K., and Suleiman, M. T. (2008). “Pervious Concrete Mixture Proportions for Improved Freeze-Thaw Durability.” *Journal of ASTM International*, 5(2), 101320.

Deo, O., Sumanasooriya, M., and Neithalath, N. (2010). “Permeability Reduction in Pervious Concretes due to Clogging: Experiments and Modeling.” *Journal of Materials in Civil Engineering*, 22(7), 741–751.

Ferguson, B. K. (2005). *Porous pavements*. Taylor & Francis.

Haselbach, L. M. (2010). “Potential for Clay Clogging of Pervious Concrete under Extreme Conditions.” *Journal of Hydrologic Engineering*, 15(1), 67–69.

Hein, M. F., Dougherty, M., and Hobbs, T. (2013). “Cleaning Methods for Pervious Concrete Pavements.” *International Journal of Construction Education and Research*, 9(2), 102–116.

Hogland, W., and Niemczynowicz, J. (1986). “The unit Superstructure-A New Construction to prevent groundwater depletion.” *Conjunctive Water Use (Proceedings of the Budapest Symposium, July 1986*, 513–522.

Kevern, J. T., Schaefer, V. R., Wang, K., and Suleiman, M. T. (2008). “Pervious Concrete Mixture Proportions for Improved Freeze-Thaw Durability.” *Journal of ASTM International*, 5(2), 101320.

Kia, A., Wong, H. S., and Cheeseman, C. R. (2017). "Clogging in permeable concrete: A review." *Journal of Environmental Management*, Elsevier Ltd, 193, 221–233.

Kumar, K., Kozak, J., Hundal, L., Cox, A., Zhang, H., and Granato, T. (2016). "In-situ infiltration performance of different permeable pavements in a employee used parking lot – A four-year study." *Journal of Environmental Management*, Elsevier Ltd, 167, 8–14.

Lim, E., Fwa, T. F., and Tan, K. H. (2015). "Laboratory evaluation of clogging behavior of porous concrete pavements." *Bituminous Mixtures and Pavements VI - Proceedings of the 6th International Conference on Bituminous Mixtures and Pavements, ICONFBMP 2015*, 1603–1612.

Minitab, Inc. (2010). "Minitab 17 Statistical Software." State College, PA. www.minitab.com

Neithalath, N., Sumanasooriya, M. S., and Deo, O. (2010). "Characterizing pore volume, sizes, and connectivity in pervious concretes for permeability prediction." *Materials Characterization*, Elsevier Inc., 61(8), 802–813.

Nichols, P. W. B., White, R., and Lucke, T. (2015). "Do sediment type and test durations affect results of laboratory-based, accelerated testing studies of permeable pavement clogging?" *Science of The Total Environment*, Elsevier B.V., 511, 786–791.

Paul, M. J., and Meyer, J. L. (2001). "Streams in the Urban Landscape." *Annual Review of Ecology and Systematics*, 32(1), 333–365.

Permeable Pavements Task Committee. (2015). *Permeable pavements*. (B. Eisenberg, K. C. Lindow, and D. R. Smith, eds.), American Society of Civil Engineers.

Sansalone, J., Kuang, X., Ying, G., and Ranieri, V. (2012). "Filtration and clogging of permeable pavement loaded by urban drainage." *Water Research*, Elsevier Ltd, 46(20), 6763–6774.

Schaefer, V., Wang, K., Suleiman, M., and Kevern, J. (2006). "Mix design development for pervious concrete in cold weather climates." *Center for Transportation Research and Education, Iowa State University*, (February), 67.

Suozzo, M., and Dewoolkar, M. (2012). "Long-Term Field Monitoring and Evaluation of Maintenance Practices for Pervious Concrete Pavement in Vermont." *Transportation Research Record: Journal of the Transportation Research Board*, 2292(2292), 94–103.

Teng, Z., and Sansalone, J. (2004). "In situ partial exfiltration of rainfall runoff. II: Particle separation." *Journal of Environmental Engineering-ASCE*, 130(9), 1008–1020.

The Mathworks Inc. (2016). "MATLAB - MathWorks." Natick, MA. *www.mathworks.com/products/matlab*

Welker, A. L., Jenkins, J. K. G., McCarthy, L., and Nemirovsky, E. (2013). "Examination of the Material Found in the Pore Spaces of Two Permeable Pavements." *Journal of Irrigation and Drainage Engineering*, 139(4), 278–284.

Winston, R. J., Al-Rubaei, A. M., Blecken, G. T., Viklander, M., and Hunt, W. F. (2016). "Maintenance measures for preservation and recovery of permeable pavement surface infiltration rate – The effects of street sweeping, vacuum cleaning, high pressure washing, and milling." *Journal of Environmental Management*, Elsevier Ltd, 169, 132–144.

CHAPTER V

MULTIPLE COMPONENT ANALYSIS OF AGED PERVIOUS CONCRETE FROM X-RAY COMPUTER TOMOGRAPHY AND RELATIONSHIPS TO FIELD PERFORMANCE

This chapter will be submitted to Cement and Concrete Research, an Elsevier journal.

ABSTRACT

Pore space is a critical attribute of pervious concrete because it is the conduit for stormwater infiltration and can act as a filter to capture pollutants. X-ray computer tomography was used to non-destructively quantify voids and clogging of four different pervious concrete mixes that had experienced field conditions. Segmentation is one of the most important steps when quantifying material from x-ray images. In this study, a multi-component content frequency fitting process is applied to pervious concrete to quantify pore space, mixed component voxels, and cementitious material. Poristy was on average 5% less with the frequency fitting method compared to Otsu's method. Multiple component classification prevents voxels in regions of high density heterogeneity from being forced into a binary segmentation; voids or solid material. Mixed component content was determined to be an indicator of clogging. Mixed component fraction was generally greatest in the top 10 mm and is an indication of clogging near the surface. The field pervious concrete plots were cleaned after cutting the cores. Cores with less mixed component

content in the top 10 mm correlated to pervious concrete that was more efficiently cleaned.

INTRODUCTION

Impervious surfaces alter the natural coarse of stormwater runoff, which can cause negative effects on the landscape and ecosystem. Pervious concrete (PC), a Low Impact Development practice, is designed to drain surface water to the subsurface and promote infiltration and treatment. Interconnect voids within PC create a network of pores that are the conduits for flows. The void content and size of the pores within PC influences performance. For PC to maintain an infiltration rate for its lifespan, the pores need to not only allow water flow but be resistant to clogging and cleanable.

Proper identification of void space within PC is critical for porosity quantification and analysis of pore size and connectivity. Porosity is often determined by optically surface scanning cut and polished surfaces or imaging with x-ray Computed Tomography (CT). Porosity analysis from cut, polished, and surface scanned cores is common in PC research (Neithalath et al. 2006, Sumanasooriya and Neithalath 2009, Sumanasooriya et al. 2010, Deo and Neithalath 2010, Kayhanian et al. 2012, Radlińska et al. 2012, Rehder et al. 2014). Void and solid content segmentation methods for surface-scanned cut cores are not well defined. This prevents automated and easily repeatable segmenation methods from being applied to other PC samples.

Many x-ray CT based PC research studies use manual or unspecified threshold selection methodology for image segmentation (Teng and Sansalone 2004, Schaefer et al. 2006, Sansalone et al. 2008, Kuang et al. 2011, Meulenyzer et al. 2012). Kuang et al. (2015) segmented CT images with Bayes' discussion theory of pattern recognition while Manahiloh et al. (2012) and Ahn et al. (2014) segmented images with Otsu's method (Otsu 1979). Otsu's method is a common automated global methodology for CT image segmentation (Wildenschild and Sheppard 2013, Iassonov et al 2009). Porosity from CT methods are often validated with gravimetric methods.

Porosity from CT analysis has been reported greater than and less than gravimetric based porosity. Segmentation of PC cores is limited to voids and solid material. Clogging material, cement paste, and aggregates have been directly identified through threshold analysis.

The typical depth of PC is 102 to 152 mm (4 to 6 inches) and is designed to have a porosity of approximately 20% (Permeable Pavements Task Committee 2015; Ferguson 2005). Mix design, compaction during installation, and clogging causes actual porosity in field installations to vary with depth. Porosity has been shown to vary with depth because of compaction (Haselbach and Freeman 2006; Kayhanian et al. 2012; Manahiloh et al. 2012; Meulenyzer et al. 2012; Radlińska et al. 2012). Radlińska et al. (2012) evaluated nine PC cores to determine porosity change with depth. Porosity in the upper 38 mm (1.5 inches) ranged from 1.0% to 10.8% with porosities near the bottom as high as 25.5% but as low as 1.4% (cement to aggregate ratio varied between samples). Haselbach and Freeman (2006) showed that porosity increased in the vertical direction from top to bottom because of compaction during installation. Porosity at the top quarter of a 152-mm (6-inch) slab was on average 5% less than the middle half. In addition, the bottom quarter of field cores had 5% more porosity than the middle half. Porosity profiles were created using x-ray imaging of seven field cores by Kayhanian et al. (2012). In some cases, the upper porosity was less than half the average porosity. Three cores were imaged by Meulenyzer et al. (2012). All three had a linearly decreasing trend for porosity in the upper 70 mm (2.75 inches) and a nearly constant average porosity from 70 to 140 mm (2.75 to 5.50 inches). Lower porosity in the upper portion of the PC causes the pores near the surface to act as a filter, which would cause the surface to clog quicker implying that clogging will occur in the top.

PC clogs as it ages and is exposed to natural urban stormwater conditions. Depth of clogging has experimentally been measured with a microscope to only migrate 12.7 mm (0.5 inches) into the pores (Vancura 2012). Manahiloh et al. (2012) utilized x-ray CT imaging and Otsu's segmentation to quantify clogging in PC cores attributed some of the porosity change to clogging.

They estimated the clogging fraction by taking the difference of segmented images from before and after vacuuming the surface of the cut cores. Kayhanian et al. (2012) utilized x-ray CT to image clogged PC cores that were collected from the field. They concluded that clogging occurred in the top 25 mm (1.0 inches), though, this conclusion appears mainly from decreased porosity near the surface of the cores and no visual evidence is clearly showing clogging material.

Mix design influences porosity and pore size. In general, the porosity is less with larger aggregate but has larger pores compared to PC made with smaller aggregate (Neithalath et al. 2010). Statistical relationship between mix design and PC porosity are lacking. Additionally, there is limited research that utilizes statistically analysis to link mix design, long-term performance (including clogging), and internal characteristics of field aged PC. Past studies that have examined internal features in efforts to quantify clogging have utilized segmentation processes that do not directly account for the clogging material. There is a need to examine aged PC with nondestructive methods that directly identify clogging in an automated process and utilize the results to provide insight into to the influence of mix design on clogging potential.

PC cores collected from the field installed test plots are imaged with x-ray CT with the objective to quantify PC with a multiple component segmentation process. The specific objective are: (1) complete multiple component segmentation with methodology developed by Hsieh et al. (1998) on x-ray CT images of PC cored from a field installation, (2) compare multiple component segmentation results to segmentation results completed using Otsu (1979) methodology, (3) quantify the multiple components relative to depth from the surface, identified clogging, and different PC mixes, and (4) determine trends between segmentation results and known field performance metrics of the sampled PC.

MATERIALS AND METHODS

Site description and coring

PC cores from the Tulsa, OK tests plots described in Chapter 4 were analyzed in this study. Each test plot was installed on the same day. The PC was installed with a vibrating screed and finished with a roller compactor. Clogging was observed for this PC as a decrease in infiltration rate over 2.5 years. Two cores were cut from tests plots 1, 3, 4, and 5. One core per plot was from the up-gradient region and the other in the down gradient region. Cores from plots 1, 3, and 4 were collected from side B, while cores from plot 5 were collected from side A. Cores were cut with 69.85 mm diameter concrete coring bit (Figure 5.1). A small stream of water was sprayed on the outside of the coring bit to cool it. No water was sprayed on the inside bit to minimize cuttings from flowing into the cores and flushing of clogged particles. The cores were cut from the test plots 2.5-years after installation, where not maintenance occurred during this time period. Depth of the PC test plots varied. Core depths are listed in Table 5.1.

Image acquisition and processing

Cores were imaged with a ZEISS Xradia 410 Versa x-ray system, which has a cone beam source (Carl Zeiss X-ray Microscopy, Inc., Pleasanton, CA). System settings for acquisition are listed in Table 5.2. Image reconstruction, including beam hardening and ring artifact removal, was competed with ZEISS Scout-and-Scan Control System Reconstructor (Carl Zeiss X-ray Microscopy, Inc., Pleasanton, CA). Individual images representing a slice through the core equal to the voxel size were exported as 16-bit TIFF (Tag Image File Format) format for analysis.

Table 5.1. X-ray computer tomography image acquisition settings of ZEISS Xradia 410 Versa

Parameter	Value
Lens type	Macro (0.4X)
Source voltage	113 kV
Source current	66.0 mA
Detector charge-coupled device	2,048 by 2,048 pixel
Pixel bin size	2 pixels
Reconstructed image size	1024 by 1024 voxel
Number of projections	2200
Reconstructed voxel size	60.15 μm

Images were cropped for quality control. This includes removal of 50 images from the top and bottom of each image stack. This effectively is cropping in the vertical scale (z-direction) to remove image artifacts. Image artifacts on the circular edge were removed by cropping the images in the x- and y-direction down to 40 mm by 40 mm. Cropping in the x- and y-direction also removes edge effects caused by breaking edge pieces or the migration of cuttings into the pores during cutting. The length of the cores required two separate x-ray imaging scans in order to analyze the top 100 mm of the core. Scans completed on the same core overlapped and image stacks were group together by matching the mean attenuation in the overlapping region. Figure 5.1 shows the relative location of x-ray scans, a single reconstructed image slice from a top scan and from a bottom scan, and an example of the stitching overlap. Directions x and y have no specific directional meaning other than to denote a 90-degree difference in the horizontal plane.

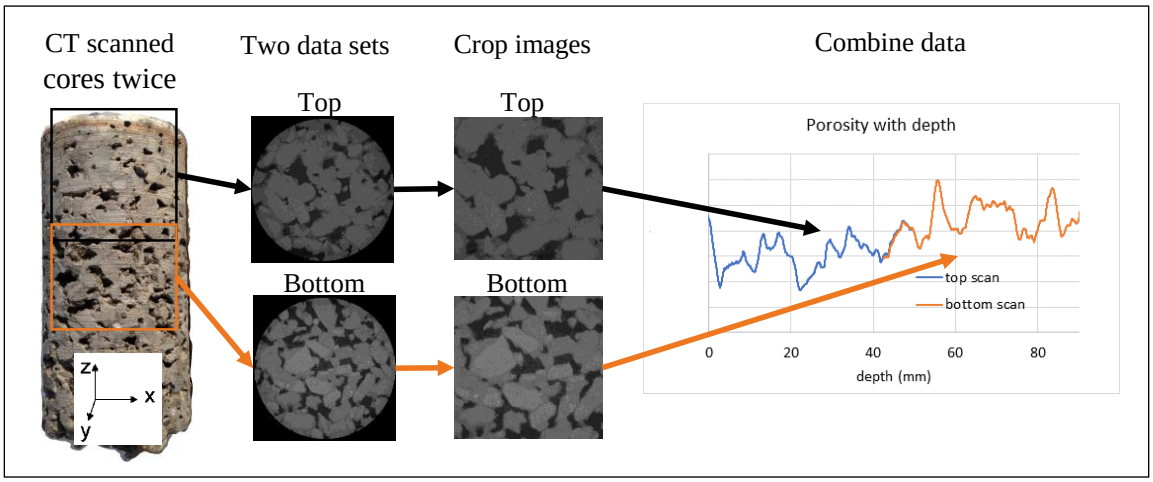

Figure 5.1. General location of x-ray scans and mean attenuation overlap for stitching x-ray image stacks together.

Threshold methods and void space quantification

Two different threshold techniques were completed on the image stacks. Otsu, a common threshold technique that has been used by others to quantify PC (Zhong and Willie 2016, Ahn et al. 2014, and Manahiloh et al. 2012). The second threshold technique is an adaptation of Hsieh et al. (1998) voxel frequency distribution fitting and is referred to here as Hsieh's method. This

method fits theoretical distributions to material-densities histograms of reconstructed image slices. Theoretical distributions are developed from known densities of the scanned material and photon statistics. PC is predominantly composed of void space, cement paste, and aggregate. It may also contain sand, add mixtures, and clogged material. The sand will have a similar density to that of the aggregate and cement paste compared to the void space.

X-ray attenuation is linearly related to the density of the material that it passes through Petrovic et al. (1982) and Orsi et al. (1994). Attenuation can be converted to density with a calibration process. Stacks of reconstructed image slices from the CT scans of the cores require independent calibration coefficients. The calibration process involved converting the voxel value such that the attenuation in the center of clearly identifiable voids matched the density of near zero. In this case the density of air was assume constant for all experiments at 1.15 kg/m^3. To avoid temperature effects on the air temperature, a 20-minute warm-up scan was completed before tomographs were acquired. Then, the adjusted attenuation was converted to density with a calibration coefficient. Voxel densities of reconstructed image slices were calculated as

$$\rho(x,y) = (A(x,y) - C_{void})\,\frac{\rho_{agg}}{C_{agg}} \tag{5.1}$$

where ρ is the density of voxel x, y, A is the x-ray attenuation of voxel x, y, C_{void} is the offset of the voids, ρ_{agg} is the density of the aggregate, and C_{agg} is the calibration coefficient of the aggregate. An assumed value of 2500 kg/cm^3 was used for ρ_{agg} because a system calibration coefficient was not available. C_{void} and C_{agg} were manually determine for each scan by estimating an average attenuation of the known materials through visual inspection.

Images were initially investigated with Otsu's segmentation method (Otsu 1979). This is a common unsupervised histogram thresholding technique that calculates the gray level that corresponds to the maximum variance between the gray level values above and below the

threshold value (Iassonov et al. 2009). The gray level threshold value identified through Otsu's method is then used to segment the image. PC is predominantly composed of void space and cementitious material thus a single threshold value can be applied to identify void content (Zhon and Willie 2016, Ahn et al. 2014, and Manahiloh et al. 2012). Otsu's threshold value was used to segment reconstructed images to quantify void content. Threshold identification and segmentation were completed with the Otsu algorithm in Matlab (The MathWorks Inc 2016).

An alternative approach is to examine multiple components based on their densities and photon statistics. Hsieh et al (1998) showed that for a material composed of pure components, the relative frequency of a voxel being a pure component is defined as

$$f_c(\rho) = \begin{cases} 1\ (R_c), & \rho = \rho_c \\ 0\ (R_c), & \rho \neq \rho_c \end{cases} \tag{5.2}$$

where *f* is the relative frequency, *R* is the fraction of the pure component in the mixture, and subscript *c* denotes the component. Since the voxel size is often larger than pure components, some voxels contained a mixture of materials. Density of a mixed component voxel will be greater than the least dense pure material and less than the densest pure material. Hsieh et al. (1998) showed that the distribution of mixed component voxels can be modeled with a beta distribution.

$$f_m\left(\frac{\rho}{\rho_{max}}\right) = \begin{cases} \left(\left[\left(\frac{\rho}{\rho_{max}}\right)^{\alpha-1}\left(1-\frac{\rho}{\rho_{max}}\right)^{\beta-1}\right]\frac{\Gamma(\alpha+\beta)}{\Gamma(\alpha)\,\Gamma(\beta)}\right)\ (R_m), & 0 \leq \left(\frac{\rho}{\rho_{max}}\right) \leq 1 \\ 0\ (R_m), & elsewhere \end{cases} \tag{5.3}$$

where ρ_{max} is the density of the densest component, α and β define the shape of the beta distribution, and R_m is the fraction of the mixed voxels. Each of the individual components represents a fraction of the scan material, therefore the component fractions are related as

$$1 = \sum_{c=1}^{C} R_c + R_m \tag{5.4}$$

and R_c and R_m must be greater than or equal to 0.

X-ray generation is a random event that induces a normal random error distribution to the image voxels (Brown et al. 1993). Photon statistical errors transform the true density distribution by the Gaussian distribution, $g_c(\rho)$ *(Hsieh, et al. 1998)*

$$g_c(\rho) = \frac{1}{\sqrt{2\pi\,\sigma^2}}\, e^{-\frac{(\rho-\rho_c)^2}{2\,\sigma^2}} \tag{5.5}$$

where g_c represents the statistics of component c and σ is the standard deviation. Photon statistics modify the relative frequency of pure components by completing a convolution of Eq. 5.5 with the relative frequency of the components, Eq. 5.2, and the mixed components, Eq. 5.3. The relative frequency of multiple components with photon statistics is defined as

$$f(\rho) = \sum_{c=1}^{C}\left(g_c * f_c(\rho)\right) + \left(g_m * f_m\left(\frac{\rho}{\rho_{max}}\right)\right) \tag{5.6}$$

where * represents the coevolution of the photon statistics with component fractions.

Fraction of components and mixed components were determined by fitting Eq. 5.6 to the relative frequencies of each image. The known parameters are the component densities. All other parameters were fitted by maximizing the coefficient of determine, R^2. R^2 is calculated as

$$R^2 = 1 - \frac{\sum_{i=1}^{n}(e_i - f_i)}{\sum_{i=1}^{n}(e_i - \bar{e})} \tag{5.7}$$

where f is the fitted frequency generated by Eq. 5.6, e is the empirical relative frequency, and $\bar{e}$ is the mean of the empirical relative frequency. Fitted parameters were determined using an interior-point algorithm as part of the *fmincon* function within Matlab (The MathWorks Inc 2016). The

fitted parameters include α, β, and σ, and the fraction of components; R_v, R_p, R_a, and R_m, which represent the fractions of voids, cement paste, aggregate, and mixed component voxels, respectively.

RESULTS AND DISCUSSION

Multiple component segmentation of pervious concrete

Frequency distributions were successfully fitted for each reconstructed image of the x-rayed cores by implementing a semi-automated process of the Hsieh et al. (1998) methodology. The MATLAB code of the frequency distribution fitting is shown in Appendix A2. Fraction components and the cumulative relative frequency distribution fit for three image slices of 3D are shown in Figure 5.2. Reconstructed images are included with the distribution fits for illustrative purposes. Images were selected from depths of 6.02 mm, 48.12 mm, and 90.23 mm as examples from near the top, middle, and bottom of the core. Cumulative fits are good with R^2 values of 0.961, 0.993, and 0.972 for 6.02 mm, 48.12 mm, and 90.23 mm, respectively. The two predominate peaks in the histograms represent the voids and cementitious material. Cement paste and aggregate are collectively referred to as cementitious material. The region between the voids and cementitious material is fitted as mixed component. In the 6.02 mm histogram, there is a regional peak in the mixed component. This peak is not present in the 48.12 mm, and 90.23 mm, suggesting that high mixed component fractions represent images with higher quantities of heterogeneous regions. This would be an indicator of clogging assuming the quantity of pore edges are constant through all images and image reconstruction does not affect gray level intensity values with depth.

Density of the voids peak shifted between images as did the cementitious material peak. This is caused by image artifacts from CT scanning and image reconstruction. The shifting cementitious material peaks affected proper classification of cement paste and aggregate individually. Figure 5.3 shows the fractions of cement paste and aggregate with depth of core 3D. Fractions of these

materials follow different trends between the top CT scan and bottom CT scan. The trend with depth of the top scan is higher aggregate near the top and less near the bottom. In the bottom scan, the aggregate content is greatest near the middle and less at the top and bottom. Visual identification through segmentation does not support the individual classification of paste and aggregate as correct.

Beam hardening is suspected as the main source of error for proper classification of cement paste and aggregate fraction. Figure 3 illustrates the variability between the cement paste and aggregate fraction for core 3D. X-ray scans were completed by rotating the core sample through a cone shaped x-ray source. Ray paths near the cone's center traveled through more cementious material compared to ray paths near the edges. X-rays passing through more material harden and thus intensity readings are expected to be less in these regions; specifically, the center of the core near the top and bottom a scan. The bottom scan of figure 5.3 has signs of beam hardening near the top (48 mm to 60 mm) and bottom (80 mm to 96 mm). The top scan of figure 5.3 does not follow this trend. It is suspected that increased solid and mixed component material in the upper region of the top scan impacted the beam hardening disproportionality compared to the bottom region of the top scan. This caused over correction by the automated beam hardening correction completed by the reconstruction process, resulting in an increase of the aggregate classification near the top of the top scan. Cement paste and aggregate fraction were inconsistently identified across all cores, so they are presented as a single component, cementitious material. Fraction of cementitious material is not a fitted distribution, but the summation of the cement paste and aggregate fractions.

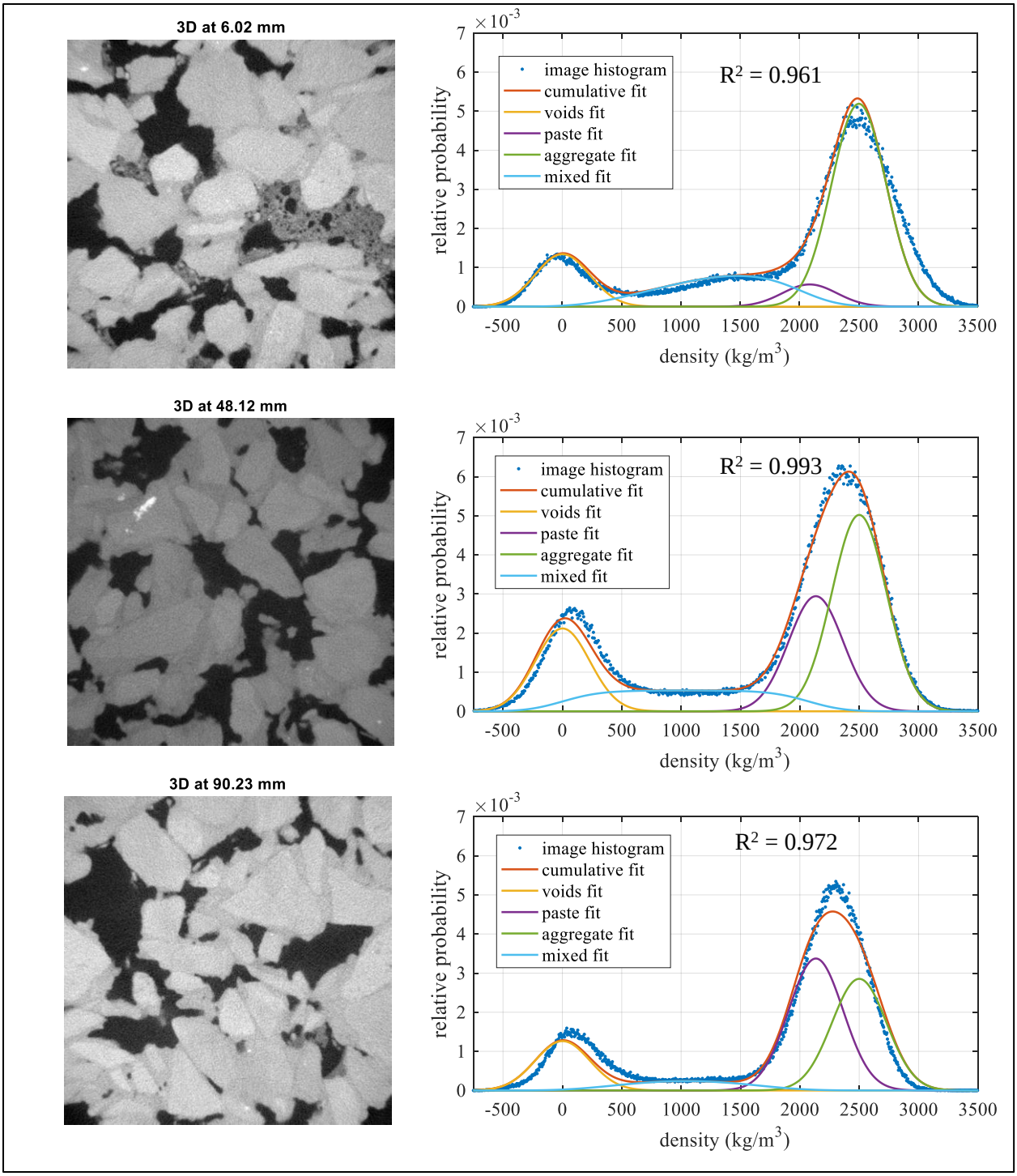

Figure 5.2. Gray level images and corresponding relative frequency distribution of density with fraction component and cumulative fitted curves from Hsieh et al. (1998) methodology. Contrast of image gray level values are enhanced for visual purposes.

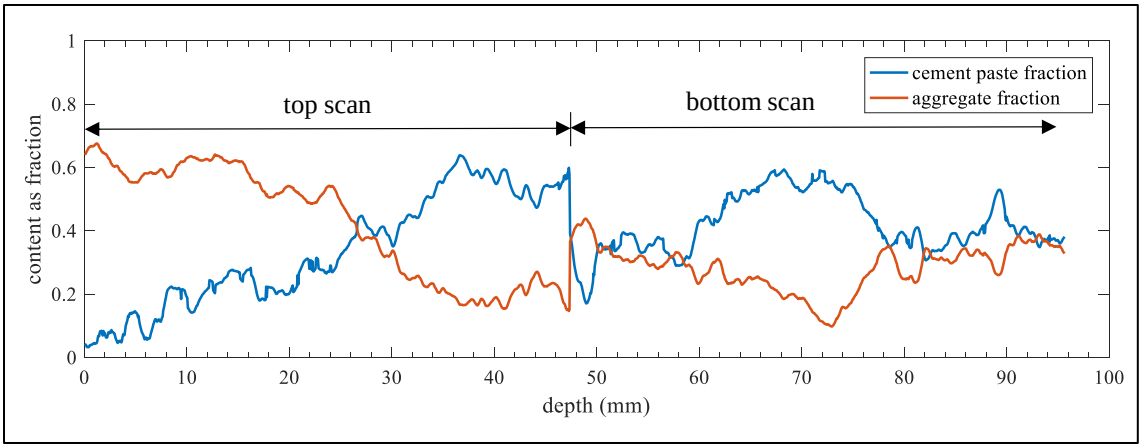

Figure 5.3. Cement paste and aggregate fractions classified by Hsieh et al. (1998) methodology for core 3D. The range of the top scan and bottom scan are identified.

Comparison of multiple component segmentation to binary segmentation

Differences between void content

All reconstructed images were quantified and analyzed to have two primary components, voids and cementitious materials, and a mixed component. For comparison to other segmentation methods, the cementitious material is often referred to here as solid content. Component fraction results from Hsieh method are compared to component fraction from Otsu method. Classification of components differed between the Otsu method and Hsieh method. Figures 5.4 shows the reconstructed image, Otsu void fraction, Hsieh void fraction, and the difference between Otsu and Hsieh void fraction for core 3D at 6.02 mm. The comparison in figure 5.4 visually illustrates the differences between the methods by leaving the segmented data as the actual reconstructed image gray level values. There is a visible difference in the quantity of lighter gray voxels in the Otsu voids image compared to the Hsieh void image. The lighter gray level voxels predominately show up in the difference image between the two methods (figure 5.4 lower left image) indicating that Otsu void content has included non-void voxels.

Average Otsu porosity as indicated by the void fraction content is 24.1%, while the porosity as indicated by Hsieh's void fraction is 17.7%. The difference is caused by the improper

classification of voxels that have a density less than pure paste or aggregate and greater than a void space. The regions of high density heterogeneity are composed of a mix of components with varied densities. The Otsu method does not account for these mixed component voxels when implemented as a binary process; voids or solids only. The regions identified in the difference image appear to contain the clogging material, though the quantity of clogging is not directly measurable from the difference.

Classifying mixed material with Hsieh's method produced a more representative segmentation of the true void content compared to the Otsu segmentation because it rejected the mixed voxels. The void fraction would differ between the two segmentation methods even if the image did not contain the region of high-density heterogeneity. Voxels at the interface between voids and cementitious material contain varying fractions of both components. Classification as a void as is the case with Otsu's segmentation is a miss representation because the known location of material within the voxel is not known and photon statistics indicate that the true density of the voxel may be greater. Component classification by fitting relative frequency distribution accounts for these types of classification errors and is a valid way to quantify voids, cementitious material content, and regions of mixed components. This suggests that the fraction of mixed components may be greater for images with clogging material than those without.

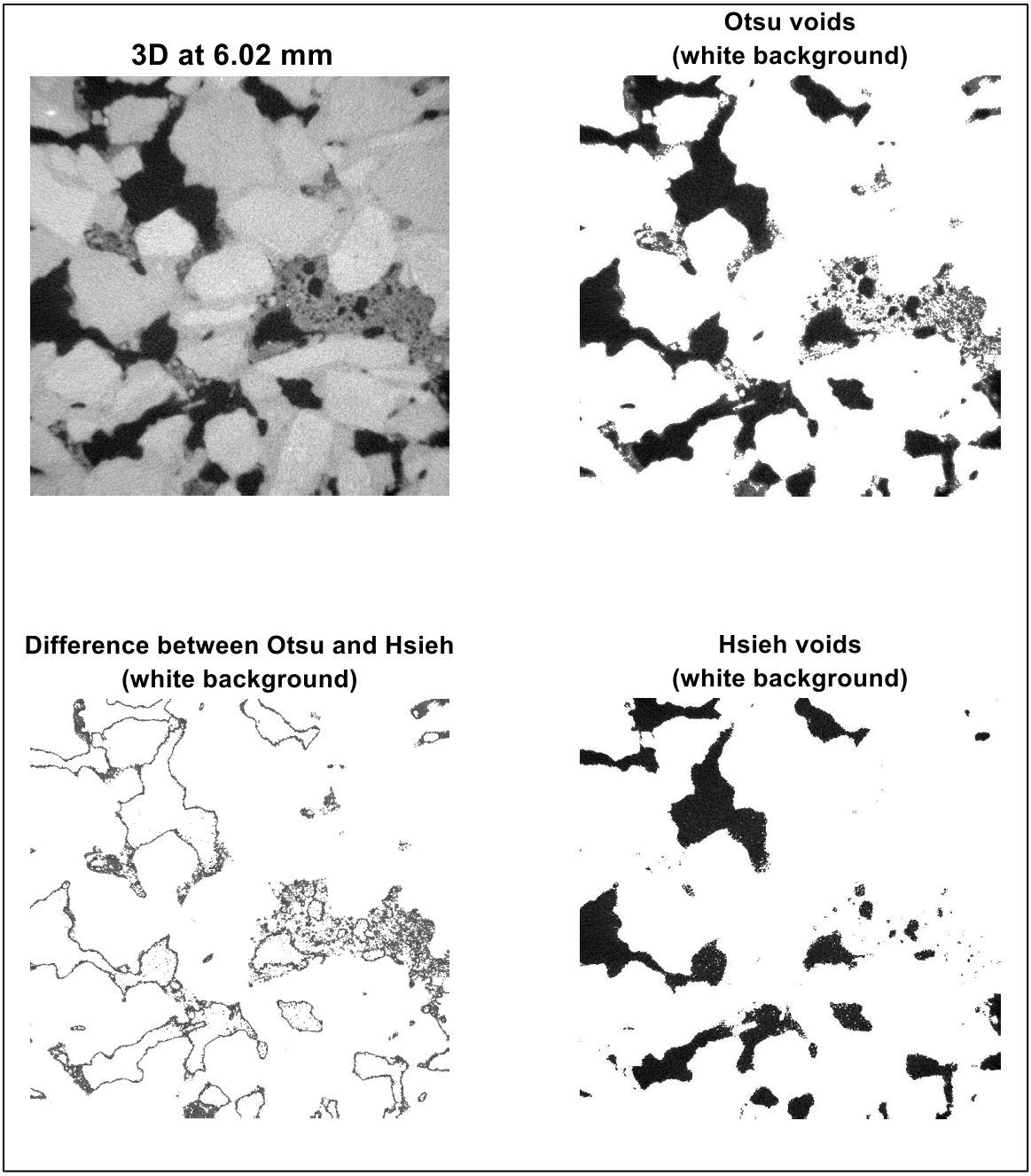

Figure 5.4. Reconstructed image at 6.02 mm for 3D, segmentation of voids with Otsu and Hsieh et al. (1998) methodology, and the difference between segmented images. Segmented voids are shown with their gray level values from the reconstructed image. The background of segmented images is white.

Void content determined with Hsieh and Otsu methodology are plotted against depth for all core are shown in figures 5.5–5.8. Similarities between the methods are visibly evident by the general trends of each curve. Void content with Otsu methodology is always greater than with Hsieh

methodology. This occurs because Otsu void content will in most cases include a partition of mixed component voxels. Differences between the void contents are also plotted in figures 5.5–5.8. It was suspected that the difference would be greater near the surface because of near surface clogging as present in the reconstructed image shown in figure 5.4. Greater differences between void content near the surface is present in 1D, 3D, 5U, and 5D. In contradiction, the difference is near zero or almost constant for cores from 3U and 1U. These cores came from clogged PC plots. The difference between void content for cores from plot 4, which was not clogged, have an increase in the void content difference near the surface. There is not a consistent trend indicting that the difference between the methods is quantifying clogging, but most of the clogged cores have greater differences near the surface. Clogging was visually determined to be near the surface for the clogged cores. Overall, the Hsieh method provides a more accurate assessment of the voids because it rejects the clogging material better than the Otsu method.

Differences between solid content

Solid content fractions from Hsieh and Otsu methodology are plotted in figures 5.5–5.8. The Hsieh solid content is generally less than Otsu solid content, but the two methods are more similar at predicting solid content compared to void content throughout the entire depth of the cores. However, the differences between the methods is often greater than the voids differences near the top of the cores. This trend is more pronounced in core 1U, 1D, 3D, 5U, and 5D. All of the cores came from clogged PC plots. An increase between the solid content differences are similar to the findings shown in figure 5.4 where Hsieh methodology is rejecting clogging material. Plot 4, which was not fully clogged at the time of the cutting, experienced mixed results between the two methods suggesting that clogging cannot fully explain the variation in solid content.

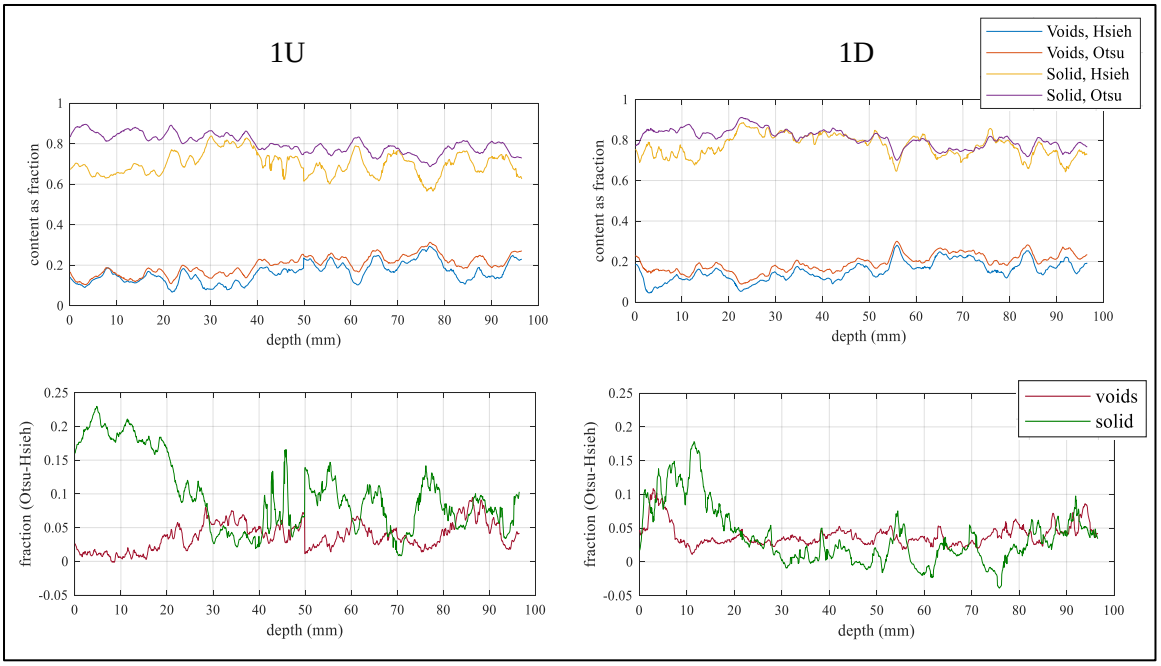

Figure 5.5. Top: plots of voids and solid content from Hsieh et al. (1998) and Otsu methods for cores 1U and 1D. Bottom: plots of the difference of voids with Otsu's methods to Hsieh's methodology and difference of solids with Otsu's methods to Hsieh's methodology for cores 1U and 1D. The top surface of the core is at 0 mm.

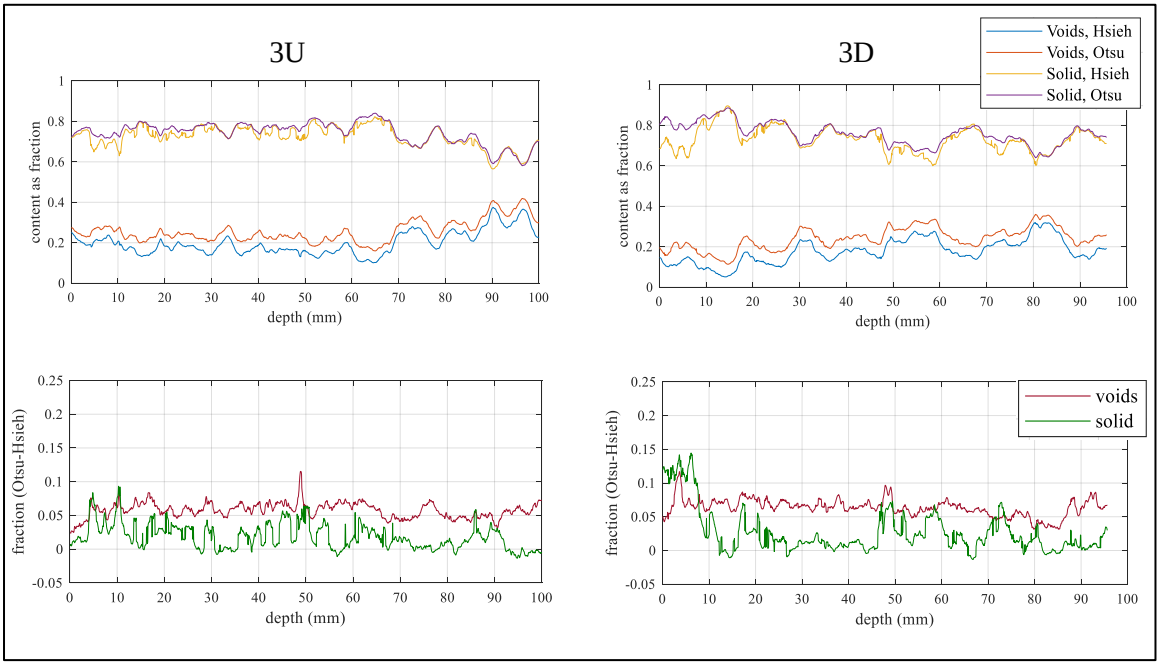

Figure 5.6. Top: plots of voids and solid content from Hsieh et al. (1998) and Otsu methods for cores 3U and 3D. Bottom: plots of the difference of voids with Otsu's methods to Hsieh's methodology and difference of solids with Otsu's methods to Hsieh's methodology for cores 3U and 3D. The top surface of the core is at 0 mm.

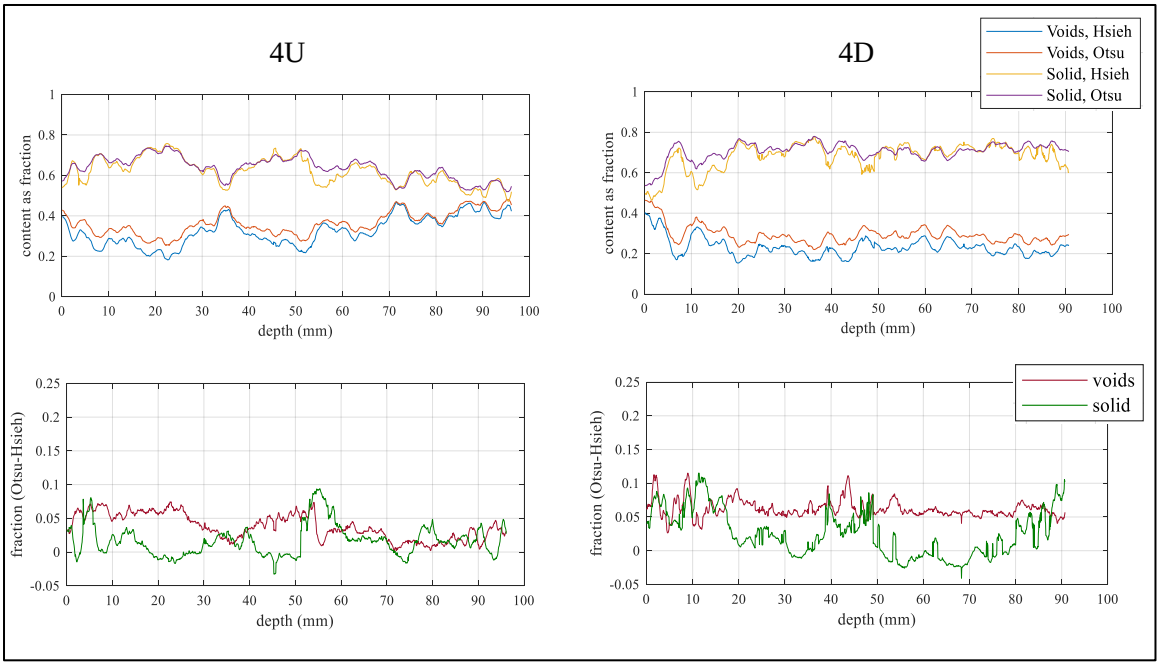

Figure 5.7. Top: plots of voids and solid content from Hsieh et al. (1998) and Otsu methods for cores 4U and 4D. Bottom: plots of the difference of voids with Otsu's methods to Hsieh's methodology and difference of solids with Otsu's methods to Hsieh's methodology for cores 4U and 4D. The top surface of the core is at 0 mm.

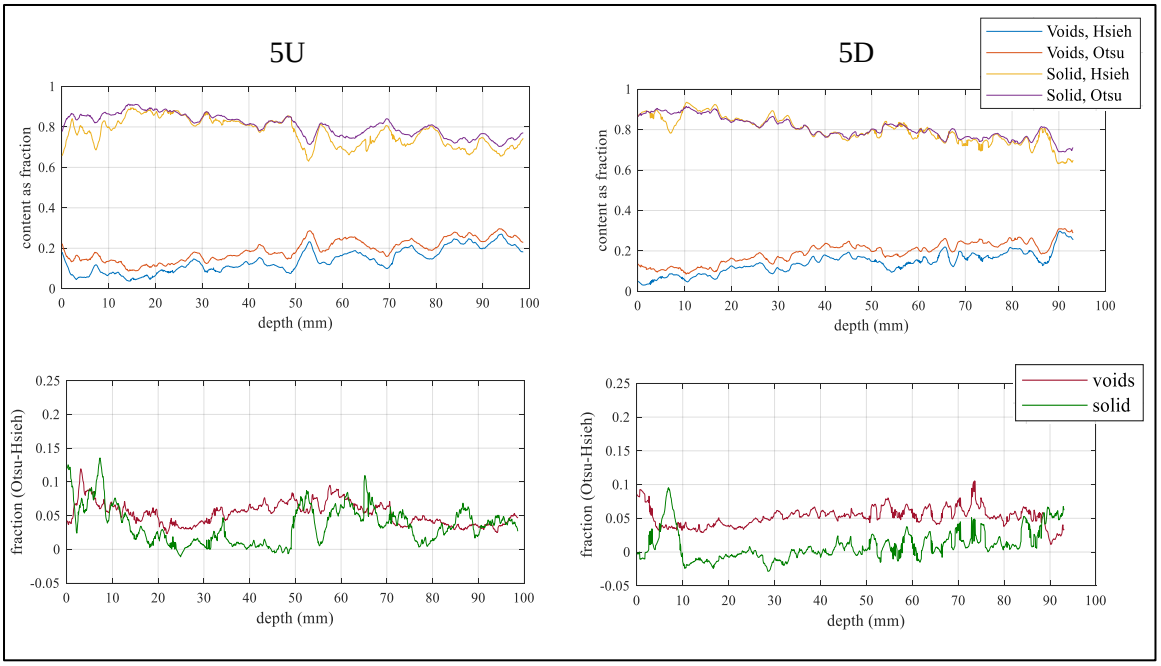

Figure 5.8. Top: plots of voids and solid content from Hsieh et al. (1998) and Otsu methods for cores 5U and 5D. Bottom: plots of the difference of voids with Otsu's methods to Hsieh's methodology and difference of solids with Otsu's methods to Hsieh's methodology for cores 5U and 5D. The top surface of the core is at 0 mm.

Analysis of void, mixed, and cementitious material content

Content trends with depth

Void and cementitious material content determined with Hsieh methodology cycle up and down complementary with depth for all cores (figure 5.9). This is expected as they are dominating components within PC. Mixed component fraction is also plotted against depth in figure 5.9 for all cores. Void and cementitious material fractions vary between cores more than the mixed component fraction. For all cores, mixed component fraction has a max of 0.26 which occurs at 3.6 mm in core 3D. The maximum void fraction is 0.47, which occurs at 72.5 mm in core 4U, and the minimum is 0.03, which occurs at 1.3 mm in core 5D, for all cores. Cementitious material fraction has a maximum of 0.95 at 10.5 mm in core 5D. The minimum cementitious material occurs at 95.5 mm in core 4U and is 0.47. Maximum mixed, minimum voids, and maximum cementitious material content all occur near the top of the cores. These properties should be related to clogging; therefore, the top 10 mm is quantified separately.

The average material content fractions of the cores and the top 10 mm of the cores provides insight into the difference between cores, gradient, and depth. Averages of the void, cementitious, and mixed material fractions are listed in table 5.2. The top 10 mm is included separately because clogging is suspected in this region based on the findings in figure 5.4 and because maximum mixed component fractions occur in this region. In general, the void and cementitious material fractions in the top 10 mm were less than core averages. The top 10 mm has on average 0.03 lower void fraction than the entire core. This occurs because the mixed component fraction was greater in the top 10 mm for most cores. Clogging is considered the primary cause of the differences.

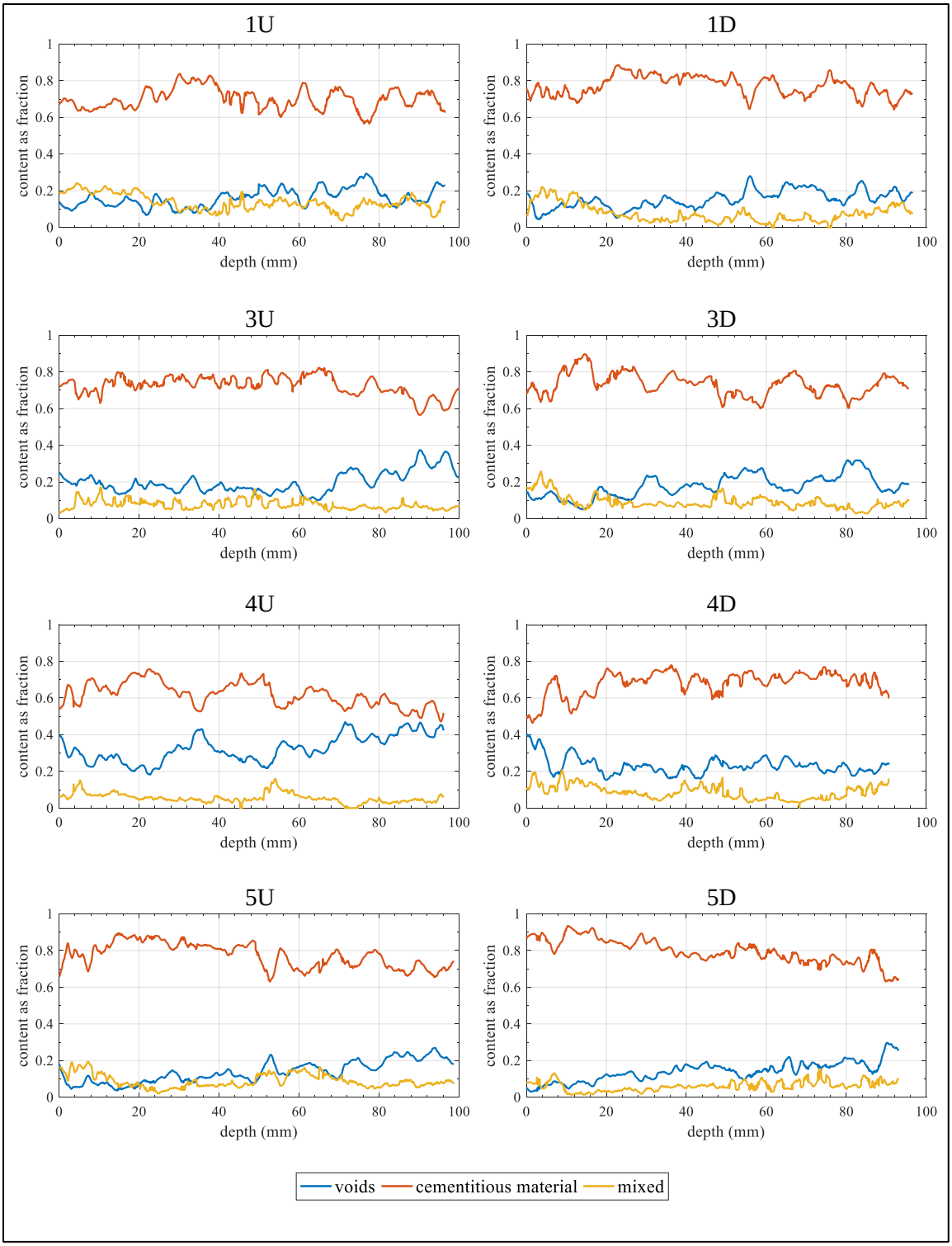

Figure 5.9. Void, mixed, and cementitious material component fractions with depth for cores 1U, 1D, 3U, 3D, 4U, 4D, 5U, and 5D from Hsieh et al. (1998) methodology. The top surface of the core is at 0 mm.

The cores are utilized to represent the PC from which they were cut, but it is important to note that each core represents less than 0.02% of the total surface area of the test plots. There is variability between core void content of cores from the same test plot. The average absolute difference is 0.032 between the void fraction from up-gradient to the down-gradient core from the same test plot. Void content fraction of the top 10 mm had a slightly higher average absolute difference of 0.038 for up compared to down gradient. This may be caused by clogging at the surface. Though, differences between up- and down-gradient were not significantly different at a 95% confidence level when tested with a paired t-test for the core averages nor the top 10 mm averages. Plot 1 was the only plot tested that had significant difference between the up-gradient infiltration rate and down-gradient infiltration rate based on the finding in chapter IV (figure 4.5). Lack of significant differences between up- and down-gradient void content determined from x-ray analysis and Hsieh methodology supports the findings that the plots 3 and 5 were clogged all along the gradient.

Table 5.2. Average void, solid, and mixed content of the entire core and the top 10 mm of each core from Hsieh et al. (1998) methodology.

	Voids		Solid (cementitious)		Mixed	
Sample ID	Core average (fraction)	Top 10 mm (fraction)	Core average (fraction)	Top 10 mm (fraction)	Core average (fraction)	Top 10 mm (fraction)
1U	0.162	0.133	0.702	0.662	0.137	0.205
1D	0.153	0.101	0.771	0.734	0.076	0.166
3U	0.199	0.210	0.726	0.709	0.076	0.081
3D	0.177	0.117	0.733	0.715	0.090	0.168
4U	0.325	0.290	0.620	0.628	0.055	0.081
4D	0.231	0.283	0.682	0.586	0.087	0.131
5U	0.138	0.082	0.773	0.767	0.089	0.151
5D	0.141	0.061	0.797	0.859	0.062	0.081

Component fractions vary with depth (figure 5.9). The void content increases with depth while the cementitious material decreases for all cores except 4D. This is the result of the installation process. A vibratory screed and roller were used to finish the concrete. This caused compaction near the surface. Listed in Table 5.3 are fit coefficients for linear regression models of void content for each core and the void fraction of the core and the top 10 mm of the core. Plot 5 has the lowest average void content (table 5.2) and has the strongest relationship between with depth according to R^2 values. Linear regression models for 1U, 1D, 3U, 3D, and 4U have weak fits as indicated by R^2 less than 0.5. The primary cause of the lack of fit is the cyclic pattern of the void fraction data with depth, which is influenced by the sample size, mix design, and clogging.

Table 5.3. Void fraction and linear regression fit of void fraction with depth of each core and top 10 mm of each core.

Sample ID	Slope (voids fraction/mm)	Intercept (voids fraction)	R^2
1U	0.94×10^{-3}	0.116	0.28
1D	1.10×10^{-3}	0.100	0.41
3U	1.03×10^{-3}	0.147	0.26
3D	1.41×10^{-3}	0.110	0.41
4U	1.72×10^{-3}	0.240	0.47
4D	-0.52×10^{-3}	0.254	0.09
5U	1.75×10^{-3}	0.052	0.74
5D	1.64×10^{-3}	0.064	0.70

Quantification of clogging

The reconstructed image at 6.02 mm depth for 3D was visually selected to be segmented with Otsu's and Hsieh's methods to illustrate what looks like clogging material (figure 5.4). Mixed voxel classification accounts for the voxels that are associated with clogging. Therefore, mixed material can be used as means to quantify clogging in an automated process for all images. An automated process was needed for constancy between classification and to reduce processing time. Approximately 13000 images were processed. Additionally, mixed component fraction was greater in the top 10 mm portion compared to the core averages. This further suggests the

usefulness of quantify clogging with a mixed component fraction because clogging has been found by other to occur in the top portion of PC (Vancura 2012).

Mixed component fraction is greater at the top than elsewhere for cores 1U, 1D, 3D, 4D, 5U, and 5D. The mixed component fraction is at or near 0.2 for these cores and peaks between 4 mm and 8 mm, after which, it decreases. Clogging is the primary cause of the elevated mixed component near the top. Plots 1, 3, and 5 were known to be clogged with infiltration rates of 13.8, 3.7, and 1.6 mm/min, respectively. Plot 4 was not clogged, but the infiltration rate had decreased from 1810 mm/min at instillation to 1120 mm/min. There is an additional increase of the mixed component fraction near the 50 mm of 1U, 3U, 3D, 4U, 4D, and 5U. This is assumed to be caused by CT image artifacts near the edges of scans. Mixed component fraction peaks near the middle of the cores are not as great as the peaks near the surface, except for 4U, which was not clogged. Additionally, there is an increase in mixed components near the bottom of some of the cores. This is also assumed to be the result of image artifacts produced by the x-ray process.

The predominate factor influencing mixed component changes with depth are clogging and CT image reconstruct artifacts. Factors that were not considered that may influence the mixed component quantity and relationship to clogging include the density of clogging material, the bulk density of clogged regions, and the individual size clogging particles. The test plots from which the cores were collected were cleaned and the particles collected during hand vacuuming were collected and quantified. Results from cleaning are in chapter IV. Clogging particles collected during vacuuming range from 10 to 4000 μm. The voxel size used for reconstruction was 60.15 μm. Some of the clogging material occupies entire voxels and therefore classified as cementitious material rather than mixed material. Additionally, clogging material that is tightly packed into the pore can be classified as cementitious material. Denser clogged regions may have influenced the low mixed component fractions near the top of 3U and 5D. These locations were completed clogged based on infiltration rates measurement prior to cutting cores. The location

from which these cores were collected may have experienced repeated vehicle traffic that would cause higher bulk densities in these cores.

Trends between component fractions and pervious concrete mix design and field measured performance

Pervious concrete is typically made from three basic material classifications: water, cement paste, and aggregate. The proportions of these materials define the mix design and have an influence on the internal structure. Mix design proportions reported as ratios between common materials are plotted against void content (figure 5.10). Linear regression trend lines are included. Void content is the average for the core. Mix design data is on a plot bases, therefore, each set of plotted points has only three unique points values for mix design. This occurs because there are two cores per plot.

Cores with higher void content had lower fresh unit weight. This trend was expected as Kevern et al. (2008) presented similar findings. Trends with other PC mix design parameters were less pronounced or completely lacking. Sand content (sand:(sand+aggregate)) does not trend with void content. This is occurring because the sand in the mixes tested is a small portion compared to the crush rock aggregate quantity. Sand content may influence the size of the voids but does not affect the content of the voids in the tested cores. The total aggregate content, which is the combination of sand and crushed rock aggregate, trend with void content is slightly positive and has a weak relationship (R^2=0.17). This weak relationship is caused in part by the limited number of data points and small range of aggregate ratios. The reported aggregate ratios range from 3.52 to 4.52. Cores with increased voids where those with higher aggregate to cement paste ratio (figure 5.10). The relationship would vary if the aggregate size between PC mix design varied. Reported mean aggregate sizes were the same for all cores.

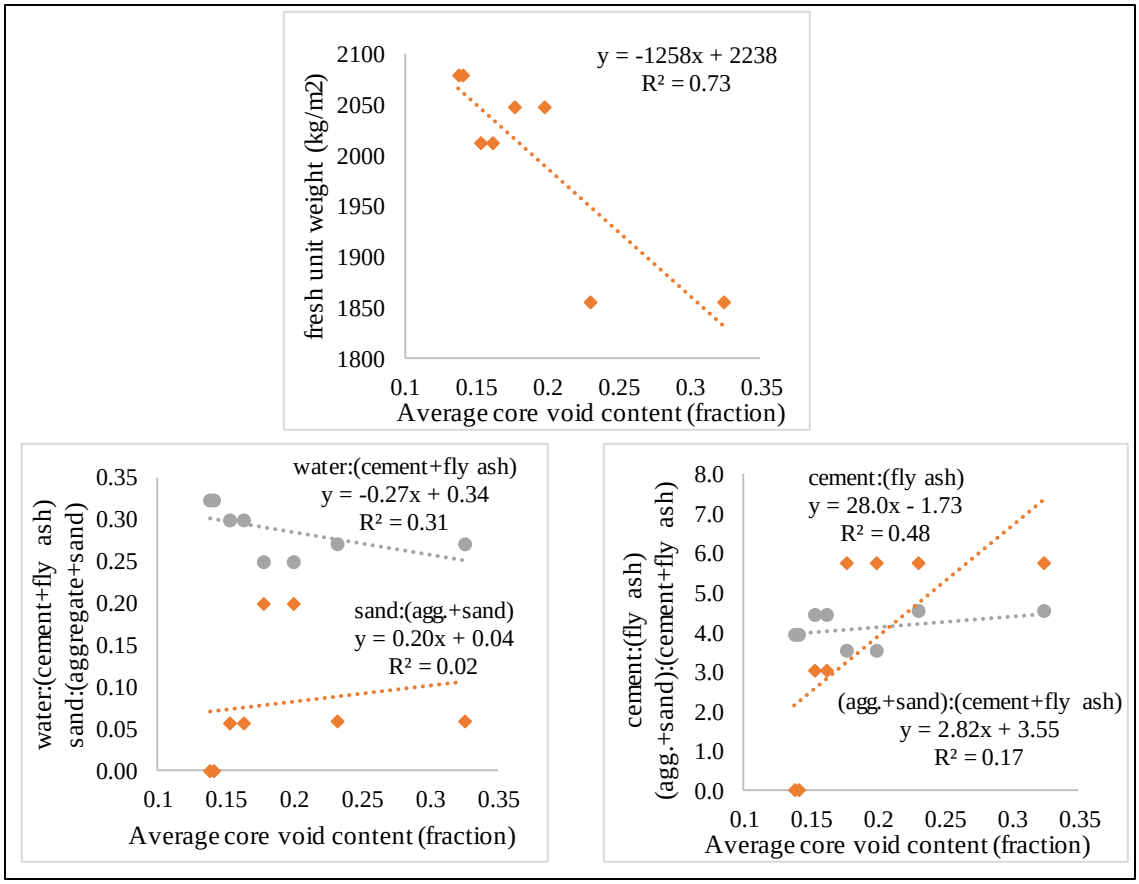

Figure 5.10. Top: plot of average Hsieh et al. (1998) void content of the entire core and fresh unit weight from chapter 4. Bottom left: plot of average Hsieh void content of the entire core and water:(cement_fly ash) ratio and sand:(agg.+sand) ratio. Bottom right: plot of average Hsieh void content of the entire core and cement:(fly ash) ratio and (agg.+sand):(cement_fly ash) ratio. Agg. stands for aggregate.

Void content and cementitious material determined with Hsieh methodology are not directly linked as the complement of each other as they are with a binary segmentation process. Trends between solid content and PC mix design along with mixed content and PC mix design were analyzed in addition to voids. Analysis of cementitious content and mixed content did not result in unique trends between PC mix design parameters that void content did not provide. Pearson's correlation coefficient between content fractions and PC mix design parameters are listed in table 5.3 to illustrate the similarities. The correlations of PC mix design to cementitious material content have similar magnitude but opposite sign of correlations with void content. This occurs

because the cementitious material is the near complement of void content. Mix content was not strongly correlated PC mix design parameters. There was a moderate correlation between the mixed fraction of the top 10 mm and % recover to phase 2 infiltration rates. This indicates that plots with more clogging were not cleaned as well as plots with less clogging. Core average voids was also moderately related to % recover to phase 2 infiltration rates. This is expected because PC with more pore space will maintain unobstructed pores even if some pores clog compared to PC with low void content. Linear regression relationships to % recover to phase 2 infiltration rates are shown in figure 5.11.

Table 5.4. Pearson's correlation coefficients between the average Hsieh void, mixed, and cementitious (solid) material component fraction of each core and the top 10 mm of each core and field measured parameters and mix design. Green values have a strong positive correlation (>0.75) and red values have a strong negative correlation (<-0.75).

	Core average voids (fraction)	*Top 10 mm voids (fraction)*	*Core average cemt. (fraction)*	*Top 10 mm avg. cemt. (fraction)*	*Core average mixed (fraction)*	*Top 10 mm mixed (fraction)*
S:(A+S)	0.16	0.23	-0.19	-0.24	0.05	-0.02
W:(C+FA)	-0.56	-0.64	0.57	0.59	0.09	0.16
C:FA	0.69	0.78	-0.73	-0.77	-0.06	-0.11
(A+S)/(C+FA)	0.41	0.41	-0.49	-0.54	0.09	0.18
Fresh Unit Weight (kg/m^3)	-0.86	-0.89	0.86	0.84	0.18	0.18
Initial infiltration rate (mm/min)	0.88	0.90	-0.84	-0.79	-0.28	-0.30
Initial clogging duration (days)	0.33	0.29	-0.12	0.07	-0.56	-0.68
Phase 2 avg. inf. rate (mm/min)	0.88	0.91	-0.85	-0.80	-0.27	-0.29
Phase 2 duration (days)	0.61	0.62	-0.66	-0.68	-0.02	0.03
% recovery to phase 2 inf. rate	0.64	0.45	-0.14	0.03	-0.38	-0.51

S – sand, A – aggregate, W – water, C – cement, FA – fly ash
inf. – infiltration, avg. – average, cemt. – cementitious

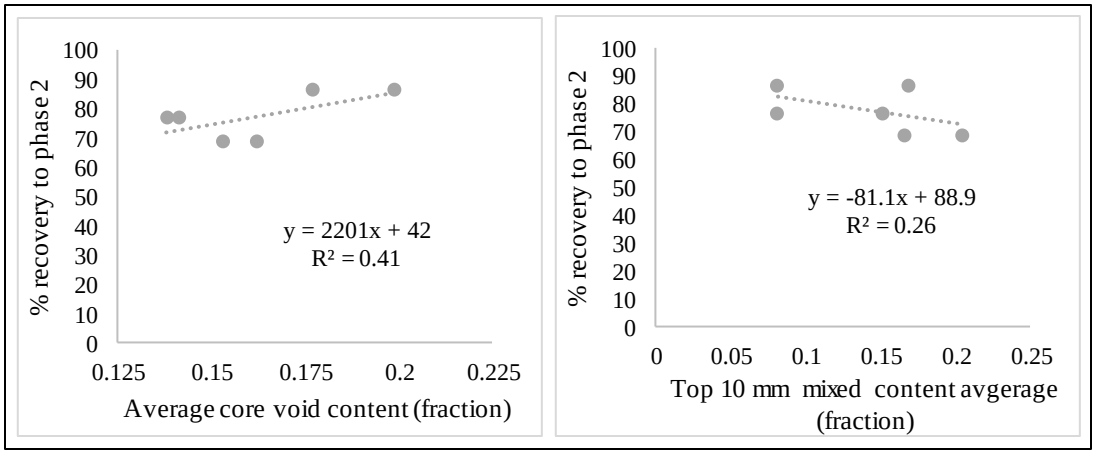

Figure 5.11. Left: plot of average Hsieh et al. (1998) void content of the entire core and % percent recovery of the phase 2 infiltration rate after Vactor truck cleaning from chapter 4. Right: plot of average Hsieh mixed component content for the top 10 mm of the cores and % percent recovery of the phase 2 infiltration rate after Vactor truck cleaning from chapter 4. Pervious concrete test plot 4 is not included because it was not cleaned with the Vactor truck

Average core void content is positively related to the initial and phase 2 average infiltration rates (figure 5.12). This is a logical relationship because PC with more voids has the potential to pass more water per area of PC. However, the quantity of voids through segmentation does not directly indicate that the voids provide a continuous path from the top to the bottom. Further analysis of spatial connectivity of the pores may improve the relationship between void content and infiltration rate performance. Regardless of the connectivity of the pores, there is a strong correlation between voids and the initial infiltration rate and infiltration rate as the PC clogged.

Duration of the phase 2 was greater for cores with greater void content (figure 5.12). A linear regression fit explains only 37% of the variability, but the correlation coefficient is moderate at 0.61. This relationship is similar to that of the infiltration rate in that more voids provides more opportunity for infiltration rate regards of the size. It is expected that PC with greater voids will continue to have open pores even as some clog. The size and shape of the pores will determine the size of particles that will clog the pores. An initial attempt to characterize the pore size of the PC cores is provided in appendix A6.

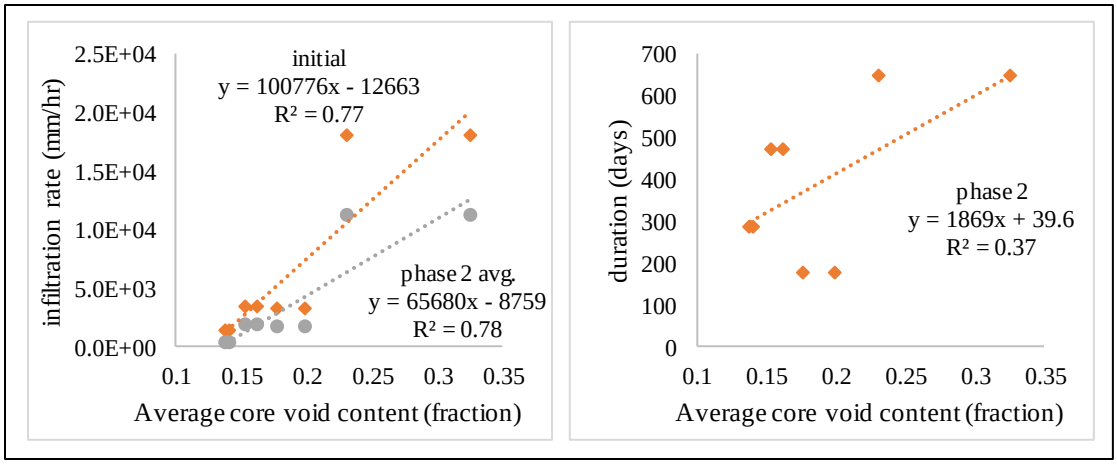

Figure 5.12. Left: plot of average Hsieh et al. (1998) void content of the entire core and the initial and phase 2 average infiltration rate from chapter 4. Right: plot of average Hsieh void content of the entire core and phase 2 duration from chapter 4.

CONCLUSIONS

Utilizing known information about the components within PC and photon statistics of x-ray CT proved to be a valid and useful method to quantify porosity. Content classification and quantification with Hsieh's method more accurately rejected regions of high-density heterogeneity that appear to be clogged regions compared to Otsu's threshold and segmentation. Fraction of cement paste and aggregate could not be properly identified with Hsieh's method because of image artifacts associated with x-ray CT and the similarity between the densities of the two materials. Void fraction increased with depth for most cores.

Analysis was completed on cores that were known to have clogged pores based on reduced infiltration rates, making the results presented here more applicable to aged PC that has been subjected to stormwater runoff. Analyzing PC with clogging may be more useful for long-term planning and modeling of PC because PC exposed to stormwater does not maintain its initial condition for an indefinite period.

Clogging was more prevalent in the top 10 mm of the cores based on increased mixed component fraction in this region. However, no definitive process is evident to isolate only clogging material.

Density similarities between clogging material and cementitious material and mixed voxel that occur at the edges of void and cementitious material influence the quantity of the mixed component fraction.

Component fraction averages for the cores were related to many of the PC mix design ratios and field performance infiltration rate and cleaning performance. In general, cores with less void content had mix designs with more cementitious material and lower infiltration rates. Cleaning performance was negatively related to the mixed component content fraction of the top 10 mm of the cores. This further indicates the link between mixed component and clogging. Correlations in the study are based on a limited dataset; eight data points for length and void correlations, four data points for mix design and long-term performance parameters, and three data points for phase 3 regression slope and cleaning performance.

ACKNOWLEDGEMENTS

The authors thank the City of Tulsa Stormwater Quality, the City of Tulsa Low Impact Development Working Group, and the Oklahoma State University Experiment Station. Additionally, the authors thank the companies that donated pervious concrete for the tests plots.

REFERENCES

Ahn, J., Jung, J., Kim, S., and Han, S. (2014). "X-Ray Image Analysis of Porosity of Pervious." *International Journal of GEOMATE,* 6(1), 796–799.

Brown, G. O., Stone, M. L., and Gazin, J. E. (1993). "Accuracy of gamma ray computerized tomography in porous media." *Water Resources Research*, 29(2), 479–486.

Deo, O., Sumanasooriya, M., and Neithalath, N. (2010). "Permeability Reduction in Pervious Concretes due to Clogging: Experiments and Modeling." *Journal of Materials in Civil Engineering*, 22(7), 741–751.

Ferguson, B. K. (2005). *Porous pavements*. Taylor & Francis.

Haselbach, L. M., and Freeman, R. M. (2006). "Vertical Porosity Distributions in Pervious Concrete Pavement." *ACI Materials Journal*, 103(6), 452–458.

Hsieh, H. T., Brown, G. O., Stone, M. L., and Lucero, D. A. (1998). "Measurement of porous media component content and heterogeneity using gamma ray tomography." *Water Resources Research*, 34(3), 365–372.

Iassonov, P., Gebrenegus, T., and Tuller, M. (2009). "Segmentation of X-ray computed tomography images of porous materials: A crucial step for characterization and quantitative analysis of pore structures." *Water Resources Research*, 45(9), 1–12.

Kayhanian, M., Anderson, D., Harvey, J. T., Jones, D., and Muhunthan, B. (2012). "Permeability measurement and scan imaging to assess clogging of pervious concrete pavements in parking lots." *Journal of Environmental Management*, Elsevier Ltd, 95(1), 114–123.

Kevern, J. T., Schaefer, V. R., Wang, K., and Suleiman, M. T. (2008). "Pervious Concrete Mixture Proportions for Improved Freeze-Thaw Durability." *Journal of ASTM International*, 5(2), 101320.

Kuang, X., Sansalone, J., Ying, G., and Ranieri, V. (2011). "Pore-structure models of hydraulic conductivity for permeable pavement." *Journal of Hydrology*, Elsevier B.V., 399(3–4), 148–157.

Kuang, X., Ying, G., Ranieri, V., and Sansalone, J. (2015). "Examination of Pervious Pavement Pore Parameters with X-Ray Tomography." *Journal of Environmental Engineering*, 141(10), 1–13.

Manahiloh, K. N., Muhunthan, B., Kayhanian, M., and Gebremariam, S. Y. (2012). "X-Ray Computed Tomography and Nondestructive Evaluation of Clogging in Porous Concrete Field Samples." *Journal of Materials in Civil Engineering*, 24(8), 1103–1109.

Meulenyzer, S., Stora, E., and Perez, F. (2012). "Impact of Pervious Concrete Porosity on Permeability by 3D Image Analysis." *Pervious Concrete*, ASTM International, 100 Barr Harbor Drive, PO Box C700, West Conshohocken, PA 19428-2959, 1–25.

Neithalath, N., Bentz, D., and Sumanasoorlya, M. (2010). "Predicting the Permeability of Pervious Concrete: Advances in Characterization of Pore Structure and Transport Properties." *Concrete International*, 32(5), 35–40.

Neithalath, N., Weiss, J., and Olek, J. (2006). "Characterizing Enhanced Porosity Concrete using electrical impedance to predict acoustic and hydraulic performance." *Cement and Concrete Research*, 36(11), 2074–2085.

Orsi, T. H., Edwards, C. M., and Anderson, A. L. (1994). "X-ray computed tomography; a nondestructive method for quantitative analysis of sediment cores." *Journal of Sedimentary Research*, 64(3a).

Otsu, N. (1979). "A Threshold Selection Method from Gray-Level Histograms." *IEEE Transactions on Systems, Man and Cybernetics*, 9(1).

Permeable Pavements Task Committee. (2015). *Permeable pavements*. (B. Eisenberg, K. C. Lindow, and D. R. Smith, eds.), American Society of Civil Engineers.

Petrovic, A. M., Siebert, J. E., and Rieke, P. E. (1982). "Soil Bulk Density Analysis in Three Dimensions by Computed Tomographic Scanning1." *Soil Science Society of America Journal*, Soil Science Society of America, 46(3), 445.

Radlińska, A., Welker, A., Greising, K., Campbell, B., and Littlewood, D. (2012). "Long-Term Field Performance of Pervious Concrete Pavement." *Advances in Civil Engineering*, 2012(Figure 1), 1–9.

Rehder, B., Banh, K., and Neithalath, N. (2014). "Fracture behavior of pervious concretes: The effects of pore structure and fibers." *Engineering Fracture Mechanics*, Elsevier Ltd, 118, 1–16.

Sansalone, J., Kuang, X., and Ranieri, V. (2008). "Permeable Pavement as a Hydraulic and Filtration Interface for Urban Drainage." *Journal of Irrigation and Drainage Engineering*, 134(5), 666–674.

Schaefer, V., Wang, K., Suleiman, M., and Kevern, J. (2006). "Mix design development for pervious concrete in cold weather climates." *Center for Transportation Research and Education, Iowa State University*, (February), 67.

Sumanasooriya, M. S., Bentz, D. P., and Neithalath, N. (2010). "Planar image-based reconstruction of pervious concrete pore structure and permeability prediction." *ACI Materials Journal*, 107(4), 413–421.

Sumanasooriya, M. S., and Neithalath, N. (2009). "Stereology- and morphology-based pore structure descriptors of enhanced porosity (Pervious) concretes." *ACI Materials Journal*, 106(5), 429–438.

Teng, Z., and Sansalone, J. (2004). "In situ partial exfiltration of rainfall runoff. II: Particle separation." *Journal of Environmental Engineering*, 130(9), 1008–1020.

The Mathworks Inc. (2016). "MATLAB - MathWorks." *www.mathworks.com/products/matlab*, <http://www.mathworks.com/products/matlab/>.

Vancura, M. E., MacDonald, K., and Khazanovich, L. (2012). "Location and Depth of Pervious Concrete Clogging Material before and after Void Maintenance with Common Municipal Utility Vehicles." *Journal of Transportation Engineering*, 138(3), 332–338.

Wildenschild, D., and Sheppard, A. P. (2013). "X-ray imaging and analysis techniques for quantifying pore-scale structure and processes in subsurface porous medium systems." *Advances in Water Resources*, Elsevier Ltd, 51, 217–246.

Zhong, R., and Wille, K. (2016). "Linking pore system characteristics to the compressive behavior of pervious concrete." *Cement and Concrete Composites*, Elsevier Ltd, 70, 130–138.

CHAPTER VI

CONCLUSION

MAJOR FINDINGS

Three different research projects were completed to assess aged bioretention cells (BRCs) and pervious concrete (PC). The first project, chapter III, focused on two 8-year old BRCs. Both BRCs were flood tested 1-year after construction and discussed in Christianson et al. (2012). Similar flooding tests were completed and compared to the 1-year after results to determine changes in performance. Additionally, water samples were collected from the inlet, overflow, and underdrain and analyzed for *E. coli*, enterococci, nitrate, pH, turbidity, ortho-phosphate, chloride, electrical conductivity, and pH. The major findings from chapter III are:

1. Aged BRCs constructed with fly ash amended filter media maintained sufficient storage and drawdown rates to meet design standards.
2. Change in BRC drawdown rate after 8-years varied. One of the BRC exhibited no measurable change, while the other decreased by 65 %.
3. A short antecedent dry period resulted in decreased volume reduction but similar peak flow mitigation. Additionally, antecedent dry period impacted pollutant leaching. *E. coli*, enterococci, EC, NO3-N, pH, and turbidity levels from underdrain samples were significantly lower.

4. *E. coli* and enterococci leached from both aged BRCs when flushed with treated municipal water.

The second project, chapter IV, was the assessment of infiltration rate of five pervious concrete tests plots over a 2.5-year period. Each of the plots was constructed from a different mix but installed by the same company. The test plots were installed on a slope, received stormwater runoff from an upslope impervious asphalt surface, and each was approximately the size of two parking stalls. In addition to monitoring infiltration rates, cleaning methods evaluated on clogged pervious concrete and correlations were development between long-term infiltration rate trends, cleaning performance, and mix design. Major findings from chapter IV are:

1. The infiltration rate of PC on a slope that received stormwater runoff from an upslope impervious surface underwent three phases as it aged. The infiltration rate phases were: 1) initial decrease, 2) steady period, and 3) secondary decrease.
2. The average combined duration of phases 1 and 2 was 650 days.
3. Combining spraying water and vacuuming with a Vactor truck restored infiltration rates to near phase 2 levels.
4. Mixes with higher sand content experienced improved cleaning performance.

The third study, chapter V, was the assessment and quantification of voids, clogging, and cementitious material content of PC cores with x-ray computer tomography methods. A frequency distribution fitting segmentation method developed by Hsieh et al. (1998) was evaluated to quantify multiple components within clogged PC. Segmentation results were compared to the commonly used Otsu (1979) gray level segmentation method. PC mix design and field measured performance measurements were compared to segmentation results. The major findings from chapter V are:

1. Multiple component segmentation is a valid method for quantification of clogged PC because it identifies void space, areas of high heterogeneity (which can be caused by clogging), and cementitious material.
2. Segmenting x-ray images of PC with Hsieh et al. (1998) frequency distribution fitting methodology resulted in an average of 5% less porosity than with the common Otsu (1979) methodology because it more accurately rejected regions of clogging material.
3. Infiltration based performance measures and PC mix design were strongly correlated to void content. PC with higher fresh unit weight had less voids. Plots that were most efficiently cleaned had less mixed component voxels (an indication of clogging) in the top 10 mm of the analyzed cores.

BROADER IMPACTS

Scientific community

The results here add to the existing body of long-term performance studies related to LID, but overall, this field of research is still lacking. Performance of the two tested BRC varied. The possible influence of a shallow water table, roll of vegetation, and influence of animals on the long-term performance of BRCs need further investigation. Flooding tests proved to be a viable testing method and should be considered for future assessments of infiltration based LID practices. Four out of five pervious concrete mixes that were studied clogged during the 2.5-year period. The clogging rate was influenced by mix design but was ultimately caused by washed on sediments. The impact of source control on pervious concrete and other LID practices is lacking.

The results from all three studies are all related to the specific design of the LID practices that were tested. The BRC exhibited short-circuiting of inflow to the underdrain. Additional research is needed to develop designs that increase the flow path, both through the filter media and in the ponded area. The results indicated that exfiltration was a major component of the water balance of the tested BRCs. Designs that encourage exfiltration while ensuring complete drawdown of the

storage water in the filter media are needed. Designs that utilize multi-stage underdrain outlets, similar to stormwater detention pond outlet risers, could be developed and researched. Related to pervious concrete, there exists opportunities to evaluate different mix design that may improve filter performance while improving cleaning efficiency. Sand content is a potential mix component that could be further investigated as it was found to be correlated to many performance parameters.

Chapter V utilized computer tomography methods from other fields of research to evaluate PC. The results are an example of how the research of other porous medias can be applied to pervious concrete to investigate clogging. The frequency distribution fitting component content method developed by Hsieh et al. (1998) has limited application in the literature, but proved to be a useful approach to quantify PC.

Practicing professionals

LID is now a common, and often preferred, stormwater management technique. The results from this dissertation can benefit the professional stormwater community. The tested BRC performed at or near design specifications. Design features that may have contributed to the long-term performance include the addition of sand plugs through growth media, amendment of fly ash at 5% by weight, and inclusion of an underdrain with multiple laterals. These design features should be considered for future BRCs. However, modified underdrain configurations should be considered if increased exfiltration or increased discharge times are wanted.

Maintenance proved to be a necessity for the tested pervious concrete. Yearly preventive cleaning and inspection for clogging is recommended for all types of permeable pavement. Any upslope impervious surface should also be cleaned in addition to cleaning the pervious concrete. This type of cleaning schedule could prevent the need for time-intensive restorative cleaning and ensure long-term success of pervious concrete. Furthermore, source control of sediments near pervious

concrete is highly recommend. Once clogged, restorative cleaning is needed. The simultaneous use of spraying water and vacuuming should be considered.

REFERENCES

Christianson, R. D., Brown, G. O., Chavez, R. A., and Storm, D. E. (2012). "Modeling Field-Scale Bioretention Cells with Heterogeneous Infiltration Media." *Transactions of the ASABE*, 55(4), 1193–1201.

Hsieh, H. T., Brown, G. O., Stone, M. L., and Lucero, D. A. (1998). "Measurement of porous media component content and heterogeneity using gamma ray tomography." *Water Resources Research*, 34(3), 365–372.

Otsu, N. (1979). "A Threshold Selection Method from Gray-Level Histograms." *IEEE Transactions on Systems, Man and Cybernetics*, 9(1).

APPENDIX A

APPENDIX A1 – PEARSON'S CORRELATION TABLE OF LONG-TERM CLOGGING PARAMETERS, MIX DESIGN, AND CLEANING PERFORMANCE.

	Initial infiltration rate (cm/min)	*Phase 1 clogging duration (days)*	*Phase 1 clogging regression slope (cm/min/day)*	*Phase 2 average infiltration rate (cm/min)*	*Phase 2 duration (days)*	*Phase 2 regression slope (cm/min/day)*	*Phase 3 regression slope (cm/min/day)*	*S:(A+S)*	*W:(C+FA)*	*C:FA*	*(A+S)/(C+FA)*	*Fresh Unit Weight (kg/m^3)*	*Vactor cleaning inf. rate recovery (% of phase 2 average inf. rate)*
Initial infiltration rate (cm/min)	1.00												
Phase 1 clogging duration (days)	0.00	1.00											
Phase 1 clogging regression slope (cm/min/day)	-0.97	0.00	1.00										
Phase 2 average infiltration rate (cm/min)	1.00	-0.05	-0.94	1.00									
Phase 2 duration (days)	0.83	-0.45	-0.82	0.84	1.00								
Phase 2 regression slope (cm/min/day)	-0.08	0.46	-0.13	-0.16	-0.07	1.00							
Phase 3 regression slope (cm/min)	-0.97	0.72	0.65	-0.98	-0.76	0.88	1.00						
S:(A+S)	-0.10	0.27	0.12	-0.10	-0.50	-0.25	0.23	1.00					
W:(C+FA)	-0.36	-0.35	0.34	-0.36	0.10	0.16	-0.10	-0.89	1.00				
C:FA	0.60	0.07	-0.54	0.61	0.26	-0.31	-0.29	0.70	-0.92	1.00			
(A+S)/(C+FA)	0.64	-0.39	-0.74	0.63	0.92	0.35	-0.34	-0.59	0.24	0.06	1.00		
Fresh Unit Weight (kg/m^3)	-0.98	0.07	0.94	-0.99	-0.89	0.04	0.92	0.13	0.32	-0.61	-0.72	1.00	
Vactor cleaning inf. rate recovery (% of phase 2 average inf. rate)	-0.87	0.81	0.68	-0.87	-0.92	0.61	0.93	0.53	-0.42	0.01	-0.63	0.88	1.00

APPENDIX A2 – HSIEH ET AL. (1998) FREQUENCY DISTRIBUTION FITTING

MATLAB CODE

```
%function [] = histFitStackFun_V3()
%% Set working folder
tic
% set working folder
mainFolderName = 'C:\Users\ajmclem\Desktop\PC xray
temp\beamHardCorCombined\';
subFolderName = '5D\';
folderName = sprintf('%1$s%2$s',mainFolderName,subFolderName);
imageSetID = '5D';
coreNum = 8;

%% Define voxel size
voxelSize = 60.154114; % (um)

%% Image intensity information
% these values were manually determined by average the attenuation
values
% of a known region with in the center slice of each stack. Where the
% stacks are split into each scan (i.e. top and bottom of a single
core)
% Order: 1UT, 1UB,  1DT,  1DB,  3UT,  3UB,  3DT,  3DB,  4UT,  4UB,
4DT,  4DB,  5UT,  5UB,  5DT,  5DB
att1 = [11310,11300;10100,12097;12350,10500;6300, 10800; 6000,10100;
4300,11700;11200,12000; 7100, 4500];
att2 = [21400,22400;18700,24000;25250,21250;11800,22800;12700,22500;
9100,22000;18900,21200;11400, 8400];
att3 =
[24500,25700;22400,28700;29650,25300;14150,26700;15100,26250;10500,2730
0;24100,27200;14800,10900];

% image number of the last image in the top image stack
% need to apply the correct density adjustment
%                1U   1D   3U   3D   4U   4D   5U   5D
topLastImage = [829, 816, 816, 787, 850, 816, 816, 816];

% densities; paste density is defined inside loop
rho1 = 1.15; % density of air
rho3 = 2500; % density of aggregate

%% Load image stack

% Number of images
D = dir([folderName, '\*.tif']);
numIm = length(D(not([D.isdir])));

%% Preallocate variables
% laod images into a 3D matrix (i.e. stack)
%imHistograms = nan(65536, numIm);
solution = nan(numIm, 12);

%% solver stuff not needed in the loop
```

```
% other constraints
% R1+R2+R3+Rm = 1
% the sum of the product Aeq*x = beq
% Ae1 --> muMixed, R1, R2, R3, Rm, a,  b,  stdM
Aeq = [0, 1, 1, 1, 1, 0, 0, 0];
beq = 1;
% no linear inequalities
%A = []; bs = [];
A = [0, 0, 0, 0, 0, -1, 1, 0]; bs = 0;

% solver
nonlcon = [];
options = optimset('Display', 'off');

%% solver loops through images
parfor i = 1:numIm
    %%
    if i <= topLastImage(coreNum)
        location = 1; % top of core
    else
        location = 2; % bottom of core
    end

    %% get image
    fileName = sprintf('%1$s%2$04d.tif',folderName,i);
    im=imread(fileName);
    imSize = size(im);
    imHeight = imSize(1); % [pixels] in x-axis
    imWidth = imSize(2); % [pixels] in y-axis

    %% Crop
    % cropping width and height
    cDiaMm = 40; % diameter of crop [mm]
    % cropping parameters
    cRad = round(cDiaMm/2/voxelSize*1000); % radius of crop [pixels]
    ci = [round(imHeight/2),round(imWidth/2)]; % center [pixels]
([c_row, c_col, r])
    cRangeX = ((ci(1)-cRad):(ci(1)+cRad)); % pixel range to crop to
    cRangeY = ((ci(2)-cRad):(ci(2)+cRad)); % pixel range to crop to
    imCropSq = im(cRangeX,cRangeY); % crop
    numObs = length(imCropSq)*length(imCropSq);
    % view image
    %{
    f2 = figure;
    imshow(imCropSq)
    title('cropped image')
    %}

    %% Convert hist x-axis to density

    imDen = double(imCropSq)-att1(coreNum,location);
    imDen = imDen.*(rho3/(att3(coreNum,location)-
att1(coreNum,location)));
    imDenSize = size(imDen);
    imDen = reshape(imDen,[imDenSize(1)*imDenSize(2),1]);
    [hisIm,den] = hist(imDen,1000);
```

```
    hisIm = hisIm./sum(hisIm); % converte to PDF
    %figure; plot(den,hisIm)

    %% Fitting minimization

    % known input variables: x, hisIm, Q1_loc, Q2_loc
    % set means, i.e. location of pure components
    mu1 = rho1;
    mu3 = rho3;
    mu2 = rho3*(att2(coreNum,location)/att3(coreNum,location)); %
density of cement paste

    % first guess of unknowns
    muM = (mu1+mu3)/2; % mean density of peaks, start at midway between
mu1 and mu2

    %%
    if i <= topLastImage(coreNum)
        sig_0 = 266;% abs(den(2)-den(1))*1200;
    else
        sig_0 = 265;% abs(den(2)-den(1))*1200;
    end

    %     muMixed,     R1,   R2,   R3, Rm,  a,   b,    sigma   %
variables to solve
    x0 = [muM,         0,    0,    0,  0,   6,   2,    sig_0]; % first
guess
    lb = [mu1+4*sig_0, 0,    0,    0,  0,   1.1, 1.01, 150]; % lower
bound
    ub = [mu2-3*sig_0, 0.75, 0.75, 1,  0.5, 5,   5,    265]; % upper
bound

    %%
    % define function to minimize
    % solver variables, x
    % passing extra variables through
    fun = @(x)minimizeFun(x, den, hisIm, mu1, mu2, mu3, numObs);

    % solver
    [x,fval,~,~] = fmincon(fun,x0,A,bs,Aeq,beq,lb,ub,nonlcon,options);

    % store results
    %imHistograms(:,i) = hisIm;
    solution(i,:) = [mu1, mu2, mu3, x, 1-fval];

end

%% stop timer
dt = toc/60;
sprintf('Code ran for %1$s mins',dt)

%% check out the results
%
figure
plot(solution(:,5:8))
```

```
xlabel('depth (as image num)')
ylabel('content as fraction')
grid on
legend('voids','paste','solids','mixed') % create legend

figure;
depth = (voxelSize:voxelSize:voxelSize*numIm)./1000;
plot(depth,solution(:,5))
hold on
plot(depth,solution(:,6)+solution(:,7));
plot(depth,solution(:,8))
hold off
xlabel('depth (mm)')
ylabel('content as fraction')
grid on
legend('voids','cementitious material','mixed') % create legend

figure;
plot(depth,solution(:,6),depth,solution(:,7));
xlabel('depth (mm)')
ylabel('content as fraction')
legend('cement paste','aggregate')
%print(imageSetID,'-dpng')
%}
%% Look at solution

% split out solver variables
mu1, mu2, mu3
muM = x(1)
R1 = x(2)
R2 = x(3)
R3 = x(4)
Rm = x(5)
a = x(6)
b = x(7)
sig = x(8)

% get fit curve
[f, f1, f2, f3, fm, R_sqr, Xc] = HsiehHistFitting(...
    den, hisIm, mu1, mu2, mu3, muM,...
    R1, R2, R3, Rm, a, b, sig, numObs);

% Chi-squre fit
R_sqr
Xc

%% plot
figure(1);
subplot(2,2,1)
imshow(imCropSq)
title('image')

subplot(2,2,2)
plot(den,f1,den,f2,den,f3,den,fm)
title('density distributions of components')
```

```
ylabel('probability')
grid on
legend('voids','paste','agg','mixed') % create legend

subplot(2,2,3)
plot(den,hisIm,'.',den,f)
ylabel('probability')
grid on
legend('image histogram','fitted histogram') % create legend

subplot(2,2,4)
plot(den,hisIm,'.',den,f1,den,f2,den,f3,den,fm)
ylabel('probability')
grid on
legend('image histogram','voids','paste','agg','mixed') % create legend


% save all variables as a Matlab file
% dataName = 'histogramFit';
% filename = sprintf('%1$s_%2$s.mat',imageSetID,dataName);
% save(filename,'-v7.3')


%% Histogram
histScal = 10;
[hisIm2,bins] = imhist(imCropSq,65536);
hisIm2(end)=0; %remove white (65536) background
hisIm2(1)=0; %remove black (1) background
hisIm2 = hisIm2./sum(hisIm2); % converte to PDF

%binsAdj = bins-att1(coreNum,location);%+rhoP1; % shift axis down to
the density of air
%den = binsAdj.*(rho3/(att3(coreNum,location)-att1(coreNum,location)));
%{
    f3 = figure;
    plot(bins,hisIm)
    title('image histogram')
%}

%% Segment and view

otusThresLevel = otsuthresh(hisIm2);
otusLocIdx = round(otusThresLevel*length(hisIm2));
binSize = (bins(2)-bins(1));
otusLocVal = otusLocIdx*binSize;

% Otsu
% pores
imOtsuPores = imCropSq;
imOtsuPores(imOtsuPores>otusLocVal) = 65536;
% solid
imOtsuSolid = imCropSq;
imOtsuSolid(imOtsuSolid<otusLocVal) = 0;

%% Hsieh
```

```
imDen = double(imCropSq)-att1(coreNum,location);
imDen = imDen.*(rho3/(att3(coreNum,location)-att1(coreNum,location)));

% pores
[~,p1] = max(f1);
[~,pm] = max(fm);
[~,intersection] = min(abs(f1(p1:pm)-fm(p1:pm)));
thresHsiehVoids = den(p1+intersection);
imHsiehPores = imCropSq;
imHsiehPores(imDen>thresHsiehVoids) = 65536;

% aggregate
[~,p2] = max(f2);
[~,p3] = max(f3);
[~,intersection] = min(abs(f3(p2:p3)-f2(p2:p3)));
thresHsiehSolid = den(p2+intersection);
imHsiehSolid = imCropSq;
imHsiehSolid(imDen<thresHsiehSolid) = 0;

% paste
[~,intersection] = min(abs(f3(pm:p2)-f2(pm:p2)));
thresHsiehPaste = den(pm+intersection);
imHsiehPaste = imCropSq;
imHsiehPaste(imDen<thresHsiehPaste) = 65536;
imHsiehPaste(imDen>thresHsiehSolid) = 65536;

% mixed
imHsiehMixed = imCropSq;
imHsiehMixed(imDen<thresHsiehVoids) = 65536;
imHsiehMixed(imDen>thresHsiehPaste) = 65536;

%% plot
figure(2)
subplot(3,3,1)
imshow(imCropSq); title('original')

subplot(3,3,2)
plot(den,hisIm,den,f)
ylabel('probability')
grid on
legend('image histogram','fitted histogram') % create legend

subplot(3,3,3)
plot(den,hisIm,den,f1,den,f2,den,f3,den,fm)
ylabel('probability')
grid on
legend('image histogram','voids','paste','agg','mixed') % create legend

subplot(3,3,4)
imshow(imOtsuPores); title('Otsu pores, with white background')

subplot(3,3,7)
imshow(imOtsuSolid); title('Otsu solid, with black background')
```

```
subplot(3,3,5)
imshow(imHsiehPores); title('Hsieh pores, with white background')

subplot(3,3,8)
imshow(imHsiehSolid); title('Hsieh solid, with black background')

subplot(3,3,6)
imshow(imHsiehMixed); title('Hsieh mixed, with white background')

subplot(3,3,9)
imshow(imHsiehPaste); title('Hsieh paste, with white background')
%}

%% save all variables as a Matlab file
%{
dataName = 'histogramFit';
filename = sprintf('%1$s_%2$s.mat',imageSetID,dataName);
save(filename,'-v7.3')
%}
```

```
function [fminValue] = fmincon(...
    x, den, hisIm, mu1, mu2, mu3, numObs)
% split out solver variables
muM = x(1);
R1 = x(2);
R2 = x(3);
R3 = x(4);
Rm = x(5);
a = x(6);
b = x(7);
std = x(8);

[~, ~, ~, ~, ~, Rsq, ~] = HsiehHistFitting(...
    den, hisIm, mu1, mu2, mu3, muM,...
    R1, R2, R3, Rm, a, b, std, numObs);

fminValue = 1-Rsq;
```

```
function [f, f1, f2, f3, fm, R_sqr, Xc] = HsiehHistFitting(...
    den, hisIm, mu1, mu2, mu3, muM,...
    R1, R2, R3, Rm, a, b, sig, numObs)

% inputs %%%%%%%%%%%%%%%%%%%%%%%%%%%%%%%%
% x, histogram bins
% hisIm, image histogram
% mu1, pure component 1 peak
% mu2, pure component 2 peak
% mu3, pure component 3 peak
% muM, mixed component mean density
```

```
% R1, fraction of pure component 1
% R2, fraction of pure component 2
% R3, fraction of pure component 3
% Rm, fraction of mixed component
% a, beta-distribution alpha value
% b, beta-distribution beta value
% std, normal-distribution standard deviation

% outputs %%%%%%%%%%%%%%%%%%%%%%%%%%%%%%%
% f_pure, pure component density distribution
% f_mixed, mixed/partial voxel component density distribution
% f_comp,  pure and mixed/partial voxel component density distribution
% f, density distribution with photon statistics
% R_sqr, R-squard of a linear fit between f and hisIm
% Xc, chi-square fit between f and hisIm

%% Mixed and partial voxel compoenent

% fraction of mixed components
% Rm = 1-R1-R2-R3;
% mixed and partial voxel will be between the lowest and highest pure
% components. The range of this is based on the lcoation of peaks.
numPts = int16((mu2-mu1)/abs(den(2)-den(1)));
%xm_range = (mu1:step:mu2); % mix/partial voxel range
beta_range = linspace(0,1,numPts);
% distribution, assume a beta distribution works
Qm_betaPDF = betapdf(beta_range,a,b); % create PDF of a normal
distribution
Qm = Qm_betaPDF./sum(Qm_betaPDF);
%figure; plot(Qm_betaPDF); sum(Qm_betaPDF)

%% Photon statistical noise

% create Gaussian distribution
% according to Brown et al. 1993 (Accuracy of Gamma Ray Computerized
% Tomography in Porous Media), the standard deviation is equation to
the
% squre-root of mean of I
g_normPDF = normpdf(den,mu1,sig); % crate PDF of a normal distribution
g1_noise = g_normPDF./sum(g_normPDF);
g_normPDF = normpdf(den,mu2,sig); % crate PDF of a normal distribution
g2_noise = g_normPDF./sum(g_normPDF);
g_normPDF = normpdf(den,mu3,sig); % crate PDF of a normal distribution
g3_noise = g_normPDF./sum(g_normPDF);
g_normPDF = normpdf(den,muM,sig); % crate PDF of a normal distribution
gM_noise = g_normPDF./sum(g_normPDF);
%plot(den,g1_noise,den,g2_noise,den,g3_noise,den,gM_noise)

%% Convolution of component histogram with photon statistics

f1 = conv(g1_noise, R1, 'same');
f2 = conv(g2_noise, R2, 'same');
f3 = conv(g3_noise, R3, 'same');
fm = conv(gM_noise, (Qm*Rm), 'same');
f = f1+f2+f3+fm;
```

```
%% Fit quantification

% linear model
% mdl = fitlm(hisIm,f);
% R_sqr = mdl.Rsquared.Ordinary;
% R_sqr = true;
SSr = sum((hisIm.*numObs-f.*numObs).^2);
SSt = sum((hisIm.*numObs-mean(hisIm.*numObs)).^2);
R_sqr = 1 - SSr/SSt;


% Chi-square
% density histograms (i.e. range from 0 to 1) are convereted to
frequency
Xc= true;
% Xc_i = (((hisIm.*numObs)-(f.*numObs)).^2./(f.*numObs));
% Xc = sum(Xc_i(isfinite(Xc_i)));
```

APPENDIX A3 – OTSU (1979) SEGMENTATION POROSITY MATLAB CODE

```
%% set working folder
mainFolderName = 'C:\...';
subFolderName = '4Dc\';
folderName = sprintf('%1$s%2$s',mainFolderName,subFolderName);
imageSetID = '4D';

%% Get num of images in folder
% Number of images
D = dir([folderName, '\*.tif']);
numIm = length(D(not([D.isdir])));

%% pre-allocate loop variables
porosity = nan(numIm,1);

%% loop through the other images
for i = 0:numIm

    % open file
    fileName = sprintf('%1$s%2$04d.tif',folderName,i);
    im=imread(fileName);

    % Otsu's segmentation
    level = graythresh(im);
    BW = imbinarize(im,level); % simple Otsu segmentation
    BW = BW==0; %invert image
    imSize = size(BW);

    % Save porosity result
    porosity(i) = sum(sum(BW))/(imSize(1)*imSize(2));
end
```

APPENDIX A4 – SEMIVARIOGRAM MATLAB CODE

```
%% Setup

% set working folder
mainFolderName = 'C:\Users\ajmclem\Desktop\PC xray
temp\beamHardCorCombined\';
subFolderName = '3D\';
folderName = sprintf('%1$s%2$s',mainFolderName,subFolderName);
imageSetID = '3D';
coreNum = 4;

voxelSize = 60.154114; % (um)

%% Image intensity information
% these values were manually determined by average the attenuation
values
% of a known region with in the center slice of each stack. Where the
% stacks are split into each scan (i.e. top and bottom of a single
core)
% Order: 1UT,   1UB,   1DT,  1DB,   3UT,   3UB,     3DT,
3DB,4UT,4UB,4DT,4DB,5UT,5UB,5DT,5DB
att1 = [11310,11300;10100,12097;12350,10500;6300, 10800; 6000,10100;
4300,11700;11200,12000; 7100, 4500];
att2 = [21400,22400;18700,24000;25250,21250;11800,22800;12700,22500;
9100,22000;18900,21200;11400, 8400];
att3 =
[24500,25700;22400,28700;29650,25300;14150,26700;15100,26250;10500,2730
0;24100,27200;14800,10900];

% image number of the last image in the top image stack
% need to apply the correct density adjustment
%               1U   1D   3U   3D   4U   4D   5U   5D
topLastImage = [829, 816, 816, 787, 850, 816, 816, 816];

% densities; paste density is defined inside loop
rho1 = 1.15; % density of air
rho3 = 2500; % density of aggregate

%% Load image stack

% Number of images
D = dir([folderName, '\*.tif']);
numIm = length(D(not([D.isdir])));

%% Load image stack

% preallocate loop variables
% get sample image size
fileName = sprintf('%1$s%2$04d.tif',folderName,1);
imVec=imread(fileName);
imSize = size(imVec);
imHeight = imSize(1); % [pixels] in x-axis
imWidth = imSize(2); % [pixels] in y-axis
% crop image
```

```
cDiaMm = 40; % diameter of crop [mm]
cRad = round(cDiaMm/2/voxelSize*1000); % radius of crop [pixels]
ci = [round(imHeight/2),round(imWidth/2)]; % center [pixels] ([c_row,
c_col, r])
cRangeX = ((ci(1)-cRad):(ci(1)+cRad)); % pixel range to crop to
cRangeY = ((ci(2)-cRad):(ci(2)+cRad)); % pixel range to crop to
imCropSq = imVec(cRangeX,cRangeY); % crop
imSize = size(imCropSq);
% create density matrix
imDen = zeros(imSize(1),imSize(2),numIm);

%%
% loop through images and save into a single matrix as density
for i = 1:numIm

    % get sample image size
    fileName = sprintf('%1$s%2$04d.tif',folderName,i);
    imVec=imread(fileName);
    imSize = size(imVec);
    imHeight = imSize(1); % [pixels] in x-axis
    imWidth = imSize(2); % [pixels] in y-axis

    % crop image
    cDiaMm = 40; % diameter of crop [mm]
    cRad = round(cDiaMm/2/voxelSize*1000); % radius of crop [pixels]
    ci = [round(imHeight/2),round(imWidth/2)]; % center [pixels]
([c_row, c_col, r])
    cRangeX = ((ci(1)-cRad):(ci(1)+cRad)); % pixel range to crop to
    cRangeY = ((ci(2)-cRad):(ci(2)+cRad)); % pixel range to crop to
    imCropSq = imVec(cRangeX,cRangeY); % crop

    % convert to density
    %%
    if i <= topLastImage(coreNum)
        location = 1; % top of core
    else
        location = 2; % bottom of core
    end
    imDen_i = double(imCropSq)-att1(coreNum,location);
    imDen_i = imDen_i.*(rho3/(att3(coreNum,location)-
att1(coreNum,location)));

    imDen(:,:,i) = imDen_i;

end

clear imDen_i imVec D imCropSq

% get image dimensions
imSize = size(imDen);
imLngX = imSize(1);   % num of voxels in X-direction
imLngY = imSize(2);   % num of voxels in Y-direction
imLngZ = imSize(3);   % num of voxels in Z-direction
```

```
%% Compute directional semivariograms

% ~x-direction semivariogram~
% determine unique combination of pionts
points = int8(ones(imLngX,imLngX));
unqPoints = logical(triu(points));
[ii,jj] = (find(unqPoints)); % location of unique points
h_iijj = abs(ii-jj)*voxelSize; % distance vector

% define semivariogram distances count and vectors for loop
sumSqDiff = zeros(length(h_iijj),1);
N_h_iijj = imLngY*imLngZ;
N_h_iijj(1:length(h_iijj),1) = N_h_iijj;

% loop
parfor j = 1:imLngY % y-axis loop
    for k = 1:imLngZ % z-axis loop
        % get vector of voxels in direction being analyzed
        semVec = imDen(:,j,k); % converted to double precision
        % square difference between unique points
        sqDiff = (semVec(ii)-semVec(jj)).^2;
        sumSqDiff = sumSqDiff+sqDiff;
    end
end

hx = unique(h_iijj);
N_h = zeros(length(hx),1);
sumSqDiff_h = N_h;
for i = 1:length(hx)
    h_iijj_true = h_iijj==hx(i);
    N_h(i) = sum(N_h_iijj(h_iijj_true));
    sumSqDiff_h(i) = sum(sumSqDiff(h_iijj_true));
end
Xvariogram = 1./(2*N_h).*sumSqDiff_h; % semivariogram

% save data
% x semivariogram
SemVarTable = table(hx,Xvariogram,...
    'VariableNames',{'length__mm' 'Semivariance'});
dataName = 'xSemVar';
filename = sprintf('%1$s_%2$s.csv',imageSetID,dataName);
writetable(SemVarTable,filename)

% ~Y-direction semivariogram~
% determine unique combination of pionts
points = int8(ones(imLngY,imLngY));
unqPoints = logical(triu(points));
[ii,jj] = find(unqPoints); % location of unique points
h_iijj = abs(ii-jj)*voxelSize; % distance vector

% define semivariogram distances count and vectors for loop
sumSqDiff = zeros(length(h_iijj),1);
N_h_iijj = imLngX*imLngZ;
N_h_iijj(1:length(h_iijj),1) = N_h_iijj;
```

```
% loop
parfor j = 1:imLngX % y-axis loop
    for k = 1:imLngZ % z-axis loop
        % get vector of voxels in direction being analyzed
        semVec = imDen(j,:,k); % converted to double precision
        semVec = semVec';
        % square difference between unique points
        sqDiff = (semVec(ii)-semVec(jj)).^2;
        sumSqDiff = sumSqDiff+sqDiff;
    end
end

hy = unique(h_iijj);
N_h = zeros(length(hy),1);
sumSqDiff_h = N_h;
for i = 1:length(hy)
    h_iijj_true = h_iijj==hy(i);
    N_h(i) = sum(N_h_iijj(h_iijj_true));
    sumSqDiff_h(i) = sum(sumSqDiff(h_iijj_true));
end
Yvariogram = 1./(2*N_h).*sumSqDiff_h; % semivariogram

% save data
% y semivariogram
SemVarTable = table(hy,Yvariogram,...
    'VariableNames',{'length__mm' 'Semivariance'});
dataName = 'ySemVar';
filename = sprintf('%1$s_%2$s.csv',imageSetID,dataName);
writetable(SemVarTable,filename)

% ~Z-direction semivariogram~
% determine unique combination of pionts
points = int8(ones(imLngZ,imLngZ));
unqPoints = logical(triu(points));
[ii,jj] = find(unqPoints); % location of unique points
h_iijj = abs(ii-jj)*voxelSize; % distance vector

% define semivariogram distances count and vectors for loop
sumSqDiff = zeros(length(h_iijj),1);
N_h_iijj = imLngX*imLngY;
N_h_iijj(1:length(h_iijj),1) = N_h_iijj;

% loop
parfor j = 1:imLngX % y-axis loop
    for k = 1:imLngY % z-axis loop
        % get vector of voxels in direction being analyzed
        semVec = imDen(j,k,:); % converted to double precision
        semVec = reshape(semVec,[length(semVec),1]);
        % square difference between unique points
        sqDiff = (semVec(ii)-semVec(jj)).^2;
        sumSqDiff = sumSqDiff+sqDiff;
    end
end

hz = unique(h_iijj);
N_h = zeros(length(hz),1);
```

```
sumSqDiff_h = N_h;
for i = 1:length(hz)
    h_iijj_true = h_iijj==hz(i);
    N_h(i) = sum(N_h_iijj(h_iijj_true));
    sumSqDiff_h(i) = sum(sumSqDiff(h_iijj_true));
end
Zvariogram = 1./(2*N_h).*sumSqDiff_h; % semivariogram

% save data
% z semivariogram
SemVarTable = table(hz,Zvariogram,...
    'VariableNames',{'length__mm' 'Semivariance'});
dataName = 'zSemVar';
filename = sprintf('%1$s_%2$s.csv',imageSetID,dataName);
writetable(SemVarTable,filename)

% Visulize
figure
subplot(3,1,1)
plot(hx/1000,Xvariogram)
title('x-axis semivariogram')
xlabel('distance (mm)')
ylabel('semivariance')
xlim([0 55])
xticks(0:5:55)
grid on
subplot(3,1,2)
plot(hy/1000,Yvariogram)
title('y-axis semivariogram')
xlabel('distance (mm)')
ylabel('semivariance')
xlim([0 55])
xticks(0:5:55)
grid on
subplot(3,1,3)
plot(hz/1000,Zvariogram)
title('z-axis semivariogram')
xlabel('distance (mm)')
ylabel('semivariance')
xlim([0 55])
xticks(0:5:55)
grid on


end

toc

save semivarData
```

APPENDIX A5 – SEMIVARIOGRAM MODEL FITTING MATLAB CODE

```
function [] = semivariogramModelFitting()
%% semivariogram modeling fitting
clear
load('C:\Users\ajmclem\Desktop\PC xray
temp\resultsSemivar\5DsemivarData.mat',...
    'Xvariogram', 'Yvariogram', 'Zvariogram','hx','hy','hz')


%% process variables
% only use points out the h = 0.5 image width
% limit to 20 mm
xV = Xvariogram(1:335);
xH = hx(1:335);
yV = Yvariogram(1:335);
yH = hy(1:335);
% limit to 50 mm
zV = Zvariogram(1:832);
zH = hz(1:832);

% normilize varience values
%xV = xV./max(xV);
%yV = yV./max(yV);
%zV = zV./max(zV);

% convert to mm
xH = xH./1000;
yH = yH./1000;
zH = zH./1000;

%% minimize x-direction
% variables to fit
H = xH;
V = xV;
% first quess
sill = 10000; % normalized
range = 5; % (mm)
i0 = [sill,range]; % first guess
lb = [0,0]; % lower bound
ub = [1e8,50]; % upper bound
A = [];b = []; Aeq = []; beq = [];
% define function to minimize
% solver variables, x
% passing extra variables through
fun = @(x)minimizeRsq(x, V, H);
% solver
[x,fval,~,~] = fmincon(fun,i0,A,b,Aeq,beq,lb,ub);
% output
sprintf('x-direction')
sill = x(1)
range = x(2)
R_sq = 1-fval
% plot
figure(1)
```

```
subplot(3,1,1)
fit = sill*(1-exp(-(3*H./range)));
plot(H,V,H,fit)
title('x-direction')
legend('emperical','fit')

%% minimize y-direction
% variables to fit
H = yH;
V = yV;
% first guess
sill = 10000; % normalized
range = 5; % (mm)
i0 = [sill,range]; % first guess
lb = [0,0]; % lower bound
ub = [1e8,50]; % upper bound
A = [];b = []; Aeq = []; beq = [];
% define function to minimize
% solver variables, x
% passing extra variables through
fun = @(x)minimizeRsq(x, V, H);
% solver
[x,fval,~,~] = fmincon(fun,i0,A,b,Aeq,beq,lb,ub);
% output
sprintf('y-direction')
sill = x(1)
range = x(2)
R_sq = 1-fval
% plot
subplot(3,1,2)
fit = sill*(1-exp(-(3*H./range)));
plot(H,V,H,fit)
title('y-direction')
legend('emperical','fit')

%% minimize x-direction
% variables to fit
H = zH;
V = zV;
% first guess
sill = 10000; % normalized
range = 5; % (mm)
i0 = [sill,range]; % first guess
lb = [0,0]; % lower bound
ub = [1e8,50]; % upper bound
A = [];b = []; Aeq = []; beq = [];
% define function to minimize
% solver variables, x
% passing extra variables through
fun = @(x)minimizeRsq(x, V, H);
% solver
[x,fval,~,~] = fmincon(fun,i0,A,b,Aeq,beq,lb,ub);
% output
sprintf('z-direction')
sill = x(1)
range = x(2)
```

```
R_sq = 1-fval
% plot
subplot(3,1,3)
fit = sill*(1-exp(-(3*H./range)));
plot(H,V,H,fit)
title('z-direction')
legend('emperical','fit')

%%
function [fit] = semivariogramModel(H,sill,range)

fit = sill*(1-exp(-(3*H./range)));

function [fval] = minimizeRsq(x,V,H)
sill = x(1);
range = x(2);

fit = semivariogramModel(H,sill,range);

SSr = sum((V-fit).^2);
SSt = sum((V-mean(V)).^2);
R_sqr = 1 - SSr/SSt;

fval = 1-R_sqr;
```

APPENDIX A6 – CHARACTERIZATION OF PERVIOUS CONCRETE WITH X-RAY COMPUTER TOMOGRAPHY AND GEOSTATISTICS DATA REPORT

Introduction

Multiple methods were applied to characterize pervious concrete (PC) cores. The outcome did not lead to a fully developed research project and do not fully align with the topic of chapter V. Methods and results of the additional work are presented here in a data report as a record. X-ray computer tomography data used by the methods presented here were the same data sets used in chapter V. The relative elementary volume (REV) is determined with the use of geostatistics and is compared to commonly used length parameters. Length parameters quantified include the two-point correlation function and equivalent diameter. Segmentation of x-ray CT images is required to computer the two-point correlation function and equivalent diameter. Hsieh et al. (1998) segmentation result from chapter V were used to the length parameters calculations.

Methods

Collection of cores

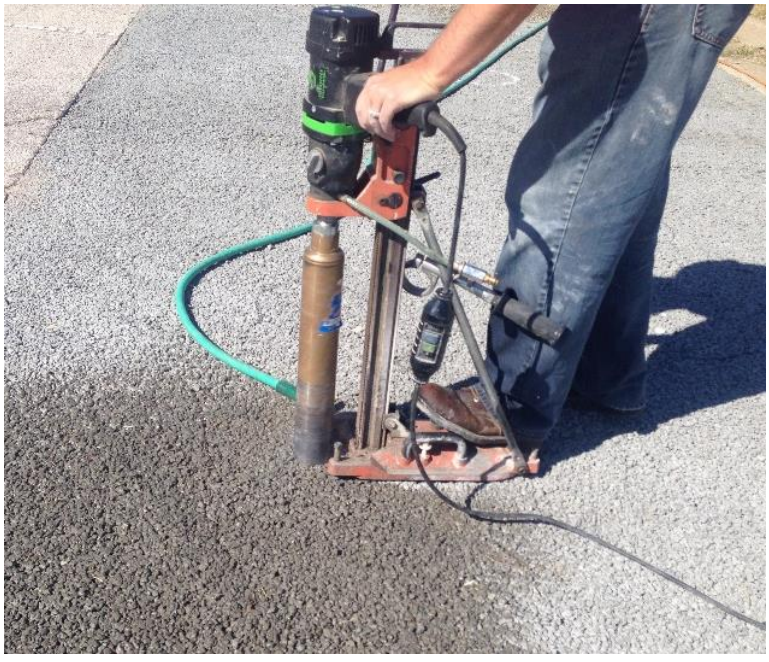

Figure A7.1. Coring drill and rig used to collect pervious concrete cores from the Tulsa, OK demonstrating plots

Table A7.1. Pervious concrete core identification labeling scheme, and total length.

Core ID (plot #-gradient)	Length mm
1U	152
1D	137
3U	140
3D	133
4U	127
4D	105
5U	140
5D	114

Characterization of pores

Three techniques were employed to characterize pore size of the voids within the PC cores. Two of the methods rely on segmented images while the third does not. Methods that require segmented images utilized voids identified through Hsieh relative frequency fitting. A representative pore diameter determined from voids in the two-point correlation length and equivalent diameter from non-connected pores. Semivariogram modeling was utilized to determine a representative length that does not rely on segmentation.

A representative pore diameter was determined with the two-point correlation procedure developed by Berrymand and Blair (1986). Two-point correlation has been extensively used in PC research to identify representative pores sizes (Deo et al. 2010, Neithalath et al. 2010, Martin 2013, Kuang et al. 2015, Sumanasooriya et al. 2009, Akand et al. 2016). The process involves randomly placing different length lines on the image and determining if both ends fall within the same material. The two-point correlation function is defined as

$$S_2(l) = \frac{1}{2l+1}\sum_{l=0}^{2r} S_2\left(r, \frac{\pi l}{4r}\right) \qquad (A7.1)$$

where S_2 denotes the second corrleation funciton, l is the length of the line, and r is the maximum radius of line l. Berryman and Blair (1986) showed that the two-point correlation function has the properties that

$$S_2(0) = \phi \qquad (A7.2)$$

and

$$S_2(l \to \infty) = \phi^2 \qquad (A7.3)$$

where ϕ is the core porosity, segmented as void space. A representative pore size is calculated from the shape of the two-point correlation function as

$$d_{TPC} = \frac{l_{TPC}}{1 - \phi} \qquad (A7.4)$$

The correlation length, l_{TPC}, is the corresponding length when the slope of the two-point correlation function at $l=0$ intersects the horizontal asymptote defined by Eq. 5.9. Stacks of segmented images were analyzed for each core with ImageJ™ (freely downloadable from www.rsb.info.nih.gov). The images were segmented using the component frequency fitting by Hsieh et al. (1998). A single representative pore diameter was determined for each core.

A representative length was also determined by back calculating the radius of connected void voxels within an image slice. Voids were considered connected if any of the surrounding 8-voxel were also classified as a void (Figure A7.2). Voxel i is considered connected to any of the surrounding 8 voxels if they are both classified as voids by the segmentation process. After pores are identified, the count of the voxels defines the individual pore area. A representative diameter was determined for each individual pore by modeling the area as a circle such that the diameter is calculated as

$$d_{ra} = \sqrt{\frac{4\ (voxel\ size)^2\ \sum(connected\ voxel)}{\pi}} \qquad (A7.5)$$

where d_{ra} is the diameter that represents the pore area. This process was completed on each image slice of all cores. Matlab's Image Toolbox *regionprops* function was used to automate this process (The MathWorks Inc 2016). The d_{50} and d_{75} were determined for each core for comparison to other core based representative parameters and mix design and long-term infiltration rate performance.

1	2	3
4	*i*	5
6	7	8

Figure A7.2. Pore space object identification check with an 8-connected voxel matrix.

Segmentation is required to compute the representative pore diameter with the two-point correlation function and back calculation of d_{ra} from non-connected pores. Vogel et al. (2003) showed that geostatistics can be used to evaluate isotopy, heterogeneity, and representative volume directly from density values of a CT images with semivariogram modeling. The semivariogram represents spatial variability from point *x* separated by a distance *h* to point *y* by taking the one-half the average of the square difference between the points.

$$\gamma(l) = \frac{1}{2N(h)} \sum_{i=1}^{N(h)} (x_i - y_i)^2 \qquad (A7.6)$$

The distance at which the semivariogram reaches a horizontal asymptote is the range. The horizontal asymptote is called the sill. Here, the range is used as representative length for PC. Another attribute of a semivariogram is the nugget, which is variance at $h = 0$. The images in this

study had varying image artifact corrections applied them during the reconstruction process. Range values were determined by fitting an exponential model to measured data.

$$\gamma(l) = 1 - e^{(-(3l/a))} \qquad (A7.7)$$

where *a* is the range.

Statistical correlations

Statistical relationships between porosity and pore size characterizations were compared to the long-term infiltration trends and cleaning effectiveness presented in chapter 3. Pearson's correlation coefficients were used as an indicator of meaningful statistical relationships. A Pearson's correlation coefficient was considered strong if it was greater than or equal to 0.75 or less than or equal to -0.75. Matlab was used to calculate Pearson's correlation coefficient and p-values (The MathWorks Inc 2016).

Characterization of pores and statistical correlations

Pore size and correlations

Segmentation based characteristic length d_{TPC} is generally less than d_{50} with an average difference of 0.573 mm for the entire core and 0.438 mm for the top 10 mm of all core samples (Table A7.2). Representative length, d_{50} and d_{75} of the top 10 mm of each core are less than the entire core all core except 3U, 4U, and 4D. Mixed component fraction indicated less clogging for cores 3U and 4U, and 4D was not considered clogged based on infiltration rate. These three cores also have the largest d_{TPC}, suggesting that d_{TPC} may be related to clogging potential. Table A7.3 is a matrix of Pearson's correlation coefficients and corresponding p-values for characteristic lengths. All segmentation based characteristic lengths are strongly correlated and statistically significant with a confidence of 95%; expect d_{50} for the core to all variables and d_{75} for the core to d_{50} for the top 10 mm. For the cores imaged, d_{50} of the core is inconsistent and is not a good indicator of

other length scales. Though, the d_{50} in the top 10 mm is correlated with many other parameters. Additionally, the top 10 mm d_{75} and d_{TPC} are strongly correlated to each other and the entire core segmentation based characteristic lengths and the void content. Measurements from the top 10 mm, which is more easily accessible compared to the entire core, provide information relative to the entire core. Only needing to analyze the top 10 mm could make estimating the void content more accessible to techniques that cannot measure the entire core depth. Subsamples from the top could be collected and void content quantified. Characteristic lengths could then be estimated from the correlations between voids and representative lengths.

Table A7.2. d_{TPC}, d_{50}, and d_{75} for the entire and top 10 mm from segmented photos using Hsieh et al. (1998) methodology.

	Entire core			Top 10 mm		
Sample ID	d_{TPC} (mm)	d_{50} (mm)	d_{75} (mm)	d_{TPC} (mm)	d_{50} (mm)	d_{75} (mm)
1U	1.067	1.940	3.590	0.693	1.640	2.770
1D	1.302	2.033	3.649	0.852	1.438	2.665
3U	1.376	1.754	3.466	1.671	1.786	3.292
3D	1.238	1.732	3.366	1.027	1.381	2.668
4U	2.093	1.925	4.289	2.139	2.272	4.870
4D	1.470	2.006	4.356	1.902	1.662	4.543
5U	0.972	1.809	3.164	0.569	1.318	2.200
5D	1.064	1.966	3.320	0.526	1.386	2.183

Table A7.3. Pearson's correlation coefficient (lower triangle) and p-value (upper triangle) between representative pore lengths. Green correlation coefficients have strong positive correlations and blue p-values values are significant at an alpha=0.05. There were 8 data points used for each correlation.

	Core d_{TPC} (mm)	Core d_{50} (mm)	Core d_{75} (mm)	Top 10 mm d_{TPC} (mm)	Top 10 mm d_{50} (mm)	Top 10 mm d_{75} (mm)	Core void fraction	Top 10 mm void fraction	X-direction Range (mm)	Y-direction Range (mm)	Z-direction Range (mm)	X-direction Sill	Y-direction Sill	Z-direction Sill
Core d_{TPC} (mm)		0.722	0.016	0.004	0.002	0.003	<0.001	0.010	0.080	0.090	0.218	0.001	0.001	0.001
Core d_{50} (mm)	0.151		0.188	0.987	0.817	0.577	0.849	0.799	0.475	0.385	0.109	0.791	0.794	0.848
Core d_{75} (mm)	0.803	0.519		0.013	0.041	<0.001	0.011	0.004	0.375	0.467	0.744	0.004	0.005	0.005
Top 10 mm d_{TPC} (mm)	0.883	0.007	0.819		0.011	<0.001	0.002	<0.001	0.082	0.130	0.263	0.001	0.001	0.001
Top 10 mm d_{50} (mm)	0.901	0.098	0.727	0.827		0.008	0.001	0.009	0.081	0.053	0.272	0.002	0.001	0.002
Top 10 mm d_{75} (mm)	0.891	0.234	0.943	0.950	0.848		0.001	0.000	0.191	0.233	0.414	<0.001	<0.001	<0.001
Core void fraction	0.968	0.081	0.828	0.913	0.929	0.940		0.002	0.115	0.105	0.185	<0.001	<0.001	<0.001
Top 10 mm void fraction	0.832	0.108	0.881	0.971	0.838	0.979	0.901		0.145	0.186	0.382	<0.001	<0.001	<0.001
X-direction Range (mm)	0.651	-0.297	0.364	0.649	0.650	0.516	0.601	0.565		<0.001	0.031	0.137	0.144	0.124
Y-direction Range (mm)	0.636	-0.358	0.302	0.582	0.701	0.476	0.615	0.521	0.968		0.018	0.136	0.135	0.118
Z-direction Range (mm)	0.489	-0.608	0.138	0.450	0.442	0.337	0.522	0.359	0.753	0.797		0.256	0.257	0.200
X-direction Sill	0.930	0.112	0.879	0.940	0.909	0.979	0.984	0.957	0.574	0.575	0.456		<0.001	<0.001
Y-direction Sill	0.929	0.111	0.869	0.932	0.924	0.972	0.987	0.951	0.566	0.576	0.455	0.999		<0.001
Z-direction Sill	0.921	0.082	0.866	0.930	0.908	0.970	0.984	0.949	0.589	0.598	0.507	0.997	0.997	

The use of a segmentation process can bias the representative pore lengths as evident in the difference between Otsu's and Hsieh's void fraction results (Figure 5.2). The range and sill from semivariogram models are an alternative method that requires only spatially defined material densities, which is a fundamental characteristic of CT images. All semivariogram models have strong fits with R^2 values above 0.970 (Table A7.4). Range values for the x- and y-direction are more similar than between x- and z-direction or y- and z-direction. The average absolute difference between x- and y- direction ranges values is 0.125 mm, while it is 0.310 mm and 0.270 mm for x- and z-direction or y- and z-direction, respectively. However, the range values in the x- and y- direction are greater than and less than the z-direction range value. There is no consistent trend to explain the variability. It was hypothesized that the z-direction range would be less than the others because of the porosity changes with depth, but that trend is not evident in the data. Sill values follow a similar trend as the range relative to direction, though, they have strong correlations to segmentation based characteristic lengths and void content (Table A7.3). Range values are only strongly correlated to each other. They are correlated to other characteristic lengths or the void fraction, but none of the correlations are strong nor are they statistically significant at a 95% confidence level. The results indicate that semivariogram range values cannot be used as a substitute to estimate segmentation based characteristic lengths, though sill values can.

Table A7.4. Semivariogram model range, sill, and R^2 for the entire core in the x, y, and z directions.

	X-direction			Y-direction			Z-direction		
Sample ID	range (mm)	sill	R^2	range (mm)	sill	R^2	range (mm)	sill	R^2
1U	5.60	8.97E+05	0.986	5.83	9.09E+05	0.985	5.53	9.17E+05	0.987
1D	5.73	8.47E+05	0.990	5.63	8.38E+05	0.988	5.08	8.41E+05	0.981
3U	6.24	9.79E+05	0.995	6.20	9.88E+05	0.991	5.86	9.73E+05	0.983
3D	5.94	8.96E+05	0.993	5.96	8.92E+05	0.988	6.66	9.21E+05	0.987
4U	6.20	1.27E+06	0.986	6.36	1.29E+06	0.987	6.28	1.24E+06	0.988
4D	5.37	1.11E+06	0.981	5.27	1.11E+06	0.979	5.22	1.09E+06	0.988
5U	4.89	8.26E+05	0.984	5.12	8.25E+05	0.990	5.09	8.26E+05	0.970
5D	4.78	7.90E+05	0.986	4.90	8.03E+05	0.987	5.01	8.08E+05	0.980

Mix design correlations

Measuring void content and characteristic lengths can be time consuming and expensive. Here, correlations are presented in an effort to provide a means of determining relationships between void content and characteristic lengths from mix design (Table A7.5). Correlations were determined between the previously presented characteristic lengths and void content to ratios of predominate PC constituents and fresh unit weight presented in chapter 3. This analysis is limited to data sets of only 4 unique points per variables, which caused a lack of significance at a 95% confidence level even though many of the correlations are strong.

Fresh unit weight is strongly correlated to void content and characteristic lengths, except d_{50} for the core and range values. The relationship between fresh unit weight and porosity was expected as Kevern et al. (2008) presented similar findings. Having a strong correlation between fresh unit weight and several of the characteristic length is also expected because many of the characteristic lengths are strongly correlated (Table A7.3). Lack of significant relationships is partially related to the small sample size. Many of the correlations to W:(C+FA), C:FA, and S:(A+S) are strong and this is expected because these ratios describe the actual quantities of material within the PC. Multiple strong correlations to (A+S)/(C+FA) were expected, but only the d_{50} is statistically

significant and strongly correlated. The core d_{50} is also correlated to S:(A+S), indicating that the addition of sand modifies the distribution of smaller pore sizes.

Table A7.5. Pearson's correlation coefficients between representative pore lengths and mix design parameters. Green values have strong positive correlations, red values have strong negative correlations, and bolded values are significant at an alpha=0.05. There were 4 data points used for each correlation. Representative pore lengths were taken as the average of the core from the same pervious concrete test plot.

	S:(A+S)	W:(C+FA)	C:FA	(A+S)/(C+FA)	Fresh Unit Weight (kg/m^3)
Core void fraction	0.171	-0.616	0.762	0.451	-0.939
Top 10 mm void fraction	0.246	-0.675	0.819	0.434	-0.931
Core d_{50} (mm)	-0.754	0.495	-0.222	**0.959**	-0.513
Core d_{75} (mm)	-0.074	-0.394	0.623	0.745	**-0.999**
Top 10 mm d_{50} (mm)	0.175	-0.616	0.792	0.546	**-0.965**
Top 10 mm d_{75} (mm)	0.120	-0.575	0.746	0.538	**-0.969**
Core d_{TPC} (mm)	0.191	-0.632	0.790	0.486	**-0.951**
Top 10 mm d_{TPC} (mm)	0.371	-0.765	0.865	0.282	-0.860
X-direction Range (mm)	0.835	-0.929	0.945	-0.048	-0.397
Y-direction Range (mm)	0.834	-0.923	0.940	-0.046	-0.391
Z-direction Range (mm)	0.934	**-0.984**	0.891	-0.407	-0.238
X-direction Sill	0.154	-0.603	0.760	0.487	**-0.953**
Y-direction Sill	0.142	-0.594	0.750	0.489	**-0.953**
Z-direction Sill	0.190	-0.632	0.783	0.463	-0.944

S – sand, A – aggregate, W – water, FA – fly ash

Long-term and cleaning performance correlations

Initial infiltration rate and sustained long-term performance of PC are critical for meeting stormwater management goals. Pores in PC are the conduits for flow and the medium for clogging. Linking pore characteristics lengths to long-term performance provides insight into the controlling properties of PC. Pearson's coefficients indicating correlations between mix design, infiltration rate, and clogging trends are discussed in chapter 4 and are listed in Appendix A1.

Phase 1 infiltration rates have a strong positive correlation to many of the characteristic lengths and the void content (Table A7.6). It is also strongly correlated to the semivariogram sill values.

Pore characteristic are not statistically correlated the initial clogging duration. Phase 1 clogging is assumed be the result of small pore clogging. Characteristic pore lengths represent medium to large pore sizes and not necessarily the small pores, thus supporting the theory regarding the initial clogging phase. The rate of clogging during phase 1 only has a statistically significant (alpha = 0.05) negative correlation with d_{75} of the core and the top 10 mm of the core. This relationship may be influenced by the magnitude of the initial infiltration rate. Cores with higher infiltration rate also have larger d_{75}. These cores most likely have more small pores because the void content is also strongly correlated to the d_{75}. Since cores with a larger void content probably have a higher quantity of small pores compared to cores with lower void content, their initial infiltration rate will decrease at a faster rate than cores with fewer small pores.

Phase 2 infiltration rate has a statistically positive correlation with many of the pore characteristics (Table A7.6). The duration of phase 2 and slope of the regression fit are not statistically correlated at a 95% confidence level, though, many of the parameters have strong positive correlations. These strong correlations are logical; PC with larger pores would be expected to have higher infiltration rates and would be less likely to clog. Phase 3 regression slope has a significant negative correlation to d_{75}. This follows the trend of the phase 1 regression slope, suggesting that the infiltration rate of PC with larger pores and higher infiltration rates are will decrease more rapidly than cores with smaller pores. This does not mean that the magnitude of infiltration rate is less, just that the rate of change is larger. PC with larger pores exhibit a faster decline of infiltration rate, but the duration of the phase is long because the total pore space is greater.

Similar to many mix design parameter, d_{50} of the cores have no statistical significant correlations to clogging trends. However, d_{50} has a strong negative correlation (p-value = 0.0018) to cleaning performance (-0.999). It is assumed that the PC with a greater percentage of smaller pores would cause clogging to stay near the surface. This is supported by the correlation to the d_{50} of the core,

but is contradicted by the positive correlations with void content and all characteristic length except the d_{75} of the core.

Table A7.2. Pearson's correlation coefficients between representative pore lengths and long-term infiltration rate trends. Green values have strong positive correlations, red values have strong negative correlations, and bolded values are significant at a 95% confidence level. There were 4 data points used for each correlation. Representative pore lengths were taken as the average of the core from the same pervious concrete test plot.

	Initial infiltration rate (cm/min)	Phase 1 clogging duration (days)	Phase 1 clogging regression slope (cm/min/day)	Phase 2 average infiltration rate (cm/min)	Phase 2 duration (days)	Phase 3 regression slope (cm/min)*	Cleaning, % of phase 2 infiltration rate*
Core void fraction	**0.966**	0.360	-0.925	**0.895**	0.971	-0.298	0.676
Top 10 mm void fraction	0.946	0.307	-0.909	**0.935**	0.953	-0.429	0.566
Core d_{50} (mm)	0.418	-0.549	-0.550	0.098	0.409	-0.470	**-0.999**
Core d_{75} (mm)	**0.973**	0.043	**-0.993**	**0.846**	0.975	**<-0.999**	-0.477
Top 10 mm d_{50} (mm)	**0.958**	0.184	-0.945	**0.939**	0.965	-0.711	0.251
Top 10 mm d_{75} (mm)	**0.979**	0.264	**-0.956**	**0.903**	0.983	-0.598	0.394
Core d_{TPC} (mm)	**0.962**	0.281	-0.933	**0.925**	0.968	-0.512	0.486
Top 10 mm d_{TPC} (mm)	0.891	0.405	-0.832	0.931	0.899	-0.201	0.747
X-direction Range (mm)	0.338	-0.089	-0.323	0.832	0.360	-0.593	0.399
Y-direction Range (mm)	0.329	-0.104	-0.317	0.827	0.351	-0.603	0.388
Z-direction Range (mm)	0.265	0.359	-0.172	0.695	0.284	-0.127	0.794
X-direction Sill	**0.972**	0.318	-0.938	0.902	0.977	-0.429	0.566
Y-direction Sill	**0.975**	0.327	-0.940	0.895	0.979	-0.406	0.587
Z-direction Sill	**0.963**	0.321	-0.927	0.914	0.968	-0.411	0.582

*correlations based on 3 data points

REFERENCES

Akand, L., Yang, M., and Gao, Z. (2016). "Characterization of pervious concrete through image based micromechanical modeling." *Construction and Building Materials*, Elsevier Ltd, 114, 547–555.

Berryman, J. G., and Blair, S. C. (1986). "Use of digital image analysis to estimate fluid permeability of porous materials: Application of two-point correlation functions." *Journal of Applied Physics*, 60(6), 1930–1938.

Hsieh, H. T., Brown, G. O., Stone, M. L., and Lucero, D. A. (1998). "Measurement of porous media component content and heterogeneity using gamma ray tomography." *Water Resources Research*, 34(3), 365–372.

Kevern, J. T., Schaefer, V. R., Wang, K., and Suleiman, M. T. (2008). "Pervious Concrete Mixture Proportions for Improved Freeze-Thaw Durability." *Journal of ASTM International*, 5(2), 101320.

Kuang, X., Ying, G., Ranieri, V., and Sansalone, J. (2015). "Examination of Pervious Pavement Pore Parameters with X-Ray Tomography." *Journal of Environmental Engineering*, 141(10), 1–13.

Martin, W. (2013). "Hydraulic Impact of Porosity Distribution and Hydrologic Characterization of Porous Pavements." PhD Dissertation, Clemson University.

Neithalath, N., Bentz, D., and Sumanasoorlya, M. (2010). "Predicting the Permeability of Pervious Concrete: Advances in Characterization of Pore Structure and Transport Properties." *Concrete International*, 32(5), 35–40.

Otsu, N. (1979). “A Threshold Selection Method from Gray-Level Histograms.” *IEEE Transactions on Systems, Man and Cybernetics*, 9(1).

Sumanasooriya, M. S., and Neithalath, N. (2009). “Stereology- and morphology-based pore structure descriptors of enhanced porosity (Pervious) concretes.” *ACI Materials Journal*, 106(5), 429–438.

The Mathworks Inc. (2016). “MATLAB - MathWorks.” *www.mathworks.com/products/matlab*, <http://www.mathworks.com/products/matlab/>.

Vogel, J. R., and Brown, G. O. (2003). “Geostatistics and the representative elementary volume of gamma ray tomography attenuation in rock cores.” *Geological Society, London, Special Publications*, Geological Society of London, 215(1), 81–93.

VITA

Alex James McLemore

Candidate for the Degree of

Doctor of Philosophy

Thesis: EVALUATION OF ESTABLISHED LOW IMPACT DEVELOPMENT TECHNIQUES: ASSESSING AGED BIORETENTION CELLS AND CLOGGING PERVIOUS CONCRETE

Major Field: Biosystems and Agricultural Engineering

Biographical:

Education:

Completed the requirements for the Doctor of Philosophy in Agricultural and Biosystems Engineering at Oklahoma State University, Stillwater, Oklahoma in November 2017.

Completed the requirements for the Master of Science in Biosystems Engineering at the University of Tennessee, Knoxville, Tennessee in 2012.

Completed the requirements for the Bachelor of Science in Biosystems Engineering at the University of Tennessee, Knoxville, Tennessee in 2010.

Experience:

Research Engineer, Oklahoma State University, Stillwater, Oklahoma January 2013 to August 2017.

Professional Memberships:

American Society of Agricultural and Biosystems Engineers (ASABE)

American Society of Civil Engineers (ASCE)